A Comparative Study on Water Vapor Extracted from Interferometric SAR Images and Synchronized Data

CHENG, Shilai

A Thesis Submitted in Partial Fulfillment

of the Requirements for the Degree of

Doctor of Philosophy

in

GeoInformation Science

The Chinese University of Hong Kong

August 2011

Thesis/Assessment Committee

Professor Jiayi PAN (Chair)

Professor Hui LIN (Supervisor)

Professor Daniele PERISSIN (Co-Supervisor)

Professor Yuanzhi ZHANG (Committee Member)

Professor Xiaoli DING (External Examiner)

論文評審委員會

潘家禕教授（主席）

林琿教授 (導師)

Daniele PERISSIN 教授 (共同導師)

張淵智教授（委員）

丁曉利教授（校外委員）

ABSTRACT

of thesis entitled:

A Comparative study on water vapor extracted from Interferometric SAR images and synchronized data

Submitted by CHENG Shilai

for the degree of Doctor of Philosophy

at The Chinese University of Hong Kong in August 2011

Synthetic Aperture Radar Interferometry (InSAR) is a newly developed satellite observation technology which is applied in studies of hydrosphere, atmosphere, topography and earth surface changes caused by natural or anthropogenic activities. The technology is capable of retrieving accurate geophysical parameters with multiple air-/satellite-based SAR images through establishing interferometric geometry where the phase measurements precisely reflect the geometry between spaceborne platforms and earth surface and highly sensitive to its variation. Due to these unique advantages, interferometric technology has been widely applied in surveying the ground topography and detecting tiny dynamic changes of ground surface in the last two decades.

However, the applicability of such technology is severely affected by differential atmospheric delay induced by inhomogeneity of air refractivity. Previous studies show that the water vapour with strong variation in both spatial and temporal domain dominates the atmospheric artifacts in interferometric phase measurements. It is the problem that we were trying to solve. In this research, we aim at determining and compensating atmospheric signal in SAR interferograms. Compared with previous works, this work studies the problem in a new perspective that the information of water vapor was extracted from Atmospheric Phase Screen (APS) obtained by Permanent Scatterer SAR Interferometry (PSInSAR), and was comparatively studied with synchronized water vapor data, including GPS observations, MERIS images and MM5 simulated products.

The main contributive work in this research includes following aspects:

Firstly, a water vapor component model was proposed for comparison between SAR and non-SAR water vapors. Besides the typical mixing turbulent and stratification terms, the spatial liner trend and ground feature related stationary term has been accounted for in mixed water vapor. Based on this model, a logical strategy of differentiation between spatial linear trend and height dependent stratification, and between stationary term and turbulence signal, was developed.

Secondly, point-based Precipitable Water Vapor (PWV) from SAR APS and GPS meteorology are compared based on the proposed model in order to assess the precision of water vapor signal obtained from SAR. Two implementation methods, a differential and a pseudo absolute mode, were proposed to build the comparison links between SAR differential water vapor and GPS absolute water vapor.

Thirdly, the spatial statistical properties of water vapor components have been investigated by analyzing water vapor signal obtained from SAR APS, synchronous MERIS near infrared images, MM5 Integrated Water Vapor (IWV) in differential comparison mode and in different spatial scales. Furthermore, in a demonstration example, absolute water vapor signal in fine scale was recovered from differential APS maps with MERIS at master date.

By introducing these ideas and data analysis methods, this thesis provides an insight on water vapor signal from Radar Interferometric images. This insight would be firstly significant toward final solution of atmospheric correction in SAR interferometry. While, the water vapor study at small scale is not only beneficial for hydrological study and regional weather (e.g., rainfall) predication, but also promising in meteorological applications in future. In addition, this water vapor study can be extended in improving of atmospheric error modeling for satellite observing technologies, especially in microwave ranging way, such as GNSS, coastal satellite altimetry and VIBL.

摘要

雷達干涉測量(InSAR)是一項新的衛星觀測技術，用於水氣，大氣，地形以及(自然或人為活動引起的)地表變化的研究。該技術通過多時相(機載或星載)SAR影像，組成干涉幾何模型，可以準確反演地球物理參數. 雷達干涉相位精確表達星載平臺與地球表面組成的幾何關係並對該幾何關係的變化極為敏感。由於以上優勢，因此在過去二十年中，干涉測量技術於地形測繪和地表微小形變監測方面得到了極為廣泛的應用.

但是大氣折射不均一引起的相對大氣延遲，嚴重影響干涉測量技術的應用。前人研究發現，水汽在空間和時間上均顯著變化，其對雷達干涉測量的大氣誤差起主導作用. 為解決上述問題，本論文也以 InSAR 大氣效應及其改正為研究目標。與前人研究相比，本研究從一個新的角度進行探討. 在本論文中，從大氣相位屏(永久散射體干涉測量 PSInSAR 技術)中提取水氣資訊，從而與同步水汽資料進行比較研究，包括 GPS 觀測值，MERIS 影像和 MM5 類比資料。

本研究的主要貢獻在以下方面：

首先，為對 SAR 和非 SAR 水氣資料進行比較，本論文給出了水汽組成模型。除典型的混合湍流項和高程分層項外，該模型還考慮了在水氣中混合的空間線性趨勢項和地物相關的穩定項. 基於此模型，本文提出了合理的分解策略，以區分空間線性趨勢項和高程分層項， 以及區分地物相關穩定項和大氣湍流項.

其次，基於上述模型，對 SAR 大氣相位屏和 GPS 氣象反演獲取的點狀水汽資料進行了比較，以分析 SAR 水汽含量的精度和兩種技術的相對精確度。為建立 SAR 差分水汽值和 GPS 絕對水汽值的比較，本文給出了兩種實現方式：差分和偽絕對比較模式.

其三，基於 SAR 大氣相位屏，同步的 MERIS 近紅外水汽影像和 MM5 水汽圖，本文對水汽各成分在差分(相對)模式下不同空間尺度的空間統計特性進行了研究。此外，作為範例，利用主影像日期的 MERIS 水汽圖對差分大氣相位屏進行了恢復，獲取了細尺度的絕對水氣圖。

基於上述概念和資料分析，本文旨在提供對雷達干涉圖像中水汽信號的新的見解。這種見解將首先為貢獻於 SAR 干涉圖的大氣校正最終方案。同時，細尺度的水汽研究，不僅有利於水文學研究和區域天氣（雨量）預報，而且對未來氣象應用極有前景。此外，該水汽研究還可以擴展，以提高衛星觀測技術(特別是微波測距模式)的大氣誤差模型，如全球衛星定位導航系統 GNSS，沿海衛星測高和甚長基線干涉測量(VIBL)。

TABLE OF CONTENTS

LIST OF TABLES

LIST OF FIGURES

ACKNOWLEDGEMENTS

It is unforgettable three years of my PhD study in ISEIS of CUHK, the most beautiful space in HK campus and the most exciting place in my youthhood. At the end of my study life, much wonderful memory in my mind and many moving moments at my heart compel me to express my sincerest appreciations.

Prof. Hui Lin, as my supervisor, expressing his long ambition, showing his energetic working capability, providing his insightful views and enduring much difficulty of youth, has stimulated me to the finish of PhD study. The beautiful working environment, the novel cross-discipline platform, his generous financial support and care of our study life must be firstly appreciated.

Prof. Daniele Perissin, as my co-supervisor and thesis instructor, inspired me ideas and trained me skills in InSAR research with his strong experience in PoliMi-birth place of PS-InSAR. The paramount data from him and his members within METAWAVE played critical role in my research for this thesis.

Prof. Longsang Chiu, in the one year following with him, I was stunned and moved by his dedicated and professional spirit from MIT. Prof. Jingnan Liu from Wuhan, Dr. Zhenhong Li from Glasgow and Prof. Tao Li, granted me instructions in study and help in research career. Dr. Liming Jiang, Dr. Fulong Chen, shared me technical knowledge and suggestions on this work. Also in our group, QingLi and Qinghua benefited my InSAR research.

External examiner Prof. Xiaoli Ding from the Hong Kong Polytechnic University and committee members Prof. Yuanzhi Zhang and Prof. Jiayi Pan in CUHK have helped me better organize my ideas and present my thesis work.

Also the following ones, accompanying me with delightful PhD time in HK, shall be acknowledged. The research, teaching and visiting peoples, and the administrative and supporting local staffs in our institute, all young students in ISEIS sharing happy memories, the friends from GRM always enjoying with dinner

together, and unforgettable PGH3 apartment/room partners communicating with worldwide regards, encouraging letters and romantic happiness even now, shall be delightfully acknowledged.

I shall pay my extremely appreciation to my fiancée Ms. Kun Xiao and family members. They have been rowing one boat with me in all my hard time with their continuous encouragement and consideration on my study and career.

Finally, to the following research climbers, I would be frankly to say, there are many hard days in the three years, when I suffered at the edge of quitting, when I felt extremely frustrated in the communication, when I fell all at sea to structure my thesis for defense, but after all the cold winter is gone, my determination and enthusiasm are reignited. A word from one romantic film is cited to encourage me, and also to you, 'my heart will go on'.

Chapter 1 Introduction

Synthetic Aperture Radar Interferometry, abbreviated to SAR Interferometry or InSAR, is a new satellite observation technology to serve studies in hydrosphere, atmosphere, earth topography and anthropologic induced earth surface changes. As interferometry firstly named in optical physics as interference of two beam of visible light from the same origin in last 1940s, Radar Interferometry afterwards refers to interference of two microwave band electromagnetic waves transmitted and received by remotely observing instrument. Forming interferometric geometry, achieving sufficient coherence and retrieving geophysical parameters (surface topography, ground deformation and etc.) with multiple air-/satellite-based SAR images, are three inherent characteristics of InSAR technology. The interferometric phases of coherent waves are highly sensitive and precise measurements of geometry (and its variation) between spaceborne platforms and the observed earth surface. Therefore in last two decades, this InSAR technology has been widely convinced being advantageous to survey the ground topography and monitor the dynamical state of earth surface.

However, such measurements are critically contaminated by differential atmospheric delay induced by inhomogeneity of air refractivity. Through previous study, the water vapour-with strong variation in both spatial and temporal domain, dominates the atmospheric artifacts in interferometric phase measurements. The intention of study and modeling of water vapor variation, for breaking up the limitation of atmospheric decorrelation and distortion, has long been the hotspot of SAR interferometry. An exploratory water vapor study, from SAR interferometric images and other technologies, therefore, is the primary interest and main topic of this thesis.

1.1 Background

Interferometry, from the idea of radio interferometry, was initiated as early as in 1946 (Tubbs 1997) and later used in the field of planetary mapping at first time in 1968 (Evans and Hagfors 1968), the application of Radar Interferometry was firstly developed nearly in 1970s. Rogers and Ingalls (Rogers and Ingalls 1969) firstly applied interferometry into radar in echoes from the planet Venus. Zisk (Zisk 1972) firstly applied radar interferometry to measure the topography of moon. Graham (Graham 1974) first applied the same technology to airborne radar to obtain earth topography from optical fringes.

InSAR is abbreviation of SAR Interferometry, can further be expanded as Synthetic Aperture Radar Interferometry. Synthetic Aperture Radar (SAR) (Kovaly 1976; Tomiyasu 1978), based on synthetic aperture technique (from Doppler Effect concept) and Pulse Compression technique, provides remarkably increased azimuth and range resolution than radar, and enable capability of 2D imaging and spaceborne observing. The invention of SAR can be regarded as the foetus of InSAR technology. Thereafter, Interferometry of SAR (Spaceborne and Airborne) system has been equipped on satellite platforms for exploratory study in geophysical research fields. SEASAT in 1978, and subsequent Magellan in 1989 and SIR-C/X-SAR in 1994 launched by NASA proved the capability of SAR Interferometry systems (Cumming 2005).

DInSAR (Differential SAR Interferometry) technique, which was extended from InSAR in 1990s, has remarkably boosted the InSAR technology after its birth in 1970s. In 1989, Gabriel et al. firstly reported the application of DInSAR technique to mapping the surface deformation in California using SEASAT images (Gabriel 1989). Additional DEM data or so-called three-pass method was used to remove the topographic phase in DInSAR to retrieve better deformation measurements (Massonet 1993; Zebker 1994).

PSInSAR, initiated at the ending of 2000s, experienced a second advance of InSAR technology. Analysis on phase-stable point-like targets from time series dataset is key breakthrough in this field. Permanent Scatterer or Persistent Scatterer (PS) (Ferretti 2000; 2001), Small baseline subset (SBAS) (Berardino 2002; 2004; Lanari 2004), Coherent Targets (CT) (Mora 2003) and Quasi-Permanent Scatterer (QPS) (Perissin 2007) are representative realization approaches. The advantage of this group of InSAR techniques lies in greatly overcoming of conventional intrinsic InSAR limitation, in terms of temporal and geometrical decorrelation as well as atmospheric disturbances.

Table 1.1 Typical Space-borne SAR sensors/platforms for earth observation.

Mission	Agency	Period of Operation[1]	Orbit Repeat Cycle (days)	Frequency (bands[b], GHz;)	Wave-length (cm)	Incidence Angle at center (deg.)	Resolution (m)
Seasat	NASA*	06/27 to 10/10, 1978	17	L-band 1.2	25	20 to 26	25
ERS-1	ESA*	07/1991 To 03/2000	3, 168, and 35[4]	C^b5.3	5.66	23	30
SIR-C/X-SAR	NASA, DLR*, and ASI*	04/09 to 04/20, 1994, And 09/30 to 10/11, 1994	6 mon., 1-, 2-, 3-day[7]	L^b 1.249 C^b 5.298 X^b 9.6	24.0 5.66 3.1	17~ 63 (L^b, C^b) 54(X^b)	10–200 (30 typical)
JERS-1	JAXA*	02/1992 to 10/1998	44	L^b 1.275	23.5	39	20
ERS-2	ESA	04/1995 ~	35	C^b 5.3	5.66	23	30
Radarsat-1	CSA*	11/1995 ~	24	C^b 5.3	5.66	10 to 60	10–100
Envisat	ESA	03/2002 ~	35	C^b 5.331	5.63	15 to 45	20–100
ALOS	JAXA	01/2006 ~	46	L^b 1.270	23.6	8 to 60	10–100 m
TerraSAR	DLR	06/ 2007 ~	11	X^b 9.65	3.1	20 to 55	1 – 16
Radarsat-2	CSA	12/ 2007 ~	24	C^b 5.405	5.55	10 to 60	3–100
COSMO-Skymed	ASI	07/ 2007[1] 12. 2007[2] 10/ 2008[3] 11/ 2010[4]	16	X^b9.65	3.1	20 to 50	1, 3-15, 30, 100

Notes: 1~4 means the information of corresponding satellite of COSMO constellation.

* marks the international agencies, each can referred to list of acronyms.

SAR Sensors and platforms played critical impulsing role in the development history of InSAR technology. Interferometric SAR images are retrieved in two system work modes. One is cross-track (and along-track) interferometry that images are formed from two antennas on a single platform with a certain distance for simultaneous interferometry. The usual implementation of this form is antennas on aircraft or special space-borne systems such as Topographic SAR (TOPSAR) and Shuttle Radar Topography Mission (SRTM) systems (Zebker 1992; Farr and Kobrick 2000). The other is that image pairs are created by one antenna on spaceborne platform in nearly identical repeating orbits, called repeat-pass SAR interferometry (Gray and Farris-Manning 1993; Massonnet and Feigl 1998). Repeate-pass is the typical implementation for SAR interferometry with spaceborne sensors such as the U.S. SEASAT, European Remote-sensing Satellites (ERS-1 and ERS-2), Shuttle Imaging Radar-C (SIR-C), Canadian Radar Satellite (Radarsat-1), Japanese Earth Resources Satellite (JERS-1), and European Environmental Satellite (Envisat), all of which operate at wavelengths ranging from centimeters (C-band) to tens of centimeters (L-band). Table 1.1 lists all current typical platforms and properties of corresponding SAR sensors (Henderson 1998; Kramer 1996).

Applications of InSAR have covered various aspects related to earth surface geometry and its dynamics. With the capability of detecting ground-surface with a spatial resolution of tens-of-meters over a relatively large region (~10,000 square km), in almost all weather conditions, SAR interferometry has definite advantages over conventional geodetic techniques on earth observation. Up to date, two developed groups of applications are most matured and world widely introduced in Engineering.

One is earth surface topography reconstruction or DEM generation (Zebker 1988). The Shuttle Radar Topography Mission (SRTM) in 2000 represented the third flight of SIR-C and X-SAR (Farr, 2000; Rao 2001; Breit; 2002; Rabus 2003; JPL 2004). In this mission, a 60-m outboard antenna was added to the Shuttle for

4

simultaneous reception of the C- and X-band SAR signals. The received data provides almost complete DEM within ±60° latitude, with a horizontal posting of 30 m and a vertical accuracy of 16 m.

The other one is earth surface deformation monitoring. This technique provides an advantageous monitoring tool on ground subsidence (Gabriel 1989; Avallone 1999; Carnec 1999; Buckley 2000; Crosetto 2002), ground deformation after earthquakes (Massonnet 1993; Zebker 1994; Rigo and Massonnet 1999; Cervelli 2001), volcanic movements (Rubin 1992; Massonnet 1995; Hooper 2006), and potential for landslide (Colesanti 2003; Hilley 2004; Vcka 2005) and glacial drift (Mohr 1998; Jónsson 1998). Among these applications, the most widely employment of InSAR technique is to detect the ground subsidence in megapolis where underground water over exploitation, soft soil groundwork construction or coastland reclamation frequently occurs.

However, both spatial and temporal variation of atmospheric pressure, temperature and water vapor content, would produce inheterogeneity of atmospheric refractivity that could significantly affect the transmission of radar signal. The artifact of returned signal in SAR images then produces artificial fringes in interferograms. Such artificial fringes have long been a limiting factor in high precision measurements of InSAR. Massonnet et al. firstly identified the atmospheric effects in InSAR when they studied the 1992 Landers earthquake (Massonnet 1994). After their work, the impact of atmospheric effect on InSAR has been studied by various experiments (Goldstein 1995; Rosen 1996; Zebker 1997; Hanssen 1998; 2001; Jónsson 2002; Li Z.W. 2004; Ding 2008)

The spatial temporal characteristics of atmospheric signals in interferograms studied in above investigations have been employed for estimation and elimination of InSAR atmospheric noises. This is regarded as statistical perspective. The representative approaches include: Pair-wise linear combination (Massonnet 1995; Hanssen 2001), Stacking (Zebker 1997; Sandwell and Price, 1997; Williams 1998;

5

Ferretti, 1999), Stochastic Filtering (Crosetto 2002), PS (Permanent Scatters) InSAR (Ferretti 2000; 2001; Colesanti 2003), Small baseline subset (SBAS) (Berardino 2002; 2004; Lanari 2004), Coherent Targets (CT) (Mora 2003) and Quasi-permanent scatterer (QPS) (Perissin 2007)

While in another perspective, such atmospheric effect could be regarded as the superimposition of tropospheric delay, ionospheric delay and delay induced by liquid water (Hanssen 2001). Ignoring liquid water effect in common weather, ionospheric and hydrostatic delays in regional scale (Xu 2006), only the wet troposphere (Zebker 1997) actually affect the interferometric phase measurements. Therefore, water vapor in wet atmosphere, varied in spatial and temporal domain, has long been studied to resolve the InSAR atmospheric effect. This is regarded as calibrating perspective. This method employs the external observed or modeled water vapor data including GPS (Bock and Williams 1997; Williams, 1998; Ge Linlin, 2000; Hanseen 2001; Bonforte et al. 2001; Buckley 2003; Li Z.H. 2006; Li Z.W 2006), Spaceborne radiometer data (e.g., MERIS, MODIS) (Li Z.H. 2003; 2004; 2005; 2009), MM5 (Wadge 2002; Perissin 2009), radiosondes (Saastamoinen 1972; Baby 1988; Delacourt 1998) to calibrate atmospheric effect of synchronized Radar images.

Though by various approaches (statistically filtering or synchronously observing) with continuous efforts, atmospheric effect for InSAR technology are still open and not resolved. Facing the same problem of InSAR atmospheric effect, following previous investigations, this research aims to improve understanding of atmospheric signal in SAR interferograms and its compensating. But different with previous ones, this research studies this problem in a new perspective. In this research, Atmospheric Phase Screen (APS) from Permanent Scatterer SAR Interferometry (PSInSAR) (Ferretti 2001), in form of transformed water vapor, is comparatively studied with external synchronized water vapor data, including GPS observations, MERIS images and MM5 simulated products.

1.1 Research objectives

The research objectives are presented in detail as follows aspects:

1) To identify and differentiate the different component of water vapor from SAR Interferometry;

How many contributive factors affect the water vapor retrieved from SAR Interferometric images, How to differentiate each one if they spatially co-existed and mixed together?

2) To built a reasonable comparative way of water vapor between that from SAR Interferometry and alternative technologies.

What is the characteristics of water vapor retrieved from SAR Interferometric images, how to link the above water vapor to other independent water vapor observations or obtaining techniques?

3) To qualitatively and quantitatively compare water vapor from SAR Interferometric images and alternative data sources.

What about the bias and standard deviation of interferometric water vapor, compared to other precise retrieved water vapor measurements? What is the influence of each contributive component in such comparison as given in question 1?

4) To enhance understanding of spatial and temporal statistic properties of water vapor from above technologies.

Are the spatial statistical law of water vapor and even each water vapor contributive component coherent between different water vapor data sources? How about the temporal statistical law of turbulence? And are there any difference in spectrum and variogram for different water vapor sources?

1.2 Research significance

The topic of this research is covered by multi-discipline among meteorology, hydrology, spatial statistics etc., and related to multiple high technologies, such as Global Positioning System, Remote sensing imaging, SAR Interferometry. The

7

values of above objectives are both scientifically significant and technically valuable in engineering and applications. The detail could be presented in following aspects:

1) Water vapor study serves for improving of atmospheric compensation of SAR interferometry.

   A) Precisely modeling of Water Vapor signal would directly help break through the bottle neck of atmospheric decorrelation in detection by Conventional SAR interferometry, especially with only small data amount SAR imagery or in emergency occurrences, which are still widely applicable in post seismic deformation retrieval.

   B) The statistical characteristics of atmospheric phase screen components in SAR interferometry represent a fundamental task in order to develop better algorithms for multi-temporal interferometric analysis from multi-sensor SAR datasets (Ferretti 2005).

   C) Further indirect significance in improvement of InSAR technology could be perceived not only in geophysical study of natural phenomena, e.g., monitoring of volcano, co-seismic deformation observing, movement of ice sheet, tectonics of global plate and etc., also engineering detection of anthropological ground deformation, in reclaimed land, soft or filled soil foundation ground, groundwater-overexploited city and even deforestation induced landslide in hilly area during rainy seasons.

2) Small scale water vapor model would bring remarkable significance in scientific research on regional water budget and circulation, investigation of atmospheric stratification, variation and circulation, and then civil service on rainfall prediction, weather forecast and extreme hazardous weather alarming.

3) Enhancement of atmospheric correction (with water vapor correction model) would not only improve applicability of InSAR technique, but also potentially boost other satellite ranging-based observing technologies, e.g.

GNSS, costal altimetry and VLBI, in various geospatial applications beyond ground deformation detection, e.g., positioning & timing of end users.

1.3 Research Methodology

Therefore in this section, as the core of this research, the research methodology is framed as the fundamental basis of designed experiments of this study. A PDAME analytical methodology was proposed for spatial problem solving and successfully applied in various research projects in geospatial field (Smith 2010). The PDAME methodology starts from Problem, Data, Analysis and Modeling, ended by Evaluation, and then recycles. Taking the reference of PDAME analytical methodology (Smith 2010) and based on the context of research in this thesis, a revised methodology was proposed with the logic from Questions, Data, Model &Implementation, Analysis and Conclusion. The structure of all phases of methodology is illustrated in Figure 1.1.

Questions
-From objectives and problems

Data
-APS, GPS, MM5, MERIS Water Vapor

Model and Implmentation
-Strategy of differentiation of water vapor components

Analysis
-Point-based comparison, Diff./ Pseudo-Abso. mode.
-Map-based comparison, spaital study ofwater vapor.

Conclusion
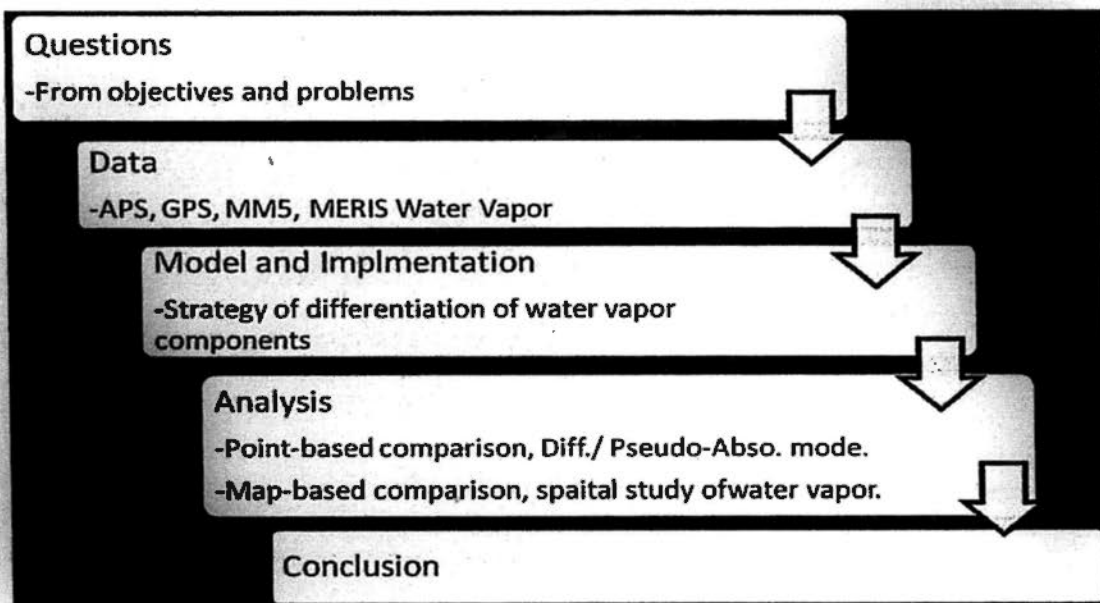
Figure 1.1 Flow chart of proposed research methodology in the thesis.

1) Selected Questions to be answered

Based on the objectives of our research, following specific unsettled questions are selected to be answered. A) For water vapor signal, besides mixing turbulence and stratification effect studied previously, is there any other effect related the water

9

vapor distribution? What's their relationship? B) How to link the water vapor obtained from Radar Interferometry with other water vapor sources from independent technologies for comparison? C) What's point-based precision of SAR derived water vapor, compared to accurate GPS meteorology water vapor? D) Use currently available map-based data, what is the spatial law of water vapor variation? What's the difference of such spatial prosperities among synchronized data?

2) Data in Experiment area

To answer the questions in phase one, the data including GPS PWV, MERIS water vapour, MM5 predicted IWV, Atmospheric Phase Screen derived from ASAR data in experimental area-north and center of Italy were collected. The data was supported as part of METAWAVE (Mitigation of Electromagnetic Transmission errors induced by Atmospheric Water Vapor Effects) project funded by ESA. In this research, Water vapor data from four kinds of sources are collected, supported by METAWAVE project funded by Europe Space Agency (ESA). The data acquisition and field campaigns have been carried out in two main test sites, Rome and Como in Italy. Besides the SAR data, GPS observations from field campaign, MERIS water vapor images, and MM5 simulated water vapor maps are presented. Since the data used in each experiment are different, the detail of each data source could be referred to the data description sections in chapters.

3) Component Model of water vapor and Implementation

A component model of water vapor has been proposed for complete consideration of signal components in APS, but also applicable for other water vapor data. In the component model of water vapor, besides the commonly referred mixing turbulent component and stratified component in water vapor signal, spatial linear trend and ground feature related water vapor signals has also been included. In addition, a logical approach of distinguishing between each water vapor components from mixed signal is analyzed in detail.

4) Comparative Analysis

Two Perspectives are analyzed from the data based on assumed Model and implemented with two different modes to answer the questions as following.

a) Point-based Comparison. Point-based water vapor products, from GPS meteorology and SAR interferometry are compared for clear illustration of individual availability, particularity and accuracy in differential comparison mode and pseudo-absolute mode.

b) Map-based Comparison. Experimental data are also chosen for map-based comparison to analyze the signal of water vapor and spatial temporal law of water vapor compositions. The spatial and temporal variation law of each component of water vapor has been investigated with synchronized data based on proposed water vapor component model by tools: power spectral analysis, decorrelation calculation, structure function derivation.

5) Conclusions

The questions framed in the first stage shall be answered according to the data analysis and experimental results. The conclusive points for each analyzing stage are drawn along with corresponding results in following chapters and then be summarized as a whole at the last chapter.

1.5 Thesis outline

Figure 1.2 depicts the content of this thesis and illustrates the relationship among different chapters. This Chapter introduces the background, objectives and significance of this research. The research methodology is also included in this chapter. Chapter 2 reviews water vapor observations, atmospheric signal in SAR interferogram and water vapor from SAR interferometry. Chapter 3 introduces component model of water vapor, which is the basis of data analysis of water vapor in next two chapters. In this chapter, a logical implementation of different components planned by the model has also been studied with MM5 data. In chapter 4, water vapor from SAR Interferometry and that from GPS meteorology have been

compared. In chapter 5, spatial stochasticity from water vapor among SAR Interferometric APS, MM5 and MERIS are comparatively studied. The last chapter concludes the work in this research and prospects the future work.

Chapter 1 Background and Outline		
Chapter 2 Review: water vapor, InSAR Atm. Signal; SAR meteorology	Model and Implementation — Chapter 3 Signal decomposition of water vapor	**Chapter 6 Conclusion and future work.**
	Analysis - I — Chapter 4 Point-based comparison between APS and GPS	
	Analysis - II — Chapter 5 Spatial Stochasticity from synchronized data	
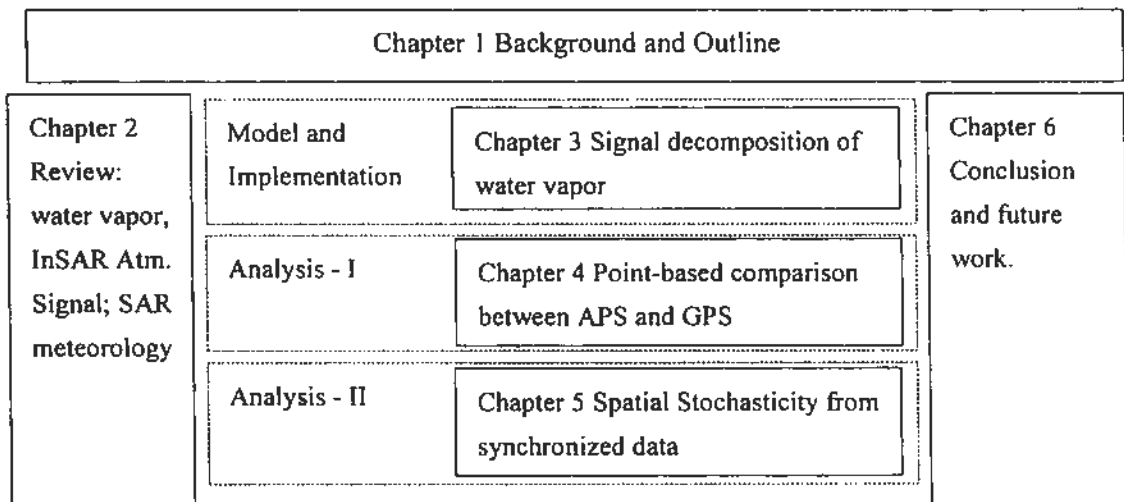
Figure 1.2 Contents and the structures in chapter of thesis.

Chapter 2 Theoretical review

In this chapter, water vapor and its observations from independent sources, point-based or area-based, from various typical technologies are shortly reviewed. And then microwave propagation delay due to atmospheric refractivity and atmospheric signal in SAR Interferometry from refractivity inhomogeneity are briefly reviewed. Following this, meteorological measurement-water vapor-from Interferometric Radar is reviewed in detail. Two meteorological perspective of such Radar Interferometry are provided. The first one is from conventional DInSAR mode. And the other one is from Atmospheric Phase Screen with advanced InSAR techniques, such as PS InSAR. All above content constructs the theoretical basis of our proposed research work in this study.

2.1 Water Vapor and observations

Water vapour is one of the most important variables for meteorological studies. At the same time, it is the meteorological parameter which is least understood. On large scales, it is the principal contributor to the greenhouse effect and plays a key role in our understanding of the climate and its sensitivity to increasing levels of carbon dioxide. On small scales, less than 100 km, the moisture variability at the lower layers of the troposphere is important to know for various disciplines. Knowledge on the fine-scale distribution is important for pin-point forecasting, hydrometeorology and studies of atmospheric radiation. The lack of knowledge of the water vapour distribution constrains the lower bound of the resolution of current Numerical Weather Models.

There are various water vapour observing or retrieving techniques, each with individual strong points and characteristics. To study the fine scale water vapor, conventional water vapour observations are briefly reviewed in following sections.

2.1.1 Water vapor overview

Water vapor is water at gas phase within mixed atmosphere. Water vapor is one state of water within the hydrosphere, the state of which could be altered with changes of environment. Water vapor is mainly constrained by wet partial pressures and temperature in the air. The permitted maximum percentage of water vapor in air - water vapor saturation - is dependent on physical air temperature. The local water vapor concentration could account for as less as a trace near to zero in cold desert regions and up to about 4% over warm tropical oceans.

Dew point temperature and relative humidity act as guidelines for the process of water vapors in the water cycle. The dew point is the temperature to which a given parcel of air must be cooled, at constant barometric pressure, for water vapor to condense into water. Relative humidity is defined as the ratio of the partial pressure of water vapor in a parcel of air to the saturated vapor pressure of water vapor at a prescribed temperature. The dew point is associated with relative humidity. A high relative humidity indicates that the dew point is closer to the current air temperature. E.g. relative humidity of 100% indicates the dew point is equal to the current temperature and the air is maximally saturated with water.

Precipitable Water Vapor (PWV) is the amount of water vapor within a column of atmosphere in the depth of condensed water if all the water in the column were precipitated as rain. PWV is measured in millimeters or gram per square centimeters. The observing and retrieving of PWV in Earth's atmosphere is important for climate studies (Rind 1991), meso-scale meteorology (Emanuel 1995; Crook 1996), numerical forecasting, satellite geodesy and remote sensing. In InSAR technologies, as described in section 2.2, atmospheric effect is nearly dominated by water vapor which varied rapidly both in spatial and temporal scale (Cheng 2009).

In principle, measuring PWV can be classified with two groups: directly or remotely. Direct ways use electronic transducers, moistened thermometers or hygroscopic materials measuring changes in physical properties/ dimensions of water.

14

Remote ways is to retrieve PWV using electromagnetic absorption from active/passive sensors boarded on satellites above planetary atmospheres.

Currently typical applicable methods of measuring PWV are based on platforms including: ground-based observing, upper-air sounding and space-borne satellite sensing/ retrieving. The typical methods as well as their properties to observe and retrieve PWV can be referred to table 2.1. The representative methods in detail which would be referred to in this thesis are summarized as following subsections:

Table 2.1 Conventional methods and platforms to observe PWV

Typical Methods	Technical Feature	Platform	Direct /Remote	Representative products
Meteoro. stations	To record wet partial pressure with physical sensor. Good temporal and poor spatial resolution	Ground-based	direct	wet-and dry-bulb psychrometer; hygrometer
Ground Lidar	Model from scattering signals of water vapor and nitrogen molecules detected by transmitted laser beam.	Ground-based	remote	Raman Lidar; Differential absorption Lidar
Water Vapour Radiometer (WVR)	Measuring the radiant flux (power) of electromagnetic radiation.	Ground-based	remote	Microwave Radiometer; MEMS
Radiosondes	Radioactivity sensor on lifting balloon at radio frequency of 403 MHz or 1680 MHz	Weather balloons-based	direct	-
Infrared/Near Infrared image	Split-window technique, i.e. using different absorptive sensitivity to water vapor in infrared band	Passive; Satellite based	remote	TOVS; AIRS; MODIS; MERIS
Microwave remote sensing	Modeling using highly water absorbing band at 22.0/183.31GHZ (microwave).	Active; Satellite based	remote	AMSU; MMR; SSM/I
GPS (GNSS) meteorology	Retrieve PWV from wet delay after modeling/removal of other geometric terms with permanent continuous stations.	Satellite constellation; Ground based.	remote	IGS PWV (global); PWV from CORS (regional)
Radio Occultation	Retrieve from bending angle of tangent satellite signal.	satellite-based	remote	SAGE-II;CHAMP;FORMOSAT-3

2.1.2 GPS meteorology

Global Positioning System (GPS) is widely used tool through distance signal from orbit determined satellites to retrieve precise geodetic measurement. With designed observing modes and double frequency double code advanced receivers, position with accuracy of mm level, velocity with 0.1mm/s, end user timing of 0.5ns could be obtained.

Similar with SAR interferometry, GPS measurements experiences distance delay from atmospheric refractivity when signal transmitting through air (both troposphere and ionosphere). Such propagation delays were inversely used to retrieve the amount of Zenith Wet Delay (ZWD), provided that hydrostatic term in troposphere could be accurately modeled and ionospheric effect can be precisely compensated. These ZWD measurements were then used to retrieve Precipitable Water Vapor (PWV) amount from finely modeled wet atmospheric delay with GPS observations for meteorological prediction. This technology afterwards was named 'GPS meteorology' (Bevis 1992; 1994). PWV retrieved from GPS meteorology have great significance on hydrology study, meteorological prediction and microwave based satellite observing for geodynamic applications.

Bevis firstly proposed GPS meteorology with claim that PWV in the air could be retrieved from zenith wet delay after subtraction of zenith hydrostatic delay (modeled with ground pressure) from zenith total delay with GPS observations (Bevis 1992). Subsequently a series of systems and applicable results are achieved in overseas and cities in china (Song 2006). With regional (or local) GPS Continuous Observation Reference System (CORS), this GPS meteorology system could provide real time PWV series with half an hour temporal resolution and 1~2 mm accuracy (Dodson 1998).

GPS observing data

Meteorological data

Double-difference processing
(e.g., using Gamit-Golbk)

Parameters retrieving: ZTD, G_{NE},
G_{WE}, M_{DRY}, M_{WET}

Temperature, pressure,
Relative humidity per site

ZHD, SHD; Double –difference;
Residue reanalysis

Average temperature of site

ZWD, then PWV product
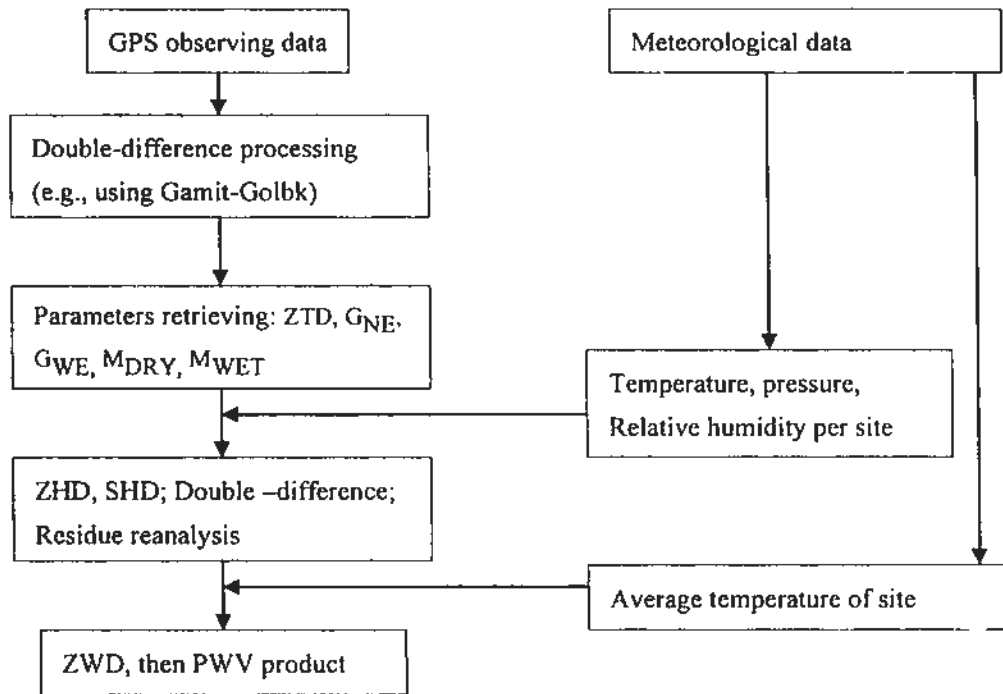
Figure 2.1 Sketch flow of PWV retrieval with GPS meteorology.

The sketch flow of PWV retrieval in GPS meteorology is illustrated in Figure 2.1. To get absolute PWV instead of relative ones, double-differential baseline mode and incorporation of nearby IGS stations with local GPS network was implemented in processing. While IGS final orbits (with accuracy higher than 5 cm), cut-off angle (at 15 °) and geophysical models (e.g. Model of Earth solid tide, pole tide, ocean wave tide) was considered for precisely estimating. With well defined Mapping Function for both dry and wet delay as well as giving piece-wise linear tropospheric model, Zenith Total Delay(ZTD) with 1 hour interval and daily ZTD gradients (in both NS and ES) can be evaluated. Subtracting the hydrostatic part with in-situ meteorological parameters (ground temperature, pressure, humidity) from the estimated ZTD, we can retrieve Zenith Wet Delay (ZWD) and then PWV with a linear scale factor transformation.

2.1.3 Spaceborne spectrometer images

Randel (Randel 1996) and Chaboureau (Chaboureau 1998) firstly propose implementing space missions to monitor water vapor, including Television and Infrared Operational Satellite (TIROS), Operational Vertical Sounder (TOVS),

Special Sensor Microwave/Imager (SSM/I) and etc. Thereafter atmospheric water vapor has been measured with the one MERIS (Medium Resolution Imaging Spectrometer), and the two NASA MODIS (Moderate Resolution Imaging Spectro radiometer) instruments.

a) MODIS

The MODerate-resolution Imaging Spectroradiometer (MODIS) was launched on board Terra (EOS AM, NASA in 1999) satellite, and Aqua satellite (EOS PM, in 2002). The MODIS instruments is a passive imaging spectra- radiometer capturing radiometric signal in 36 spectral bands ranging in wavelength from 0.4 μm to 14.4 μm at three spatial resolutions (2 bands at 250 m, 5 bands at 500 m and 2 29 bands at 1 km). With temporal cycle of 1~2 days, thousands of km coverage, MODIS are advantageous to study large-scale global atmosphere dynamics including cloud cover, radiation budget, water vapour, and aerosol etc.

Among all 36 bands, channels centered at 0.940um, 0.936um, 0.905um are very sensitive for atmospheric water vapour. Considering above three channels present different preference (0.936 um is preferential for dry conditions, 0.905um for humid condition or low solar elevation angle) (Li Z.H. 2006), mean PWV is obtained by average of water vapor from model of each band as following (Gao and Kaufman 1998):

$$PWV = f_1 W_1 + f_2 W_2 + f_3 W_3 \qquad (2.1)$$

In equation 2.1, W_i is value from each channel, and f_i is corresponding weighting function which defined on the sensitivity of radiative transmission in each channel.

Near-infrared PWV and infrared PWV are respectively included in MODIS product MOD_05_L2 and MOD_07_L2. The level 2 data are produced at 1*1km spatial resolution using the near infrared algorithm during the day, and at 5*5km resolution both day and night using infrared algorithm when at least 9 fields of view (FOV) are cloud free. In practice, Near-infrared PWV is more preferential because of

higher resolution and stable accuracy, while Infrared PWV can still provide assist to Near Infrared PWV such as cloud cover information.

Gao and Kaufman claimed an accuracy of 5-10% determined by MODIS-PWV (Gao and Kaufman 2003). The theoretical accuracy of the algorithm to re retrieve the PWV from MERIS is 1.6 mm under cloud free conditions over land (Bennartz and Fischer 2001) and between 1 mm and 3 mm above clouds (Albert et al., 2001). The accuracy of estimation of the total amount of atmospheric water vapor is expected to be less than 20% over water surfaces (Fischer and Bennartz 1997). As suggested by Kanuman and Gao, errors in derived Near Infrared water vapor are estimated with 5~10% typically and 14% extremely under hazy condition of relative PWV (Gao and Kanuman 2003)

b) MERIS

MERIS (MEdium Resolution Imaging Spectrometer) is a useful optical sensor of European ENVISAT for atmospheric studies. MERIS image is an important tool for atmosphere monitoring and extraction of atmospheric parameters. The sensor consists of 15 spectral bands in visible and near infrared regions of electromagnetic spectrum. One of the most important capabilities of these images is the column water vapor estimation. The column water vapor content is calculated in level 2 data of MERIS as one of MERIS products (ESA 2006). Total Precipitable water vapor content was estimated in earth-sensor direction, with a quadratic model of ration between the band 14 at 0.885um and water absorption band 15 at 0.900um as following (Fischer and Bennartz 1997).

$$PWV = k_0 + k_1 \log(\frac{L_{15}}{L_{14}}) + k_2 \log^2(\frac{L_{15}}{L_{14}}) \qquad (2.2)$$

In equation 2.2, PWV is column amount of water vapour, L_{15} and L_{14} are radiance at band 15 and 14 respectively, and k_i are constant coefficients derived by inverting the observations of radiative transfer model.

19

MERIS Water vapor products provide two spatial scales: 300m Full Resolution (FR) and 1200m Reduced Resolution (RR) of PWV (ESA 2006). Dataset in Water Vapor products consists of geolocation information, cloud cover and features, column water vapor and other accessorial information. The nominal estimated accuracy of product is 10% of relative water vapor amount -1.6mm under cloud free conditions and between 1mm and 3mm above could (Bennartz and Fischer 2001; Albert 2001).

2.1.4 Numerical Weather Predication (NWP) Models

Numerical Weather Predication (NWP) model is computer program sets that input current weather conditions into mathematical models of the atmosphere and output meteorological information in future time at given positions and altitudes for the physics and dynamics of the atmosphere. As non-linear complex system, mathematical models are solved by numerical computerized methods. Approximate solutions are obtained in different methods. For global scale, spectral methods for the horizontal dimensions, finite difference methods for the vertical dimension are adopted, while regional models employ finite-difference methods in all three dimensions, and smaller-scale meteorological phenomena was resolved by finer grids (Thompson 1961).

Models are initialized using observed data, e.g. radiosondes, weather satellites, and surface weather observations. Observations are processed by data assimilation and objective analysis methods as a starting point for a forecast in the model. A time stepping strategy was adopted to iteratively predict the state of the atmosphere at next time step with known state at current time step giving mathematical primitive equations, until reaching the desired forecast time. The length of the time step is related to grid resolution, varying from tens of minutes in global scale to even a few seconds for fine regional scale (Kalnay 2003).

MM5 is a nonhydrostatic mesoscale NWP model designed to simulate atmospheric circulation by National Center for Atmospheric Research

(NCAR)/Pennsylvania State University (Grell 1994). MM5 has a multiple-nested capability with increasing resolution in horizontal domain and surface pressure dependent multi-scale in vertical profiles.

Main input data of MM5 consist of reanalyzed data - a set of meteorological parameters on a regular geographic and time sampling obtained by assimilation of several meteorological measurements, include: pressure, temperature, humidity etc. Other input data for MM5 are land use maps, elevation model, land-water mask, soil types, vegetation fraction and soil temperature (Dudhia 2005).

Output products of MM5 model include temperature T(K), total pressure P(mbar), water vapor mixing ratio Q (kg/kg) and cloud water mixing ratio Qcloud (kg/kg). From water vapor mixing ratio profiles, PWV could be retrieved as (Mobasheri 2008):

$$\text{PWV} = -\frac{1}{\rho_w g_m} \int_{p0}^{0} q\,dp \qquad (2.3)$$

In Equation 1.3, ρ_w is density of water 1000kg/m^3, g_m is mean acceleration due to gravity in m/s^2, q is specific humidity calculated from water vapor mixing ratio, p is atmospheric pressure.

2.2 Radar Interferometric Atmospheric signal

Returning to the starting point of our thesis, in this section, radar interferometric atmospheric signal are reviewed. As repeat pass is the most typical and applicable work mode of SAR interferometry, InSAR in repeat pass mode and the atmospheric signal on its phase measurements is then shortly reviewed.

2.2.1 Radar Interferometric Phase measurements

According to Doppler principle - key principle of Synthetic Aperture Radar imaging, the relationship of Doppler frequency and rang could be as follows:

$$f_{Dop} = -\frac{2\partial\rho}{\lambda\partial t} \qquad (2.4)$$

Here ρ is slant range, λ is wavelength, t is time of ranging. With consideration of frequency definition:

$$f = \frac{\partial \varphi}{2\pi \cdot \partial t} \tag{2.5}$$

Integrating equation 2.4 and 2.5, phase could then be represents as eq. 2.6

$$\partial \varphi(t) = -\frac{4\pi}{\lambda} \partial \rho(t) \tag{2.6}$$

Figure 2.1 illustrates the geometry of repeat pass SAR interferometry. H is orbit height; B is the baseline of S1 and S2, which are sensor positions at time t1 and t2. At the same period, the ground target point moves from P to P' with assumed deformation vector D but constant elevation height h, while SAR signal transmits one way slant distance of ρ_1 and ρ_2 accordingly. If we mark acquisition time of master image as t1, then slave as t2, the signal in complex form for both acquisitions could be given by equation 2.7.

$$
\begin{aligned}
s_1 &= |s_1| \exp(j\varphi_1) \\
s_2 &= |s_2| \exp(j\varphi_2)
\end{aligned}
\tag{2.7}
$$

After the coregistration and resampling of slave image to geometry of master image, the interferometric signal is multiply of master by conjugated slave signal.

$$s_1 s_2 = |s_1||s_2| \exp[j(\varphi_1 - \varphi_2)] \tag{2.8}$$

Integrating equation 2.8 and 2.6, interferometric phase could be:

$$
\begin{aligned}
\varphi &= \varphi_1 - \varphi_2 \\
&= -\frac{4\pi}{\lambda}(\rho_1 - \rho_2)
\end{aligned}
\tag{2.9}
$$

Figure 2.2 Geometry of repeat pass SAR Interferometry, adapted from Wang, 2006.

In figure 2.2, giving approximation that SAR line of sight (LOS) in time t1 and t2 are nearly parallel, and the baseline of orbit in normal can be neglectable, the interferometric phase is further deduced as follows by graphic quadrilateral vector.

$$\phi \approx -\frac{4\pi}{\lambda}(B \cdot l_1 - D \cdot l_1)$$

$$= -\frac{4\pi}{\lambda}[B\sin(\theta - \alpha) - \Delta\rho] \qquad (2.10)$$

From spatial geometry, we know l is unit vector in master LOS direction, θ is incident angle of master image, α is elevation angle of baseline. $B\sin(\theta - \alpha)$ is called parallel baseline (and $B\sin(\theta - \alpha)$ is called perpendicular baseline $B_\perp$) and $\Delta\rho$ is projection of ground deformation in LOS direction.

Expanding with Taylor Series, equation 2.10 then is rewritten with a more general form as equation 2.11:

$$\phi = -\frac{4\pi}{\lambda}(B_{\prime\prime} + \frac{B_\perp^{\prime\prime}}{\rho_1\sin\theta_0}h - \Lambda\rho) \qquad (2.11)$$

Equation 2.11 equals to equation 2.12 if we decompose interferometric phase into three components: reference interferometric phase, topographic interferometric phase and deformation interferometric phase.

$$\phi = \phi_{ref} + \phi_{topo} + \phi_{defo}$$

$$\phi_{ref} = -\frac{4\pi}{\lambda} B_{\parallel}^{o}$$

$$\phi_{topo} = -\frac{4\pi}{\lambda} \frac{B_{\perp}^{o}}{\rho_1 \sin\theta_0} h \qquad (2.12)$$

$$\phi_{defo} = \frac{4\pi}{\lambda} \Delta\rho)$$

The mathematical model given by equation 2.12 is only approximate to physical model of InSAR. Inaccuracy of satellite orbits at the time of radar image acquisition, signal delay by heterogeneity of atmospheric refractivity in radar transmission and errors resulting from thermal noise internal to radar system as well as coherence loss between individual SAR observations would all produce artificial phase terms in SAR interferogram. The composition of interferometric phase in equation 2.12 can be expanded as following:

$$\phi = \phi_{ref} + \phi_{topo} + \phi_{defo} + \phi_{orbit} + \phi_{atm} + \phi_{noise} \qquad (2.13)$$

Equation 2.13 is most general formula of interferometric phase with consideration every compositional term as follows:

1) Reference term, due to curvature of Earth ellipsoid;

2) Topographic term, due to height of target above the reference geoid;

3) Deformation term, due to LOS range changes by target deformation;

4) Orbit term, due to inaccuracy of satellite orbit;

5) Atmospheric term, due to inhomogeneity of atmospheric refractivity;

6) Noise term, due to thermal noise and other signal decorrelation.

2.2.2 Atmospheric refractivity

All the microwave signals, from spaceborne platform to earth surface, propagating through the atmosphere, are enduring atmospheric refractivity. So do

microwave signal in SAR Interferometry, as described in equation 2.13. In this subsection atmospheric refractivity is briefly reviewed.

Atmosphere is a layer mixed with kinds of discrete gases surrounding the earth ellipsoid by Earth gravity. Earth's atmosphere mainly contains 78.09% nitrogen (in molar content/volume), 20.95% oxygen - together making up 99.03% of volume of clean dry air, and other minor gases, such as water vapor , argon, carbon dioxide etc. The composition of Earth's atmosphere varies temporally and spatially, e.g., water vapor and carbon dioxide.

Due to the Earth's gravity and reaction to solar radiation, the atmosphere exhibits different physical properties in different sub layers. According to variation of physical temperature on altitude, atmosphere, from bottom to top, could be divided into troposphere, stratosphere, mesosphere, thermosphere and thermosphere.

Troposphere, with average thickness around 12 km and decrease ratio of temperature at 0.65 Celsius degrees per hundred meters, is situated at bottom layer. As investigated, 80% atmospheric mass (Mason 2001) and 99% atmospheric water vapor (Mocker 1995) are held in troposphere. Dry (wet) air accounts for about 80% (20%) of total volume in troposphere respectively. Troposphere and stratosphere are non-dispersive medium. Their impact on microwaves is not dependent on signal frequency. Therefore, above layers are also called neutral atmosphere.

In perspective of ions concentration, layer of atmosphere, extending from height of about 50km to infinite could be called ionosphere, including mesosphere, thermosphere and outer part of atmosphere, in which fairly large density of ions and free electrons exist. The density of ions changes with local diurnal time, geographic location and intensity of solar activity (Odijk 2002). Each sub-layer of ionosphere with different height range also has different ratio of production and vanishing of free electron (Schaer 1999).

The velocity vector (both magnitude and direction) of microwave signal in transmission through atmosphere can be altered; this phenomenon is referred to refractivity. Giving definition of simplified refractive index N as:

$$N = 10^6(n-1) = 10^6(\frac{c_0}{c} - 1) \qquad (2.14)$$

In equation 2.14, c_0 and c are speed of light in atmosphere and vacuum respectively. Physically, the effect of refractivity could be divided into two ways: the first one is altering of velocity magnitude, usually called signal delay. And the other one is changing of direction of velocity vector, usually called signal bending. From previous study, the bending part could be neglected when signal zenith angle less than 87° even in extreme refractivity (Bean and Dutton, 1968). Then delaying is, in nearly all cases, the only effective atmospheric refraction effect in microwave signal transmission if without special discrimination in later context.

According to above analysis of atmospheric structure and refractivity, neglecting insignificant effect on refractivity by other air trace elements such as clouds, aerosols, volcanic ash and etc. (Li Z.H. 2005), refractivity N can be generally decomposed as: (1) dry refractivity; (2) wet refractivity; (3) ionospheric refractivity; (4) refractivity induced by liquid water. Here, refractivity by liquid water in rainy weather conditions is additional considered.

$$N = N_d + N_w + N_{ion} + N_{liq} \qquad (2.15)$$

Correspondingly, the microwave propagation delay due to such atmospheric refractivity could be composed of following four parts: dry delay, wet delay, ionospheric delay and delay induced by liquid water.

$$l = l_d + l_w + l_{ion} + l_{liq} \qquad (2.16)$$

2.2.3 Radar Interferometric Atmospheric delay

Returning to phase measurements of SAR interferometry, following the equation 2.15 and 2.16, the atmospheric delay of interferometric phase in zenith

26

could be correspondingly represented by four major components of refractivity in equation 2.17 as follows:

$$l_{atm} = l_{ZHD} + l_{Zwd} + l_{ion} + l_{liq} \qquad (2.17)$$

Based on principle of Doppler, atmospheric radar phase is proportional to distance delay induced by refractivity when radar signal transmitted through the air. Radar atmospheric delay is doubly counted since SAR sensor sends the signal and receives the returning signal backscattered from the ground. Similar with equation 2.4 and 2.6, atmospheric phase φ due to delayed distance l could be:

$$\begin{aligned} \varphi_{atm} &= -\frac{4\pi}{\lambda}(l_{atm}) \\ &= -\frac{4\pi}{\lambda}(l_{ZHD} + l_{Zwd} + l_{ion} + l_{liq}) \end{aligned} \qquad (2.18)$$

In equation 2.17, we can ignore the ionospheric delay since the locally uniform ionosphere scenario gives no inhomogeneity on SAR interferogram in less than 50km. Liquid water delay can also be neglected because the amplitude is less than 1mm under usual atmospheric circumstances (Hanssen 2001). With above simplification atmospheric delay in equation 2.17 only contains zenith hydrostatic delay ZHD, and water vapor induced zenith wet delay ZWD. With consideration that Mapping Function for ZHD and ZWD are required to transform atmospheric delay in Zenith into radar atmospheric delay in line of sight, atmospheric phase can be rewritten as follows by incorporating simplified equation 2.17 into 2.18.

$$\varphi_{atm} = -\frac{4\pi}{\lambda}\left(\frac{ZHD}{MAP_H} + \frac{ZWD}{MAP_W}\right) \qquad (2.19)$$

Mapping functions in equation 2.19 are differs for ZHD and ZWD, but both are only dependent on signal incident angle. Interferometric atmospheric phase is represented as differential atmospheric phase of two image acquisitions. Since interferometric baseline (no more than 1000m) is far less than distance (more than 100km) between satellites and ground, without changes of incident angle, Mapping Functions during two epochs could be supposed unchanged:

$$\phi_{atm} = -\frac{4\pi}{\lambda}(\frac{ZHD_1 - ZHD_2}{MAP_H} + \frac{ZWD_1 - ZWD_2}{MAP_W}) \qquad (2.20)$$

Because that the phase in unwrapped interferogram is the phase difference with respect to reference point of unwrapping and that ground deformation is also referenced to ground stable point (reference point). Only spatially & temporally relative tropospheric delay (by the tropospheric heterogeneity) between two SAR image points and between two SAR image acquisitions will distort the interferometric phase in InSAR. Considering that ZHD is homogeneous in different echoes (accuracy of most ZHD models is better than 1mm), the atmospheric phase induced by hydrostatic part could be neglected in SAR interferogram and deformation signal retrieval. From equation 2.20, atmospheric interferometric phase could be represented as ϕ_{atm} with only wet part.

$$\phi_{atm} = -\frac{4\pi}{\lambda}(\frac{ZWD_1 - ZWD_2}{MAP_W}) \qquad (2.21)$$

It has been demonstrated that Precipitable Water Vapor (PWV) has linear relationship with ZWD.

$$PWV = \prod \times ZWD \qquad (2.22)$$

$\prod$ is scale factor (or conversion factor). PWV linear scale factor $\prod$, though varying mildly in different zones of world, would keep stable regionally (Li Z.W. 2007). Then the atmospheric interferometric phase could be represented by PWV as follows:

$$\phi_{atm} = -\frac{4\pi}{\lambda}(\frac{PWV_1 - PWV_2}{\prod \cdot MAP_W}) \qquad (2.23)$$

2.2.4 Water Vapor sensitivity

Previous published research papers have demonstrated that how Repeat-pass InSAR measurement are affected by atmospheric delay (Zebker 1997; Li Z.H. 2006). In this section we deduce the sensitivity of water vapor accuracy on uncertainty of interferogram phase as well as in deformation in Line of Sight. Then we quantitatively study the sensitivity analysis of PWV with typical SAR imagery and working mode considering atmospheric signal.

28

For analysis of atmospheric effect on InSAR, we trace back to equation 2.13 in section 2.2. In equation 2.13 for focus of atmospheric component, we ignore interferometric phase error due to inaccuracy of satellite orbit baseline, thermal noise and signal decorrelation, while combine the reference interferometric phase and topographic interferometric phase into an integrated constant term ϕ_0, which can be accurately modeled from Earth ellipsoid and external DEM (or height derived from topographic interferometric pair). Then equation 2.13 can be rewritten as follows:

$$\phi = \phi_0 + \phi_{defo} + \phi_{atm} \tag{2.24}$$

To substitute component of interferometric phase in equation 2.24 by equation 2.12, and 2.23 then we get:

$$\phi = -\frac{4\pi}{\lambda}(l_0 - \Delta\rho + \frac{PWV_1 - PWV_2}{\prod \cdot MAP_w(\theta)}) \tag{2.25}$$

As pointed out, the observed interferometric phase is practically referred to one reference point, and then interferometric phase is spatially relative as:

$$\phi_\Delta = -\frac{4\pi}{\lambda}(l_{0\Delta} - \Delta\rho_\Delta + \frac{PWV_{1\Delta} - PWV_{2\Delta}}{\prod \cdot MAP_w(\theta)}) \tag{2.26}$$

In equation 2.26, $\Delta\rho_\Delta$ is ground deformation in LOS relative to reference point, $PWV_{i\Delta}$ is spatially differential PWV in epoch of i. $MAP_w(\theta)$ is function of θ incident angle.

If PWV in different spatial location observed in different acquisitions are independent with same standard deviation σ_{pwv_i}, according to law of error propagation, we can deduce the effect of PWV deviation on the uncertainty of SAR Interferometric phase.

$$\sigma_{\phi\Delta} = \frac{8\pi}{\lambda} \cdot \frac{1}{\prod \cdot MAP_w(\theta)} \cdot \sigma_{pwv} \tag{2.27}$$

With transformation of equation 2.26, $\Delta\rho_\Delta$ could be represented as:

$$\Delta\rho_\Delta = \frac{PWV_{1\Delta} - PWV_{2\Delta}}{\prod \cdot MAP_w(\theta)} + \frac{\lambda}{4\pi}\phi_\Delta + l_{0\Delta} \tag{2.28}$$

29

Then effect of PWV deviation on the uncertainty of deformation retrieval is:

$$\sigma_{\Delta\rho} = \frac{2}{\prod \cdot MAP_W(\theta)} \cdot \sigma_{PWV} \qquad (2.29)$$

From equation (2.27) and (2.29), standard deviation error on interferometric phase and retrieved LOS deformation signal by PWV (water vapor in atmosphere) for currently typical SAR imagery including: ENVISAT ASAR, ALOS PALSAR, RadarSat 2, TerraSAR-X and Cosmos Sky-Med SAR are exemplified. In this exemplification, we take linear scale factor as constant of 0.162 in Hong Kong (Li Z.W. 2007). Additionally, we select cosine of incident angle as approximate mapping function to simplify our prediction. The PWV affected standard deviation error could be referred to table 2.2.

Table 2.2 Standard deviation error on interferometric phase and deformation induced by PWV for typical SAR Imagery.

PWV RMS (1mm) SAR imagery	Average incidence angle	STD (rad). Interferometric phase	STD(mm)LOS Deformation
Envisat ASAR(Swath 2)	23.0°(19.2°~26.7°)	3.00	13.40
ALOS PalSAR(FineMode)	34.3°(8°~60°)	0.79	14.95
RadarSat2(Standard, Wide,ScanSAR mode)	34.5°(20°~49°)	3.39	14.99
TerraSAR-X	32.5°(20°~45°)	5.91	14.63
COSMO-SkyMed	40.0°(20°~60°)	6.53	16.11

From Table 2.2, we can theoretically conclude that the observation accuracy of 1.0mm (rms) PWV would bring uncertainty (STD) with level of 15 mm of retrieved deformation signal in LOS detected by InSAR with typical SAR imagery (sensors). The conclusion on one hand declares the great magnitude of atmospheric signal on InSAR, e.g., influence of water vapor on interferometric phase and deformation signal, and on the other hand clearly shows the importance of water vapor modeling in atmospheric mitigation in traditional InSAR monitoring technology.

2.3 Water vapor from Interferometric Radar

SAR interferometric Water vapor retrieval, compared to DEM reconstruction and earth surface deformation monitoring, is quite a virgin area but promising research filed. Meteorological knowledge (e.g. water vapor) can be obtained from InSAR technology by compensating the topographic and deformation induced phase and identifying the atmospheric contributive phase component. The concept is called Interferometric Radar Meteorology (IRM), which was firstly invented by Hanssen (Hanssen 1999; Hanssen 2001). And an exploratory water vapor study based on IRM concept has been firstly carried out by Hanssen in Delft. Hanssen and his group (Hanssen 2003) then proposed a methodology solving the acquisition ambiguity caused by double differential of radar retrieved water vapor. Based on huge amount of data set, Pierdicca, Rocca etc. from POLIMI compared the water vapor from NWP (Numerical Weather Prediction) model and SAR APS (Pierdicca 2009).

Compared to InSAR in topographic mapping and deformation monitoring, SAR interferometric water vapor retrieval has being less recognized in a long time. The water vapor study with this technology is only at preliminary exploratory stage. While compared to wide spatial coverage and extremely high resolution, water vapor from SAR Interferometry has profound significance and promising future.

2.3.1 Interferometric water vapor from DInSAR

The concept of Interferometric Radar Meteorology (IRM) was firstly invented by Hanssen (Hanssen 1999; Hanssen 2001). Based on IRM concept, an exploratory water vapor study has been firstly carried out in Delft. In the years before and around 2000s, Differential InSAR (two tracks with DEM, three tracks, four tracks and multiple tracks) strategy is the common mode in data processing. So during the period of first several years after birth of IRM, this technique is studied based on DInSAR processing strategy.

31

At the beginning of InSAR developing stage, Interferometric Radar Meteorology was implemented by DInSAR strategy. There are some common modes within this technique to study atmospheric effect in conventional InSAR techniques.

1) Tandem interferogram, i.e. ERS1 and 2 interferogram with 1 day interval.

2) Short Interval interferograms with the assumed ground motion model.

For the first case, since the temporal interval is only 1 day, the deformation of ground can be neglected and the interferometric coherence was usually high. Removing the topographic contribution with external DEM, the residual phase can be regarded as atmospheric phase and noises. The principle of different contributive components to interferometric phase could be referred to the mathematical model in section 2.2. The left one of figure 2.3 shows the differential water vapor signal with peak to peak variation of +/- 3mm retrieved from one Tandem SAR interferograms with DInSAR strategy. The signal has been proved to be informative and coherent with precipitation rate observed by temporally synchronous and spatially overlapped weather radar images (fig. 2.3, right) in the region near Netherland (Hanssen 2001).
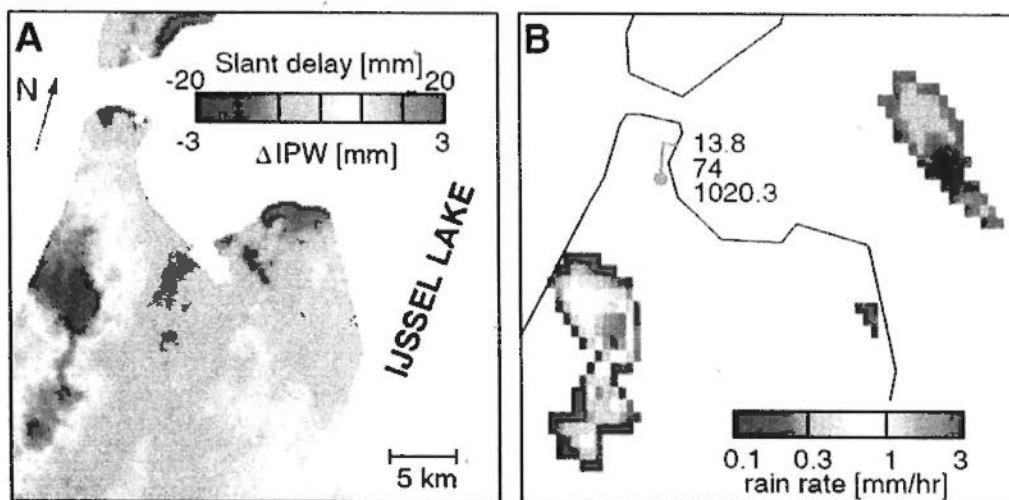
Figure 2.3 Water Vapor from radar interferometric meteorology in DInSAR mode. Left: Differential Integrated Precipitable Water Vapor (mm) from DInSAR in Netherland. Right: Precipitation observed by weather radar, courtesy of Hanssen.

For the latter case, an assumption is given that the concerned spatial area is endured with no deformation, while this could be accepted in most area of worldwide

territories. The alternative choice is to model the deformation trend with external surveying data, e.g. Leveling and GPS Real Time Kinematic (RTK) positioning. With above assumption and to neglect or remove such deformation signal in a given period, the atmosphere contributive signal can be obtained with removal of the topographic contribution.

With the retirement of ERS 1, tandem interferograms with 1 day temporal baseline cannot be used for atmospheric identification. So up to now, the first mode of DInSAR meteorology is not available. Mean while, the atmospheric noise in DInSAR are mixed with other model errors, as introduced in hanssen (Hanssen 2001). Orbital inaccuracy, small unmodeled deformation signal and noises cannot be clearly distinguished from total signal. There for, even with the second mode of DInSAR strategy, the water vapor from InSAR for meteorological use confronted much difficulty due to the stability and accuracy.

2.3.2 Water vapor from Atmospheric Phase Screen (APS)

After 2000s, Permanent Scatters (PS) InSAR has gained more advantage than traditional DInSAR technology. PS InSAR technique was first developed to detect isolated coherent pixels and estimate (and remove) the atmospheric effects at the expense of a large number of required images (at least 25-30 images) and a sparse pixel-by-pixel based evaluation by Ferretti et al in 2000 (Ferretti 2000; 2001). With the theoretical innovation and practical development of PS InSAR, which is representative of advanced InSAR processing techniques and marks the recent milestone of InSAR technology, water vapor retrieval based on Atmospheric Phase Screen (APS) from PSInSAR implicates that IRM has moved into new stage. In theory, the local water vapor in urban area could be modeled with dense PS points by mm level. Though the full potential and limitation shall be studied in chapter 3 to 5, the principle of APS base IRM is briefly reviewed in this section.

1) PSInSAR

Permanent Scatterers (PS) InSAR was developed in 2000s, as most typical advanced InSAR technique compared to conventional D-InSAR. PSInSAR was firstly proposed by Freretti at al. in POLIMI presenting a complete algorithm for the identification and exploitation of stable natural reflectors or permanent scatterers (PSs) starting from long temporal series of interferometric SAR images to overcome the previously unsolved problems of signal decorrelation, atmospheric disturbance and DEM residual effects (Freretti 2000; 2001).

Though with different handling techniques in realization, such as policies of graphic interferogram combination from SAR series, criteria of selection of stable points, algorithm of triangle network generation from stable points, and retrieving techniques of deformation from phase models, subsequent SBAS (Berardino 2002) and CT (Mora 2003) techniques have same mathematic model of interferometric phase series with PS on spatial network of spatial scatterers. If we take ϕ as interferometric phase matrix on PS points, the function model could be given as (Ferretti 2001):

$$\phi = al^{\tau} + P_{\xi}\xi^{\tau} + P_{\eta}\eta^{\tau} + Bq^{\tau} + Tv^{\tau} + E \qquad (2.30)$$

In equation 2.30, a is constant, P_{ξ}, P_{η} are linear phase coefficients in azimuth ξ and range η, B is perpendicular baseline, q is residual phase term induced by DEM, T is temporal differences between master and salve images, v is deformation velocity in LOS of PS points, E is residual phases, including non-linear atmospheric phase, non-linear deformation phase and noises.

The k^{*} interferometric phase of PS point i relative to stable reference PS point 0, giving with $\Delta\phi_{i0}{}^{\kappa}$, could be expanded as follows (Ferretti 2001):

$$\Delta\phi_{i0}{}^{\kappa} = [C_{b} \cdot B^{\kappa} \cdot \Delta q_{i0} + C_{v} \cdot T^{\kappa} \cdot \Delta v_{i0}] + \mu_{NL} + \alpha^{\kappa} + n \qquad (2.31)$$

In equation 2.31, Δq_{i0} and Δv_{i0} are spatially relative residual DEM and deformation velocity respectively between two PS points, C_{b} and C_{v} are design matrix for unsolved variable: residual DEM and deformation velocity. $\mu_{NL} + \alpha^{\kappa} + n$,

which is differenced from in equation 2.30, is a relative term of residual phase mixed with non-linear deformation, atmospheric phase and noise. After linearization, the equation 3.2 can be solved (i.e. each unknown variable: residual DEM, deformation velocity can be estimated) under provision that: 1) high PS SNR; 2) the constant velocity model; and 3) estimation in small area (Ferrite 2001).

2) Water Vapor from APS

One of the main differences between conventional InSAR and PS InSAR is the capability to estimate the atmospheric contribution, generally referred to as Atmospheric Phase Screen (APS) (Ferretti 2005). APS is newly named after development of PS-InSAR to nominate the atmospheric phases screened in interferometric phase model. Colesanti et al showed that in the estimated APS, i.e. the sum of two-phase contributions, including atmospheric effects and orbital error terms, the latter part do not change the low wave number character of the atmospheric signal since it only corresponds to low-order phase polynomials (Colesanti 2003). Therefore, in practice, APS estimated by the PS technique gather all phase delays that independent on the target elevation and on the modeled deformation. Thus, APS include not only pure atmospheric phase, but also phase terms due to orbital errors or unknown spatially-dependent phase terms.

The whole algorithm to inversely retrieve the water vapor by means of PS InSAR is implemented through three main steps (Ferretti 2001; Perissin 2010).

First, height and deformation trend of targets are estimated by reducing as much as possible the humid contribution. The goal is achieved by analyzing neighboring targets that have good probability to be coherent. An a-priori index (usually the amplitude stability index (Ferretti 2001)) is used for the initial selection of the PS Candidates (PSC). Then an ensemble of connections between neighboring PSC's is created (a spatial graph where the vertex are the PSC's). The temporal phase series associated to each connection is inverted searching for the relative height and deformation trend. The variance of the phase residuals is used to quantify the

estimate. The phase residuals depend on noise and slight atmospheric changes between the analyzed neighboring targets.

The second step of the algorithm is then the integration of the small atmospheric contributions through the spatial graph. The problem relates to the spatial unwrapping of phase residuals in presence of noise (Ghiglia 1996) and it is solved due to the high over-determination given by the redundancy of connections of the graph (many connections for each PSC). The result of the spatial phase unwrapping is thus a sparse estimate of the atmospheric phase delay in the analyzed area for each interferogram, commonly called Atmospheric Phase Screen (APS).
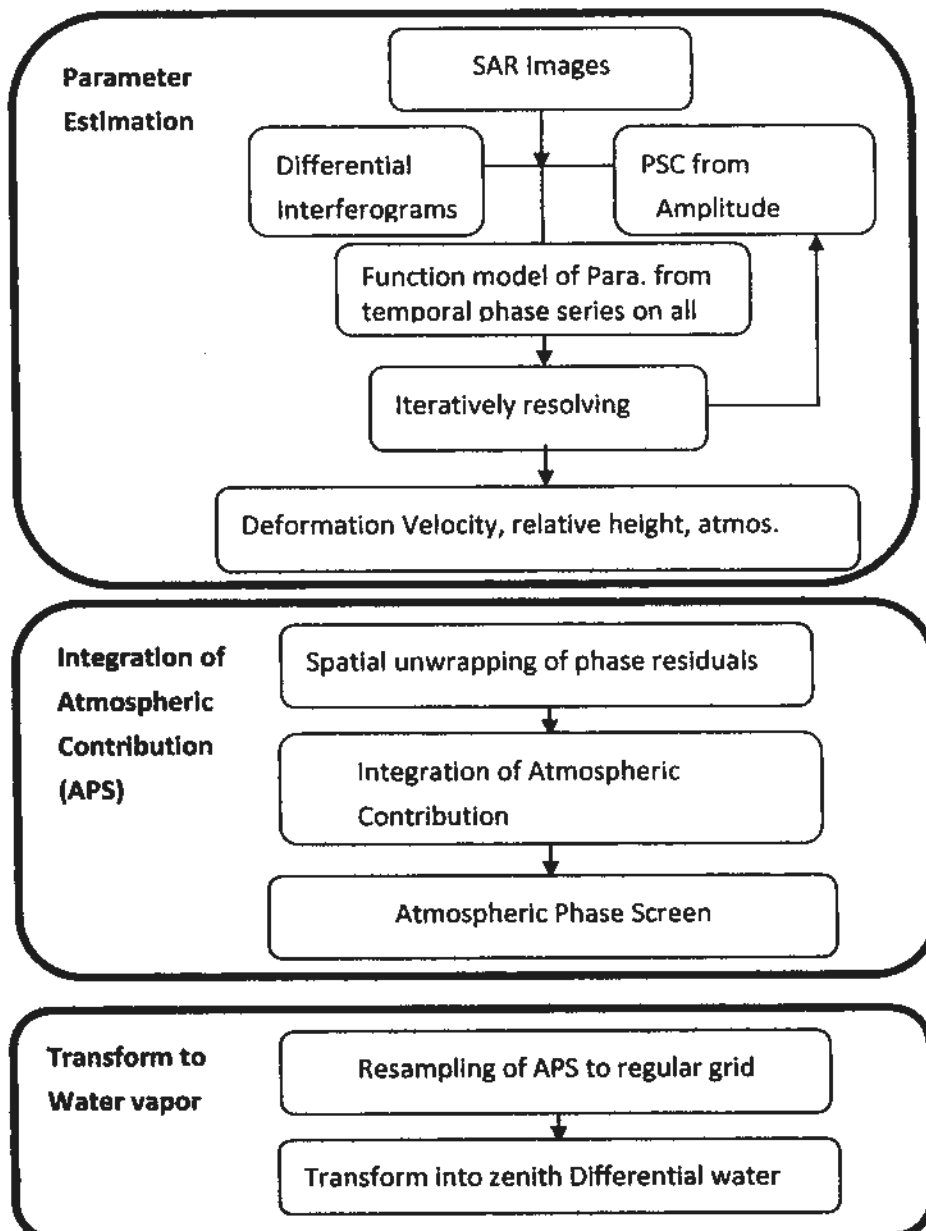
Figure 2.4 Water Vapor retrieval chain from SAR interferometry based on PSInSAR strategy.

The third step of the algorithm is re-sampling the APS on a regular grid and transforming APS into differential water vapor. Kriging process is implemented in this operation (Wackernagel 1998), in which the distance between the spatial data are taken into account and the APS are recalculated by fitting form original samples. With a mapping function of local incidence angle, APS in two way radar line of sight in radiance is then transformed into zenith delay (differential between two epochs), and then into differential water vapor by a local linear scale factor (conversion factor from wet delay to water vapor), as explained in equation 2.22. Figure 2.4 illustrate the processing chain of water vapor from above PS InSAR strategy.

But though APS in these years could be stably obtained as by product form PS InSAR technique, there is still unelectable gap between water vapor form this technology for water vapor study and meteorological application. The main drawbacks of the technique for above purpose lie in: (i) Firstly, the decomposition of the atmospheric signal of InSAR into meteorological parameters such as water vapour is still lagged. Although at least 90% of the observed signal is due to the water vapour distribution, other factors still play contributive roles in water vapor distribution and variation. (ii) Second, atmospheric signal from interferometric technique represents the temporal difference of atmospheric stages and hence cannot directly interpreted into or compared with absolute observed values. Therefore, though PSInSAR technology has been developed with ten years and widely applied in various geophysical applications, the water vapor study and meteorological application of PSInSAR still stay at a preliminary stage. More experiments and efforts for speeding up its development are required.

2.4 Summary

Typical independent water vapor observations are reviewed in section 2.1. The section 2.2 briefly reviews the principle of atmospheric signal in SAR interferometry.

In section 2.3, concept of water vapor from Interferometric Radar Meteorology, in DINSAR working mode and PS InSAR mode are reviewed.

Water vapour is one of the most important variables for meteorological studies. It is one of the most important meteorological parameters, which plays important role in could formation and precipitation, and also gives critical limitation in high precision microwave satellite observation. Therefore water vapor is the direct target of this research.

Conventional means for collecting water vapour data include radiosondes, surface-based radiometers, satellite radiometers, and GPS networks. Each of these systems has limitations, ranging from spatial sampling, spatial extent, vertical sampling, temporal sampling, data accuracy and to the cost of operation.

Spaceborne Interferometric Radar Meteorology would introduce an incredibly high spatial resolution, extremely accurate water vapor data, against relatively low costs as a spin-off product. Compared to DInSAR strategy, PSINSAR meteorology conquers the sensitivity to land cover changing and technical difficulty over vegetated and humid areas as well as over longer time intervals. It can be concluded that it is a complementary water vapor source that are impossible to observe with any other means.

As discussed in last section, the limitation of Permanents Scatterer SAR interferometric meteorology is objectively existent. This technology for water vapor studies requires more efforts in two aspects: (i) the signal components model of water vapor (ii) Second, reasonable interpretation or linking to absolute water vapor observations. Therefore in this thesis, focusing on the study of water vapor, and taking advantage of SAR interferometric meteorology, the water vapor spatial and temporal statistical properties in fine scale have been studied.

Chapter 3 Model and differentiation of water vapor components

A component model of water vapor is introduced in this chapter. In the mode, acquired water vapor is regarded as the superimposition of four signal components, i.e. water vapor terms: Spatial linear trend, height dependent stratification, ground feature related stationary part and mixing turbulence. This model is given with primary purpose for comparison of water vapor from SAR APS, but it is also applicable for water vapor data from other independent technologies. Based on this, one complete approach for differentiation of four water vapor components was proposed. In the approach, mixing between spatial linear trend and stratification is divided by a joint least squares estimation, and then remained mixture of stationary part and turbulence is suggested to differentiate with temporally periodic averaging or spatially spectral filtering. With acquired MM5 data, spatial and temporal correlation law of the estimated water vapor turbulence are studied, based on the approach given above.

3.1 Introduction

In previous studies, two major terms -stratification and mixing turbulence-were carefully considered and modeled in atmospheric signal in SAR Interferometry (Hanssen 2001, Li Z.H. 2006, Onn, 2006; Cavalié, 2007; Doin 2009). The systematic error of spatial linear trend was less covered though its influence was mentioned by Hanssen (Hanssen 2001). While at the same time, after the modeling of spatial linear trend and stratification, turbulence is not the only residual signal in the remained water vapor and suggested to include ground feature related stationary part (Perissin 2010). In our assumed component model of water vapor, as represented in equation 3.1, spatial linear trend, stratification term, stationary term and mixing turbulence term are superimposed and mutual influential in water vapor maps. The reasons for

above consideration of spatial water vapor lie in following aspects. Firstly, the spatial linear trend is introduced by inaccuracy of SAR satellite orbit (Hanssen 2001). Secondly, temporally stationary term caused by ground feature such as water body, centralized vegetation would inevitably co-exist in InSAR atmospheric effect (Perissin 2010). Thirdly, when above compositions in water vapor mixed together, the discrimination of each water vapor effect confronts difficulty and the endeavor of correction of atmospheric effect turned hopeless. All in all, in more general and widespread cases, InSAR atmospheric effect not only contains the turbulence and stratification, but also mixes with other physical originals, e.g. the spatial linear trend and stationary terms.

Two target goals are set up in this chapter. 1) To propose a reasonable strategy to decompose the different components of water vapour. For this goal, two sub objectives can be then divided. The first one is to distinguish between spatial linear trend and stratification. And the second one is to distinguish between stationary term and mixing turbulence. 2) As turbulence terms are separated from above strategic approach, to study the statistical characteristics of its variation in space and time.

So in this chapter, we proposed methodology to extract each composition of the atmospheric water vapor signal. 1) In the proposed methodology, spatial linear trend and linear stratification has been synchronously modeled with joint least squares fitting. 2) And then stationary term and turbulence was distinguished with introduced two approaches, temporal periodic averaging with large amount of hourly MM5 IWV maps, or spatial spectral filter at spatial frequency threshold for each independent map. 3) Spatial and temporal variation in different scales of extracted mixing turbulence was studied by obtaining of its spatial temporal correlation image.

The founding in this chapter firstly provides evidence that spatial linear trend and ground feature related stationary term are superimposed and mutual influential with stratification & turbulence terms in water vapour. It improves the theoretical understanding of water vapor signal in atmosphere, being potentially significant for

improving of water vapor modeling. This improvement of water vapor modeling would then generate engineering significance for correction of InSAR atmospheric noises in ground geophysical applications.

3.2 Component model of water vapor

Though the concept of mixing turbulence and stratification in atmosphere has been proposed in theory and studied with regional cases in last decades, a complete view and their relationship of all related factors in radar interferometry is still not available. The primary reason is that purposes of the previous concept are to remove dominated atmospheric noise in SAR interferograms. While for study of water vapor obtained from Radar Interferometric Meteorology, spatial linear trends and ground feature related terms can be mixed with above terms and difficult to distinguish. For a solid study understanding of the water vapor from radar, we proposed a component model of water vapor to improve the conceptual understanding and practical differentiating of water vapor from Interferometry.

Continuing to the theory of atmospheric water vapor in SAR Interferometry reviewed in section 2.2, ignoring the ionospheric signal and the hydrostatic atmospheric effect, expression of absolute integrated vertical water vapor in single SAR data can be written as a function of space coordinates x and y (in range and azimuth directions) as follows mathematic model (Perissin 2010):

$$
\begin{aligned}
\alpha_i(x,y) &= P_i(x,y) + \varepsilon_i(x,y) + k_i \cdot h(x,y) + w_i z(x,y) \\
&= \alpha_i + b_i x + c_i y + \varepsilon_i(x,y) + k_i \cdot h(x,y) + w_i z(x,y)
\end{aligned}
\tag{3.1}
$$

In equation 3.1, $\alpha_i(x,y)$ is the atmospheric water vapor in temporal epoch i at spatial point (x,y) in radar coordinates. $P_i(x,y)$ means spatial linear trend modeled as a 1st order 2D plane, expressed as $\alpha_i + b_i x + c_i y$, which is bilinear function of latitude and longitude (or north and east after projection, or range and azimuth in image). $\varepsilon_i(x,y)$ is the spatially correlated perturbation term, in which most of signal

41

are from the atmospheric turbulent processes. $k_i \cdot h(x,y)$ is height dependent stratified term, in which k is height dependent stratification ratio or slope. The last part $w_i z(x,y)$ stands for the ground feature dependent term, e.g. the land cover, water body etc. Here, w means the weight of influence by ground feature. The above model of water vapor components is originated from SAR, but also applicable for other spatial water vapor data.

As far as atmospheric water vapor in SAR interferograms or SAR APS, the observed signal owns the spatially and temporally differential characteristics. With a double difference from above equation 3.1, then we can get the differential water vapor model for only SAR APS water vapor as equation 3.2. Compared to absolute values, the constant term and nominal term of all components are all cancelled out in observed differential signal in equation 3.2.

$$
\begin{aligned}
\Delta\alpha_{iM}(x,y) &= [\alpha_i(x,y) - \alpha_i(x_0,y_0)] - [\alpha_M(x,y) - \alpha_M(x_0,y_0)] \\
&= b_{iM} \cdot \Delta x + c_{iM} \cdot \Delta y + \varepsilon_{iM}(\Delta x, \Delta y) \\
&\quad + \delta k_{iM} \cdot h(\Delta x, \Delta y) + \delta w_{iM} z(\Delta x, \Delta y)
\end{aligned}
\tag{3.2}
$$

Model given by eq. 3.2 is differential form of that in eq. 3.1. While, the model given in equation 3.1 is regarded as water vapor component model in this chapter, which would be taken as a basis of data analysis in this thesis. The physical interpretation of each component of the given model is stated as following:

1) Spatial linear trend

Spatial linear trend of water vapor from Radar could be possibly caused by following one or more reasons: a) a spatial trend as a systematic error inevitably introduced due to inaccuracy of satellite orbit for current platforms, such as ENVISAT, etc. (Hanssen 2001) b) Water vapor variation with spatial scale larger than the water vapor coverage concerned by RIM c) Ionospheric delay horizontal linear trend if more than 50 km. 4) removal of spatial linear trend enables water vapor characteristic of statistical stationarity, under which frequency processing and variogram calculation meet statistical preconditions.

2) Mixing turbulence

Turbulent Mixing results from atmospheric turbulent processes. It causes three dimensional heterogeneity of the refractivity in both horizontal and vertical direction during both SAR acquisitions, affecting flat terrain as well as mountainous terrain. Turbulent mixing is a result of different tropospheric processes such as solar heating of the earth's surface which can cause convection, differences in wind direction or velocity at different layers, frictional drag and large scale weather systems (Hansen 2001). Turbulent Mixing results from atmospheric turbulent processes and causes both horizontal and vertical heterogeneity in the refractivity.

3) Stratification

Stratification is caused by vertical refractivity profiles in two epochs and highly correlated with topography. This signal affects only mountainous terrain area if no turbulent mixing occurring. Such effect is called vertical stratification (Hanssen, 2001). Atmospheric stratification only considers vertical variation of the refractivity along height. For hilly or mountainous terrain, refractivity difference of the vertical profile during both acquisitions will affect the phase difference between two arbitrary resolution cells with different topographic height, and then cause an erroneous interpretation in the phase measurements for geographical parameters inversion.

4) Ground feature related water vapour

It is believed that land use/land cover changes induced by anthropologic activities have resulted in the change in land surface albedo, vegetation cover fraction, and greenhouse gases emission. Simulated models, satellite and in-situ observations have evidenced that these land cover changes affect the interaction of atmospheric, land surface process and hydrological process, in global scale, continental scale, and regional scale (Song 2010). Through the conversion of forests and grasslands to croplands and pastures, humans have affected the exchange of water between the atmosphere and land surface (Twine 2004).

43

Atmospheric precipitable water vapor mainly comes from two sources: land surface vapor -transpiration and water vapor transport from ocean, atmospheric water vapor content primarily depend on the land surface feature when the other weather conditions are the same (Song 2010). So the land surface characteristic will at some extent affect the precipitable water content and its spatial distribution. Thought the underlying mechanisms of water vapor variation (distribution) at local scale (with in $100*100$ Km^2) cannot be accurately modeled as being coupled by multiple related factors, It has been proved with various cased studies that water vapor can be remarkably affected by ground features (Song 2010). As investigated, usually, the water body area and forest land have most positive contributions on water vapor content as a whole (though a temporal lag exists).

We pay our attention neither on the mechanism of relationship between ground feature and water vapor signal, nor on the mathematical model of water vapor determined by ground feature. In this thesis, we determinately adopt the assumption of ground feature related signal in water vapor component model, which is paramount for later data comparison, as well as spatial pattern analysis on different scales in next chapters.

3.3 Data and Implementation

As represented in equation 3.1, spatial linear trend, stratification term, stationary term and mixing turbulence term are integrated in water vapor maps. Before analyzing spatial and temporal behavior of each basic signal, each component shall be clearly and independently separated in advance. The study in this section focuses on detection (or separation) of four basic signal compositions in water vapor which would be precondition of spectral analysis of each basic water vapor signal component.

Compared to limited data spatial coverage, unevenly distribution, sparse sampling restricted by radar coherence, temporally differential characteristics for

SAR APS water vapor signal. MM5 data was employed to validate the rational of water vapor component model because a good range of spatial scale (from 1km to 129 km) and wide temporal scale (1 hour to 25 hour) are provided as perspective window for perceiving water vapor signals.

MM5 Integrated Water Vapour (IWV) data in this research experiment are simulated products of Numerical Weather Predication (NWP) model, generated on two-dimensional surface centered at Roma, Italy, referring to Figure 3.1(a). More detail of MM5 model operations and input& output data could refer to official website of National Center for Atmospheric Research (NCAR)/Pennsylvania State University or related references (Grell 1995; Kistler 1999) and the review in section 2.1.4. More than 775 simulated IWV hourly maps on 32 dates are acquired during 2002 to 2008, as shown in Table 3.1 and Figure 3.1(b). MM5 Integrated water vapor (IWV) data have been kept in analysis chain only if IWV maps with 25 continuous hours are available. The day with less than 25 hourly IWV maps is discarded.

Table 3.1 Dates of all acquired MM5 IWV maps.

Dates of acquired MM5 IWV			
20051001	20070414	20050723	20060127
20081003	20080516	20070623	20050527
20031206	20021116	20070323	20071228
20040807	20041016	20040424	20060429
20040110	20051118	20060825	20080829
20071110	20080920	20081025	20050129
20031010	20021221	20050827	20080329
20070112	20030823	20040227	*Total 31*

Number of Hourly IWV maps in each day

(b)

45
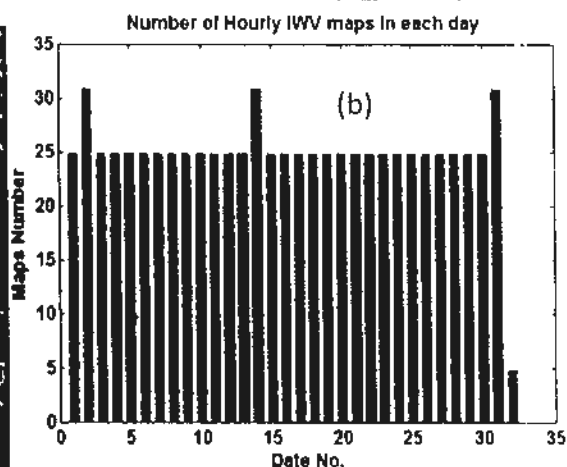
Figure 3.1 (a): Geo-location of simulated MM5 IWV at Rome in Italy shown on Google Earth, marked with red rectangular; (b): Number of maps of MM5 IWV hourly in each day.

The research experiment is carried out with MM5 Integrated Water Vapor (IWV) data, which are simulated products of Numerical Weather Predication (NWP) model, with spatial coverage of 129*129 km^2. These water vapor maps are highly suitable for spatial and temporal analysis of water vapor signal because they have sufficient detail of dynamic characteristics both in space and in time. With multiple-nested capability with increasing resolution in spatially horizontal domain, spatial scale of modeled MM5 IWV could vary from 27 km to as high as 1km, the water vapor maps employed in this experiment own spatial resolution of 1km. Besides the spatial scale of 1km, the temporal scale of MM5 water vapor is as high as 1h or half an hour.

But the limitation of MM5 water vapor we have to mention is that the prediction of water vapor field rely the numerical model, the initial observations or reanalysis data. So absolute synchronization of water vapor to given epoch and given point is difficult, and also the accuracy of predication depends on the beginning time and the span of running model (Perissin 2010).

DEM data is required for estimation of stratification signal of water vapour. In our experiment, DEM is firstly read from 3 seconds resolution SRTM DEM products, then resampled into 2D grid with spatial coverage (129*129km^2) and grid size (1km) as same as that of MM5 IWV.
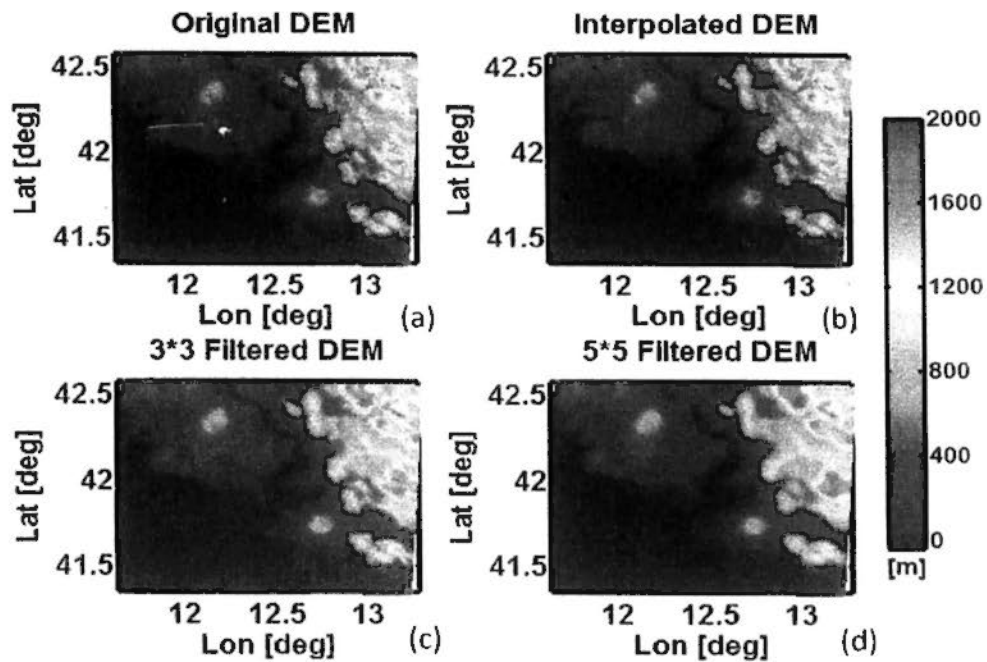
Figure 3.2 DEM in experimental area. (a) DEM grid (1km*1km) with blank area due to missing values from 3 seconds resolution SRTM DEM; (b) DEM grid, two dimensional triangle-based linearly interpolated on blank area. (c) DEM grid, by a median filtering with window size of 3*3 on interpolated DEM (d) Filtered DEM with window size of 5*5.

However, there are still missing values at regions in the 2D DEM grid as shown in Fig. 3.2 (a). For this reason, DEM grid is then interpolated with a triangle-based linear interpolation on blank area, as Fig. 3.2 (b). Besides this, the median filtering with window size of 3*3 and window size of 5*5 on interpolated DEM were operated to avoid possible artificial errors in modeling of height dependent stratification due to small sudden fluctuation of DEM.

From above Fig. 3.2, DEM of experimental area in Northeast is higher than that in the South west. A spatial pattern can be visibly perceived that height is gradually decreased from mountainous Northeast to oceanic Southwest.

3.4 Stratification and spatial linear trend

As stated at the beginning of this chapter, one reasonable way shall be fixed to separate each composition of water vapor according to their characteristics for the purpose of validate the water vapor component model. The terms in first group we

dealing with are re stratification and linear trend, because both terms are directly correlation with geography or elevation.

3.4.1 Linearity of stratification

In this sub section, the stratification effect in IWV is studied. The question to be answered is that the height dependent stratification is linear or non-linear. And how much modeled residuals there are if a simple linear assumption is adopted.

With acquired MM5 data described in previous section, height dependent stratifications of IWV in six random days are shown in figure 3.3. The adopted IWV are daily stacked data from multiple hourly maps to increase samples for analyzing stability. In each sub graphy of figure 3.3, more than 400, 000 samples are divided into different groups according to their heights. Each group is determined by evenly spaced and increased height with experiential step of 100m. Then the statistical means and standard deviations of grouped IWV are drawn with error bar to represent the trend and its uncertainty. With elevation range close to 2000m, the approximate inverse linear relationship between IWV and height are clearly observed in all cases.
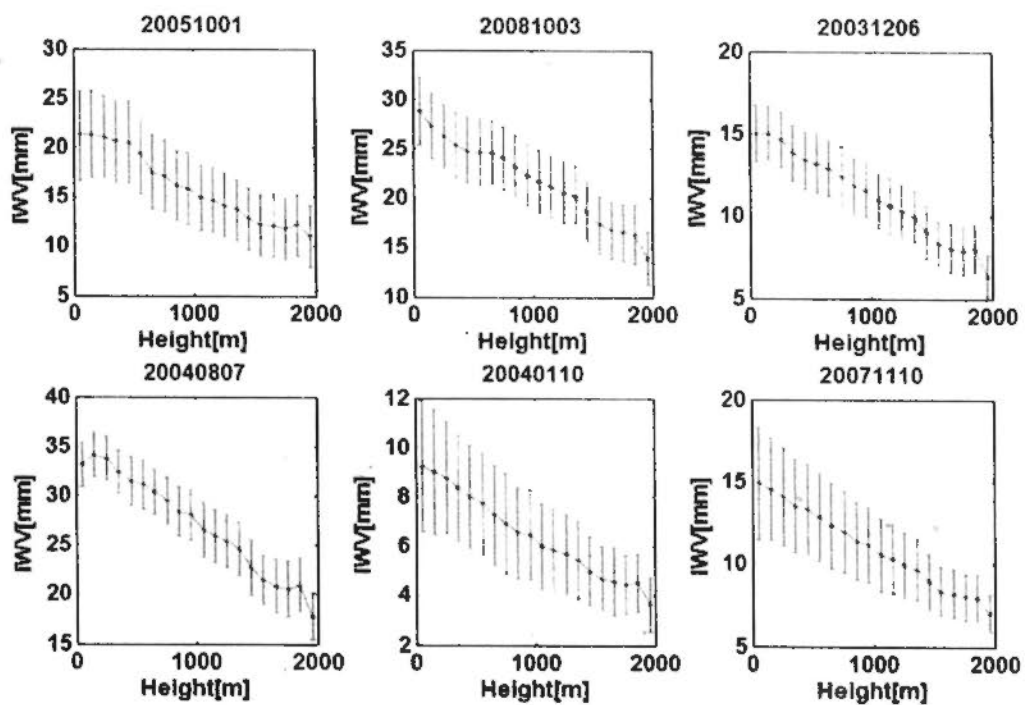
Figure 3.3 Height dependent stratification of MM5 IWV (in six random days). IWV are daily stacked from multiple hourly maps to ensure stability. Statistical mean

and standard deviation of grouped IWV are drawn with error bar. Each group is determined by evenly spaced and increased height. Increasing step of 100m for centered height in each group are chosen.

To mathematically judge the linearity, following three models are compared to test the linearity of stratification in this section. Linear model are simple but widely used as assumption of stratification effect. 3rd order polynomial function model are chosen for comparison to answer whether the high order nonlinear effect be influential or not. As claimed to be advantageous to model stratification at lower attitudes, advanced exponential model given by Onn was adopted in comparison to answer the questions given in this section.

$$\alpha(h) = a + bh \qquad (3.3)$$

$$\alpha(h) = a + bh + ch^2 + dh^3 \qquad (3.4)$$

$$\alpha(h) = I_0 + Ce^{-\beta h} + h\beta Ce^{-\beta h} \qquad (3.5)$$

The equation (3.3), (3.4) and (3.5) respectively stands for linear model, 3-order polynomial model and Onn's Exponential model for stratification of integrated water vapor (IWV). In all three equations, $\alpha(h)$ and h means IWV and local elevation. In equation (3.3) and (3.4), a, b, c and d are polynomial coefficients. In equation (3.5), I_0, C and β are model parameters (Onn, 2006).

With stacked daily IWV data, modeled IWV values versus their height on given six days are drawn in Fig. 3.4. The performances of above three models can be observed together in each sub graph. At moderate height, i.e., from 100m to 1600m, curve of linear model highly close to that of non linear model. While at lower height and extremely larger height, curve of nonlinear model would partially departure from linear model. Even nonlinear model performs instability in individual cases, i.e. 3rd order polynomial model and Onn exponential model departure from each other with remarkable contrary trends on 20081003.

The table 3.2 gives the Standard deviation of IWV residuals with above three models. The statistical numbers can prove the above judgment. Residual of Onn's

exponential model on 20081003 and 20071010 are slightly higher than that of simple linear model. With general perspective of statistical numbers of table 3.2, nonlinear model keeps a little higher performance than linear model, but the difference between them are not distinct.
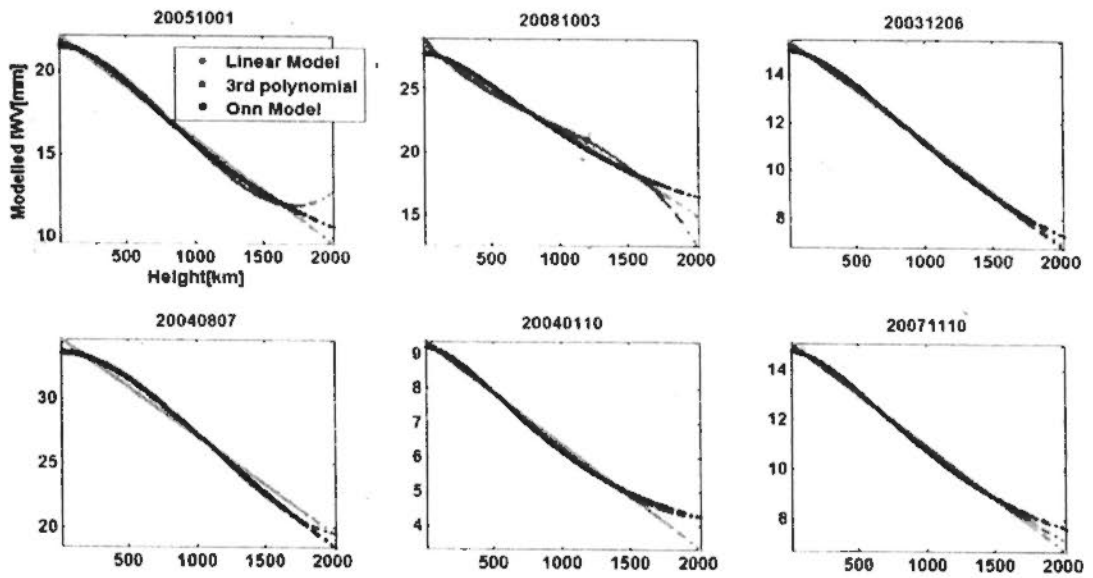
Figure 3.4 The modeled IWV values versus height given by stratification models. Curves with red, blue and black color represent the linear model, 3rd order polynomial function model and Onn's exponential model (Onn 2006).

Table 3.2 The STD of IWV residuals of modeled stratification.

Std of modeled IWV residuals	20051010	20081003	20031206	20040807	20040110	20071010
Linear model	4.070	3.292	1.702	2.501	2.188	2.791
3rd polynomial model	4.044	3.268	1.700	2.420	2.186	2.791
Exponential model (Onn)	4.046	3.343	1.703	2.420	2.185	2.795
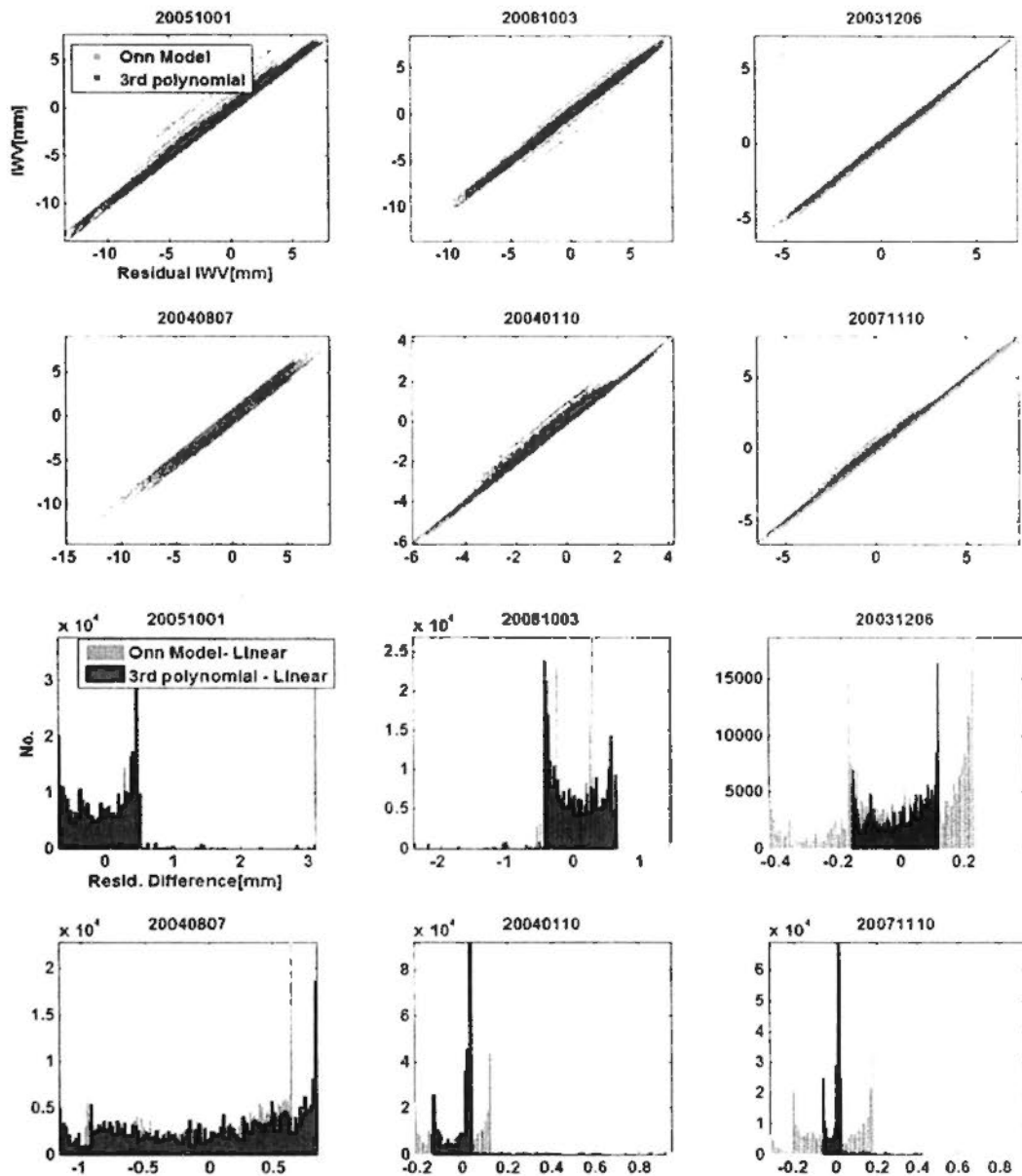
Figure 3.5 The IWV residuals of modeled stratification from total MM5 water vapor and histogram of difference of IWV residuals. For the first six sub graphs, IWV residuals of Onn's exponential model versus that of linear model are given by scatter points in red color. IWV residuals of 3rd order polynomial model versus that of linear model are plotted in blue color. For the last six sub graphs, differences of modeled IWV residuals between Onn model and linear model are plot in red, and that between 3rd order polynomial model and linear model are plot in blue.

Besides the macro-view of performance difference for data collection, the micro -view of performance difference for individual samples are detected. The information of performance difference for above models was included in figure 3.5. IWV residuals of modeled stratification and histogram of difference of such IWV residuals,

for nonlinear compared to linear model, are plotted in figure 3.5. Firstly, the IWV residual coincide well among three with positive linear relationship. Secondly, except individual samples in one case (20051001), the difference of IWV residuals of modeled stratification between above three models are small than 1.2mm. While difference among three models less than 0.6 mm is applicable for majority of individual samples.

Therefore, our suggestion on stratification is as follows. For map based water vapor comparison and spatial statistical study of water vapor field, the linear model for stratification can be competent with uncertainly of 0.6 ~1mm. For point based water vapor comparison or water vapor induced delay, especially at area with highly variable elevation, nonlinear model are preferential with better performance.

3.4.2 Spatial linear trend of IWV and DEM

As discussed in the model in section 3.2, besides topography correlated stratification term, 2D spatial linear trend would also coexist in integrated water vapor and affect partition of other terms, e.g. ground feature related stationary term and mixing turbulence. As discussed in section 3.4, the reasons of carefulness on spatial linear trend lies in two points: 1) the spatial trend in SAR products are systematic error due to satellite small instability; 2) the spatial trend in non SAR products are due to the distribution in scale larger than target area, which is not the study focus from statistical view.

This mentioned spatial linear trend was clearly validated with our data, as shown in Fig. 3.6. The figure 3.6 shows observed typical spatial linear trend in acquired MM5 IWV data. The 1st column plots three original IWV maps in three different days (20051010, 20041016 and 20060825). The corresponding spatial linear trends are remarkable visible and modeled in 2nd column. Such spatial trend can be in random directions, depending on water vapor distribution at larger scale. The 3rd column plots daily averaged IWV maps on these three days. From the averaged IWV maps with more than 24 hours, spatial linear trend is decreased but

still can be observed. The modeled spatial linear trends from such daily averaged IWV maps are drawn in last column in Fig 3.6
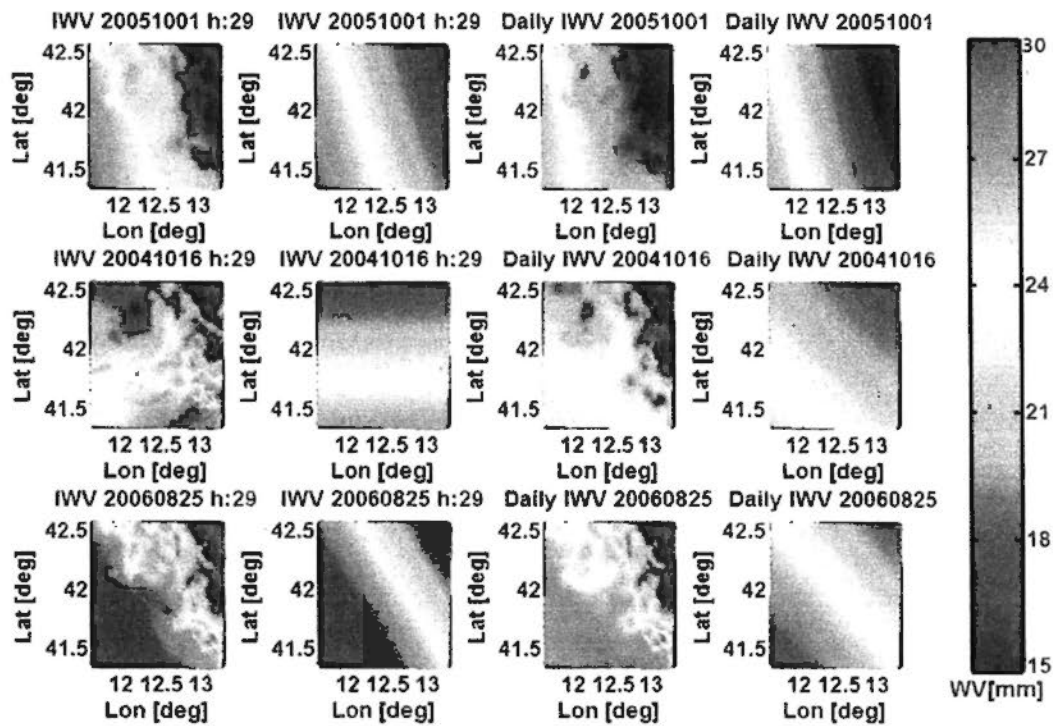
Figure 3.6 Observed typical spatial linear trend in MM5 IWV. The 1st column plots three IWV maps in three different days (20051010, 20041016 and 20060825). The corresponding modeled spatial linear trends are drawn in 2nd column. The 3rd column plots daily averaged IWV maps on these three days. Similarly, spatial linear trends modeled from such daily averaged IWV maps are drawn in last column.

While, making the problems more complicated, spatial linear trend not only exits in IWV maps, the trend can also be observed in elevation in target area, e.g., DEM in our experimental area. DEM data in experimental area and spatial distribution of signal intensity of elevation in different angles were drawn in Fig. 3.7. This signal intensity was obtained by Radon transformation and projected to rotated directions. Radon transform is a tool to project intensities of image into a transect line at given angles. A mapping of an image from two dimensions to one dimension through Radon transform is significant to investigate spatial anisotropy or patterns of intensity variations (Bracewell 1995; Ding 2008). In our case, from the Fig. 3.7, viewing at the center of DEM map and taking eastward direction as reference, most strong signals of elevation are located at +40~60 km at angles between -20~+20

degrees. On the contrary, nearly no signals of elevation are located at -40~-90 km at angles between +40~+90 degrees. These numbers are direct evidence to prove the correlation between height dependent stratification and spatial linear trend.
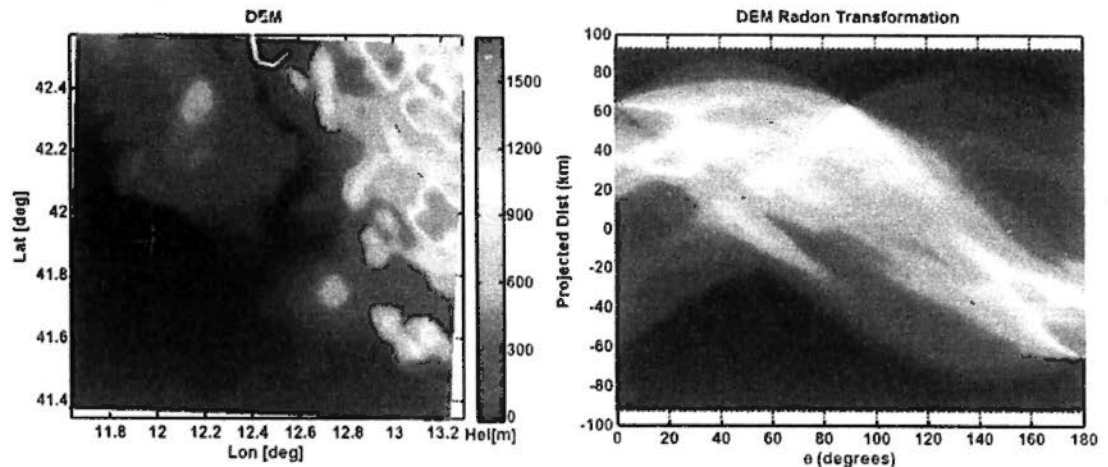
Figure 3.7 Dem in experimental area and spatial distribution of signal intensity of height in different angles by Radon transformation. The origin of radon transformation is geometric center of DEM map, directions in degrees are anticlockwise rotated and relative to eastward direction (0 degree).

The case that target elevation has strong spatial linear trend can be applicable in most global land area with coverage larger than 100* 100km. Under such cases, the separation of stratification and spatial linear trend shall be carefully considered to avoid misinterpretation due to partially correlation.

3.4.3 Joint retrieval with least squares fitting

In last section, it has been point out that the separation of stratification and spatial linear trend shall be carefully considered if that elevation in experimental area has certain extent of spatial trend.

The truth is that the spatial linear trends are less concerned. If concerned, it is commonly modeled with a simple 2 dimensional linear model and then removed from water vapor maps. In the section, we highly suggest a joint least squares fitting strategy to synchronously retrieve spatial linear coefficients and stratified coefficients. Synchronous retrieval of all above parameters can effectively avoid misinterpretation of individual terms due to partially correlation between both.

The principle of parameter retrieval by least squares fitting is as following. From equation 3.1, water vapor signal can be rewrite into equation 3.6. Since other terms, e.g. turbulence and stationary signals are neither correlated to latitude or longitude, are nor correlated to elevation. To focus on the target parameters we concerned, the water vapor signals can be regarded as integration of only spatial linear trend, height dependent stratification and other random terms, as illustrated in equation 3.6.

$$
\begin{aligned}
\alpha_i(x, y) &= P_i(x, y) + k_i \cdot h(x, y) + \varepsilon_i \\
&= a_i + b_ix + c_iy + k_i \cdot h_{(x,y)} + \varepsilon_i
\end{aligned}
$$

(3.6)

For an observed water vapor map at given epoch, all spatial pixels observed above equation. The function model in matrix form can then be constructed as equation 3.7.

$$
\underset{N\times 1}{\Phi} = \underset{N\times 4}{A} \cdot \underset{4\times 1}{X} + \underset{N\times 1}{\varepsilon}
$$

$$
A = \begin{bmatrix} 1 & x_1 & y_1 & h_1 \\ 1 & x_2 & y_2 & h_2 \\ & \downarrow & & \\ 1 & x_N & y_N & h_N \end{bmatrix}
$$

(3.7)

$$
X = \begin{bmatrix} a & b & c & k \end{bmatrix}^T
$$

Based on the principle of minimum of error squares in least squares fitting, to meet $\varepsilon^T \varepsilon = min$, the target parameters can be uniquely determined as equation 3.8 if no special weights for observations are specified.

$$
X = (A^T \cdot A)^{-1} \cdot (A^T \cdot \Phi_0)
$$

(3.8)

The parameters model can be iteratively resolved and above four coefficients, a, b, c and k can be retrieved. With the coefficients, the spatial linear trend and stratification term can then be reconstructed. Figure 3.8 shows separated spatial linear trend and stratification term from MM5 IWV by join least squares fitting. The illustration example is given at UTC hour 23 on 20071010. Remained signal (Fig.

3.8d) is the original water vapor (Fig. 3.8a) after removal of modeled spatial linear trend (Fig. 3.8b) and modeled stratification (Fig. 3.8c).

To better demonstrate the necessity of least squares fitting, we compared the difference of results between joint lease square fitting strategy and sequential separation strategy. For the sequential separation way, two choices are both adopted for better comparison. Choice A: retrieval and removal of stratification is at first step, and retrieval of spatial linear trend is at second step. Choice B: retrieval and removal of spatial linear trend is at first step, and retrieval of stratification is at second step. Four parameters a, b, c and k are retrieved for each hourly IWV map. 775 IWV maps in 31 days provided sufficient statistical samples of retrieved parameters, improving statistical significance of comparison. In figure 3.9 and 3.10, the four coefficients retrieved between least squares fitting, choice A and choice B of sequential separation are plotted with scatter points for comparison.
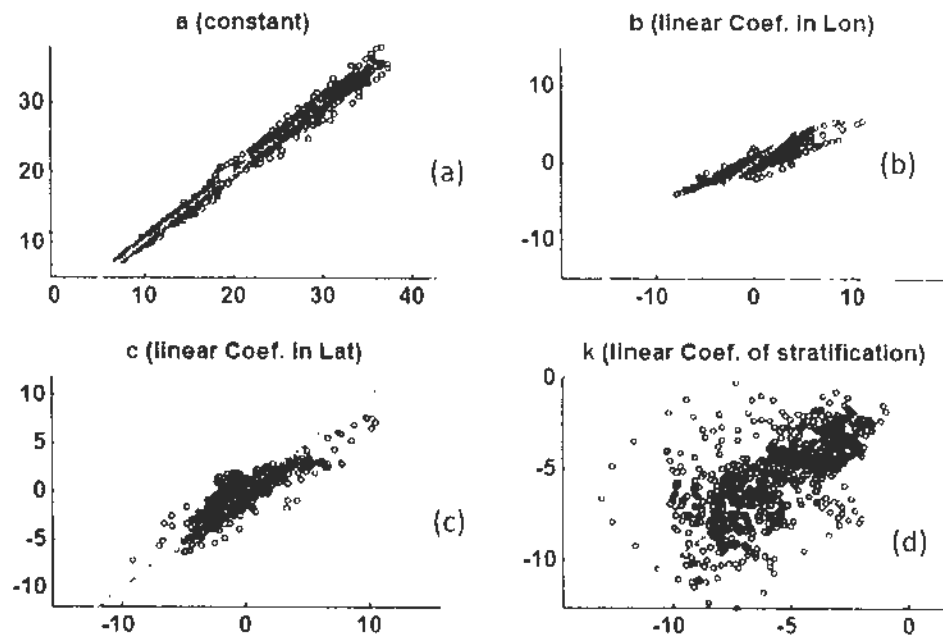
Figure 3.9 Retrieved parameters in sequential separation way versus that from joint least squares fitting. In this sequential way, retrieval and removal of stratification is at first step, and retrieval of spatial linear trend is at second step. The lines with slope of +1 are drawn in red for reference.

The results of the choice A for sequential separation way are shown in Fig.3.9. In this way, modeling of stratification has priority than modeling of spatial linear

trend. Then the spatial linear trend, varying with intensities and directions in different maps, would inevitably bias the retrieved stratification slopes, strongly or slightly, positively or negatively. Therefore, the retrieved stratification coefficients have increased random error, as validated in last sub graph of Fig. 3.9. Meanwhile, after the modeling of stratification with its maximum and then removal of biased stratification, the retrieved spatial trends are slightly decreased in magnitude, though keeping the sign (positive or negative). This can also be validated by 2nd and 3rd sub graphs in Fig. 3.9.
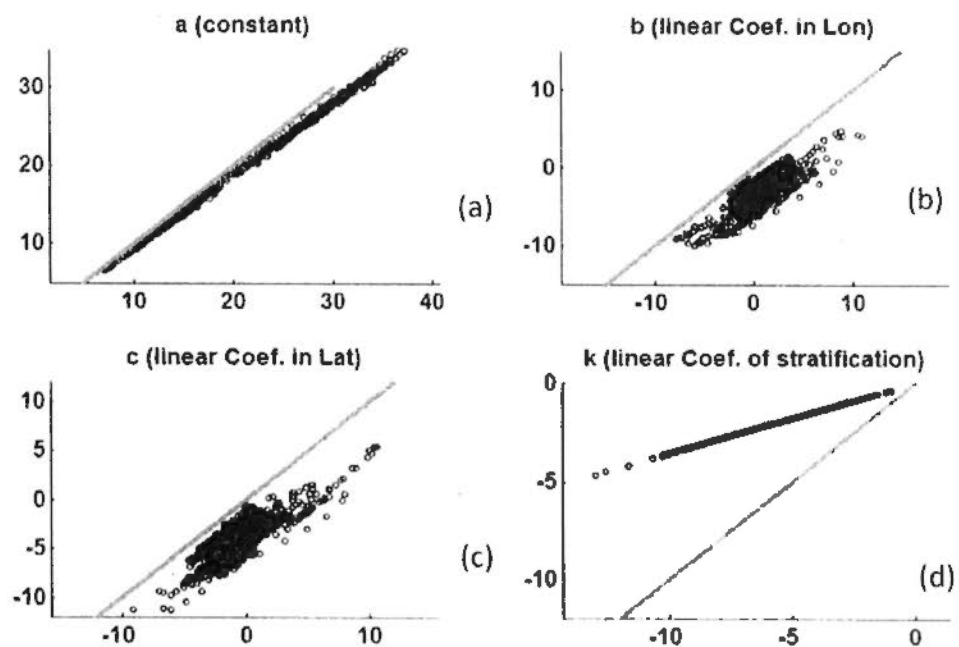
Figure 3.10 Retrieved parameters in sequential separation way versus that from joint least squares fitting. Retrieval and removal of spatial linear trend is at first step, and retrieval of stratification is at second step. The lines with slope of +1 are drawn in red for reference.

Inversely, Fig.3.10 presents the results of choice B for sequential separation way. In the choice B of sequential separation way, spatial linear trend is modeled with priority than stratification. Then a bias with constant sign but varying scaling from spatial pattern of DEM would be compulsively imposed on the retrieved spatial linear coefficients in latitude, longitude. Therefore, negatively overestimation of spatial linear coefficients and distinct underestimation of stratification coefficients can be validated in sub graphs in Fig. 3.10. Compared to least squares fitting.

estimated stratification slope in choice B of sequential way is quite special. The biased stratification effects due to spatial linear trend are kept straight in linear scaling relationship, thought underestimated.

In summary, based on above analysis in this section, we point out height dependent stratification can be correlated with spatial linear trend if the DEM has spatial pattern. In such cases, a strategy of synchronous retrieval for parameters in both terms by a least squares fitting is quite better than the strategy of sequential separation way.

As far as the case of our experimental area, the topography owns a spatial trend from northeast to southwest. So the founding and recommendation are also applicable and significant for other maps based water vapor data, e.g. MERIS and SAR APS.

3.5 Stationary term and turbulence

As proposed in the water vapor component model in section 3.2, the acquired water vapor is regarded as the superimposition of four signal compositions, i.e. four different water vapor terms: Spatial linear trend, height dependent stratification, ground feature related stationary term and mixing turbulence term. According to the discussions and suggestions given in last subsections, we carefully considered the influence of elevation dependent stratification and spatial linear trend and reasonably removed the two water vapor terms for each IWV map with least squares fittings strategy. Then remained water vapor signal after removal of stratification and spatial trend, according to water vapor component model, can be regarded as the combination of mixing turbulence and ground feature related stationary term.

The objective of this subsection is to distinguish between such stationary term and turbulence term. In the following context of this subsection, water vapor then means remained water vapor after removal of stratification and spatial trend as illustrated in section 3.4. Before any implementation of differentiating between two

58

terms, the differences of statistical characteristics between stationary term and turbulence term are claimed as followings based on the theory of the model:

1) SPATIALLY: The Stationary term would be generally correlated to local ground feature, e.g., small Lakes, linear watersheds, pieces of forests or shaded area of mountains, so the spatial scale of this signal is coincident with that of ground feature. Experientially speaking, the spatial scale of such kind of stationary terms is equal to or less than tens of kilometers. But turbulent term is randomly distributed and spatially independent. In most cases, the spatial scale is larger than that of stationary term, usually from tens of kilometers to thousands of kilometers.

2) TEMPORALLY: Generally, since above mentioned natural ground features always keeps high stability in the period from months to several years. Therefore the factorial signal of stationary term is assumed to be temporally unchanged, though the weights of signal for each IWV map is dependent of overall intensity of vapor. Inversely, as discussed in the model, the driving force of mixing turbulence is complicated with multiple factors including: solar heating, temperature, pressure, wind, frictional force, monsoon and etc. Therefore, mixing turbulent term varies quickly in time domain, usually keeping higher correlation within less than 3 hours and turning to uncorrelated in 24 hours.

The above statistical characteristics between stationary term and turbulence term can be adopted as the principle of differentiating between both terms. In this section, the designed approaches to implement the goal are in following two ways. 1) Temporal technique: periodic averaging; 2) Spatial technique: Spectral filtering. The two techniques in detail will be described in following contexts. Lastly, spatial and temporal decorrelation law for turbulence signal shall be studied after successful differentiating of above two terms.

3.5.1 Temporally periodic averaging

According to the above discussions, the remained water vapor signal after removal of stratification and spatial trend, based on water vapor component model,

can be regarded as the combination of mixing turbulence and ground feature related stationary term. Figure 3.11 presents maps of remained water vapor after modeling and removal of spatial linear trend and stratification in continuous 12 hours on 20050723. As shown in the figure, generally turbulence signal behaves in larger spatial scale and shorter temporal correlation time than the stationary term, though the intensity of stationary term varies in different maps.
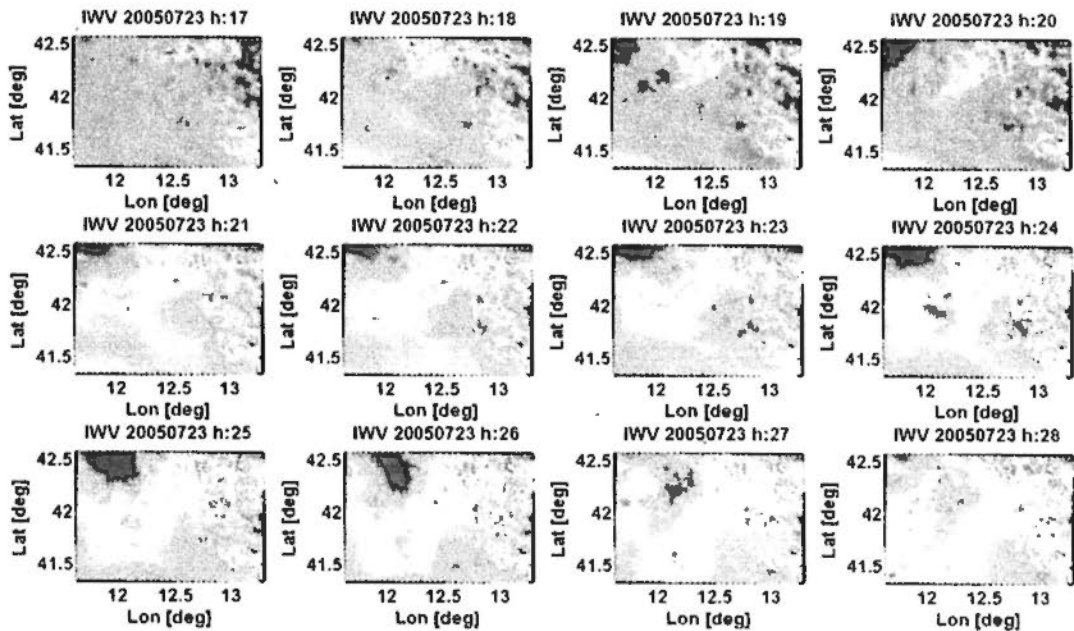
Figure 3.11 Maps of remained IWV after modeling and removal of spatial linear trend and stratification in continuous 12 hours on 20050723.

In equation 3.1, stationary term is expressed in $w_i z(x, y)$. w_i is linear coefficient (or weight) of ground feature z at ground location (x, y). But this linear coefficient is difficult to directly estimated, because that up to now no determinate relationship between the stationary term and ground feature has been reliably built. In addition, how to transform different classification of land cover in to comparable scalar of ground feature is still unresolved.

Restrained by above two reasons, we adopted a statistical approach instead of deterministic approach in this subsection. The way we adopt is to use periodic averaging to restrain temporally varied turbulence signal and treat global average of remained signal in extremely long time as factorial signal of stationary term. This

factorial signal of stationary term is used as independent variable to linearly fit the scaling factor (not weight) of stationary term in each IWV map. Then individual stationary term in each water vapor map could be statistically recovered. The whole principle can be illustrated as following equations.

$$\alpha_i^{-}(x, y) = w_i z(x, y) + \varepsilon_i(x, y) \tag{3.9}$$

$$\alpha_i^{-}(x, y) = \gamma_i \cdot [w_0 z(x, y)]$$
$$\gamma_i = \frac{w_i}{w_0} \tag{3.10}$$

In eq. (3.9), $\alpha_i^{-}(x, y)$ is remained water vapor signal, w_i is weight of stationary term, ε_i is turbulence term. Eq. (3.10) is rewritten from eq. (3.9), in which $w_0 z(x, y)$ means factorial signal of stationary term, and γ_i means the scaling factor (not the weight w_i). The Eq. (3.10) is adopted in periodic average as estimation of stationary term estimation instead of Eq. (3.9). The practical operation is implemented by following steps:

1) Daily average of water vapor maps

At first step, we calculate daily average of remained water vapor map within 24 hourly. The whole region of experimental area, including both Land and water area is involved in calculation. Maps of daily averaged remained IWV signal after removal of spatial linear trend and stratification on eight random days are presented in the Figure 3.12. From the eight daily averaged maps, turbulence signal have been highly constrained after 24 hours averaging, but still detectable in specific cases, e.g. 20070414, 20041016.
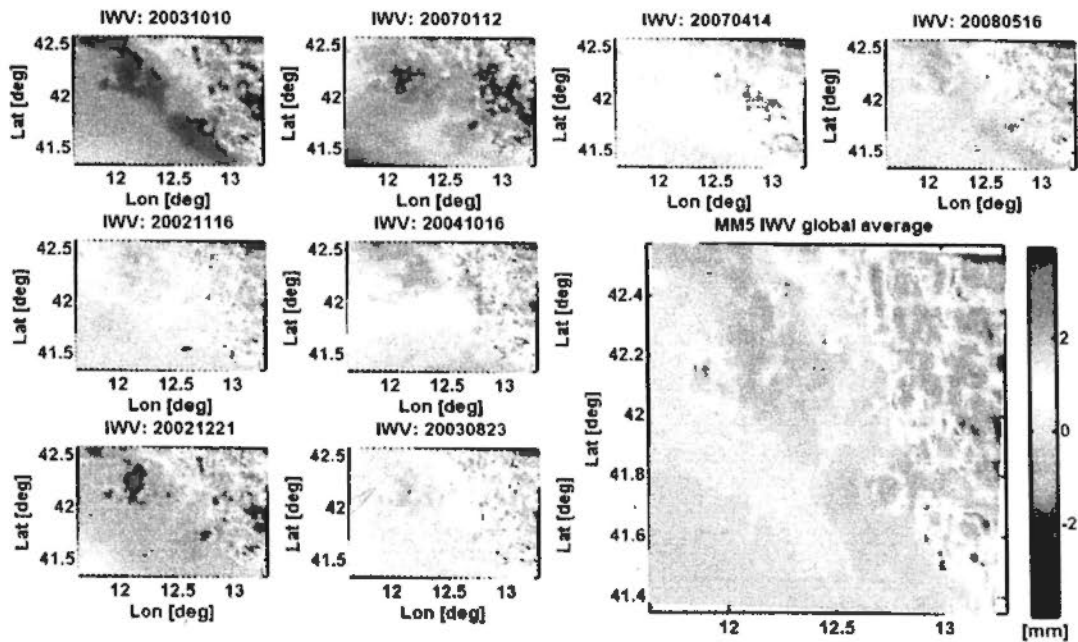
Figure 3.12 Maps of daily averaged remained IWV signal after removal of spatial linear trend and stratification on 8 random days. The globally averaged map of such remained IWV signal was zoomed in and drawn at last sub graph.

2) Global averaging of daily averaged water vapor maps

To further restrain the turbulence signal in daily maps, global averaging on daily averaged water vapor maps was operated. In Fig.3.12, the globally averaged map of such IWV signal was drawn at last sub graph which has been was zoomed in. Since the global averaging is taken across several years, this globally averaged map then can be regarded as stationary term.

3) Retrieving of scaling factor of each stationary term

The stationary term obtained in global view is only factorial signal of stationary term, as $w_0 z(x, y)$ illustrated in equation 3.10. This factorial signal of stationary term is then employed as independent variable to linearly fit the scaling factor of stationary signal in each IWV map.
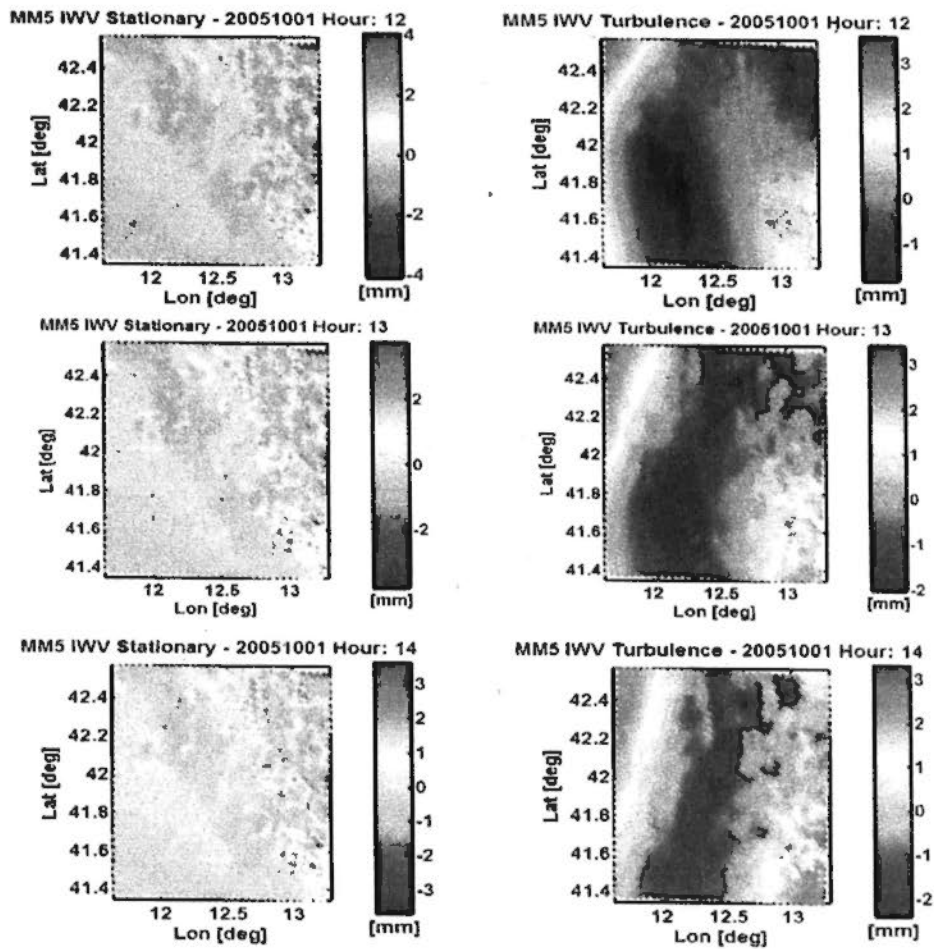
Figure 3.13 Separated ground feature related stationary term and turbulence signal by approach of temporally periodic averaging. Maps in three consecutive hours on 20051001 are shown in the figure.

4) Recovering of stationary term and turbulence

Continuing to last step, individual stationary term in each IWV map can be modeled with factorial signal of stationary term and retrieved individual scaling factor. The turbulence term is then subtracted from remained water vapor signal by stationary term. Figure 3.13 presents one example of separated ground feature related stationary term and turbulence signal with above temporally periodic averaging approach. Maps are drawn in three consecutive hours on 20051001. Figure 3.14 present another case of such separation by this approach. Maps in three different days are shown in this figure.
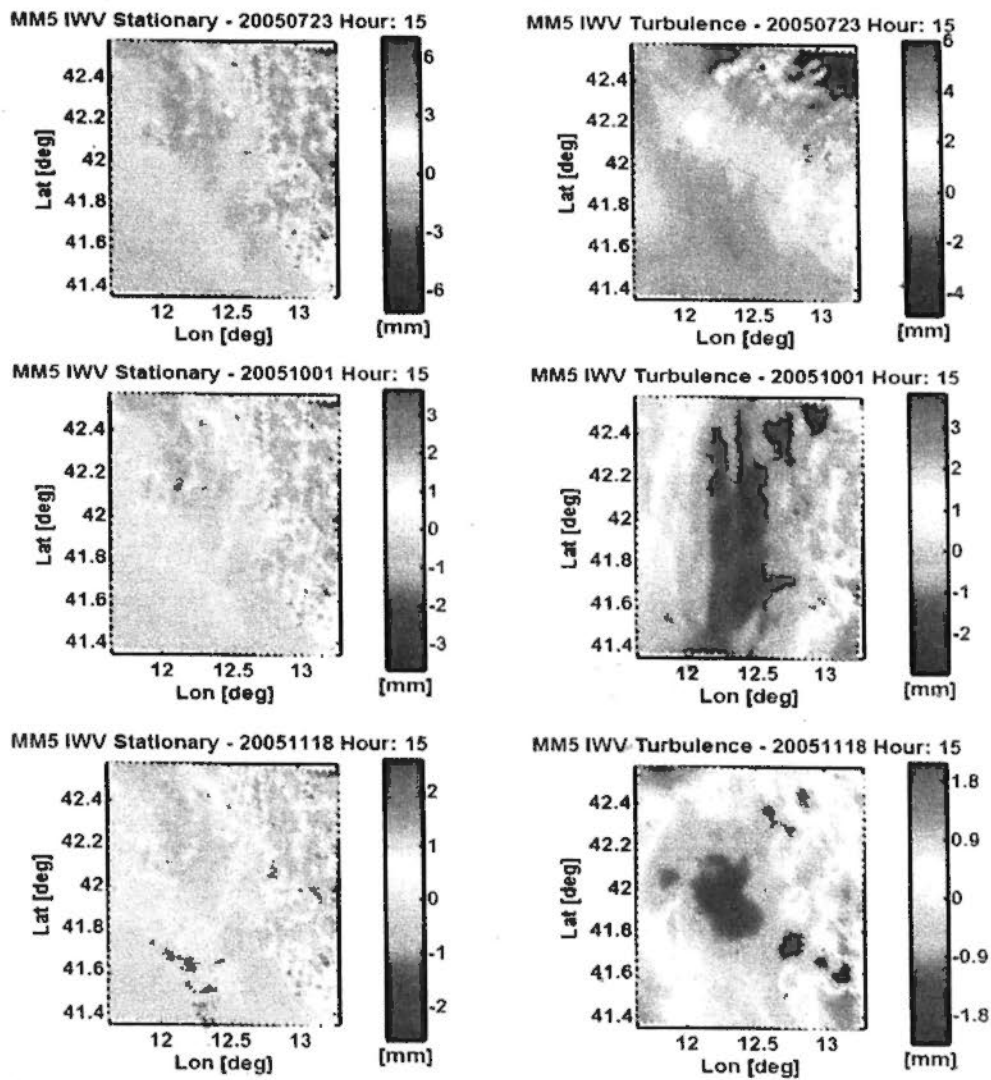
Figure 3.14 Separated ground feature related stationary term and turbulence signal by approach of temporally periodic averaging. Maps in three different days (20050723, 20051001 and 20051118) are shown in the figure.

Comparing the result examples in two figures, some assumption in spatial domain can be well proved by such implementations in temporal domain. The first is that the stationary signals are in quite small scale, with the pixel resolution of 1km, stationary signals in maps can be perceived with scale of 2~10 km. The second is that turbulence terms behave sin large scale, e.g. 30~100 km. In given cases, the temporal variation of turbulence across three hourly still keep high correlation, while turbulence signals across days are fully unrelated.

3.5.2 Spatially Spectral Filtering

In this section, we provide another approach to distinguish between stationary term and turbulence term from remained water vapor. As discussed at the beginning of section 3.5, stationary term and turbulence term behaves in different spatial scales. Then the dividing of both terms is feasible if we transform the spatial signal into frequency domain and separate the two terms by low/high pass spectral filtering with experiential spatial frequency threshold.
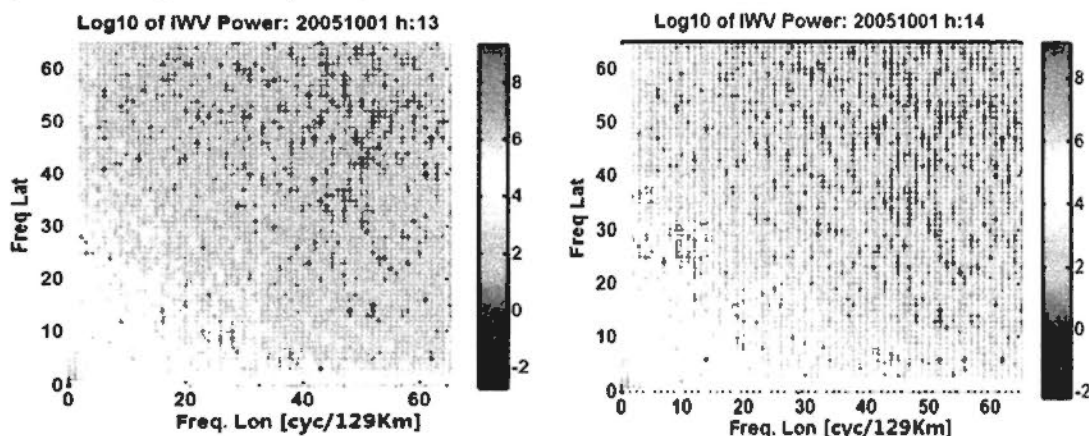
Figure 3.15 Spatial power spectrum of remained IWV signal after removal of spatial trend and stratification, two hourly cases on 20051010 are shown. X and Y axis represents signal spatial frequency with unit of cycle/129km. The signal power was saturated with range from 10^{-2} to 10^8.

Fig. 3.15 presents the signal power in different spatial scales in two hours on 20051010. The stationary terms and turbulence terms are both included and contributive in the intensity maps. From experiential observing of multiple spatial power spectrum density maps, the signal power intensity beyond 10^6 dominates in spatial scale larger than 8 cycles/129Km, i.e. 16Km; while the signal power intensity beyond 10^5 dominates in spatial scale larger than 16/129Km, i.e. 8Km. These maps provide us experiences of choosing appropriate bandwidth of spectral filter in frequency domain to distinguish between two target terms. Finally, half bandwidth of spectral filter with 8 in frequency domain (spatial scale of 16 Km) is chosen to balance the signals of turbulence terms and stationary terms.
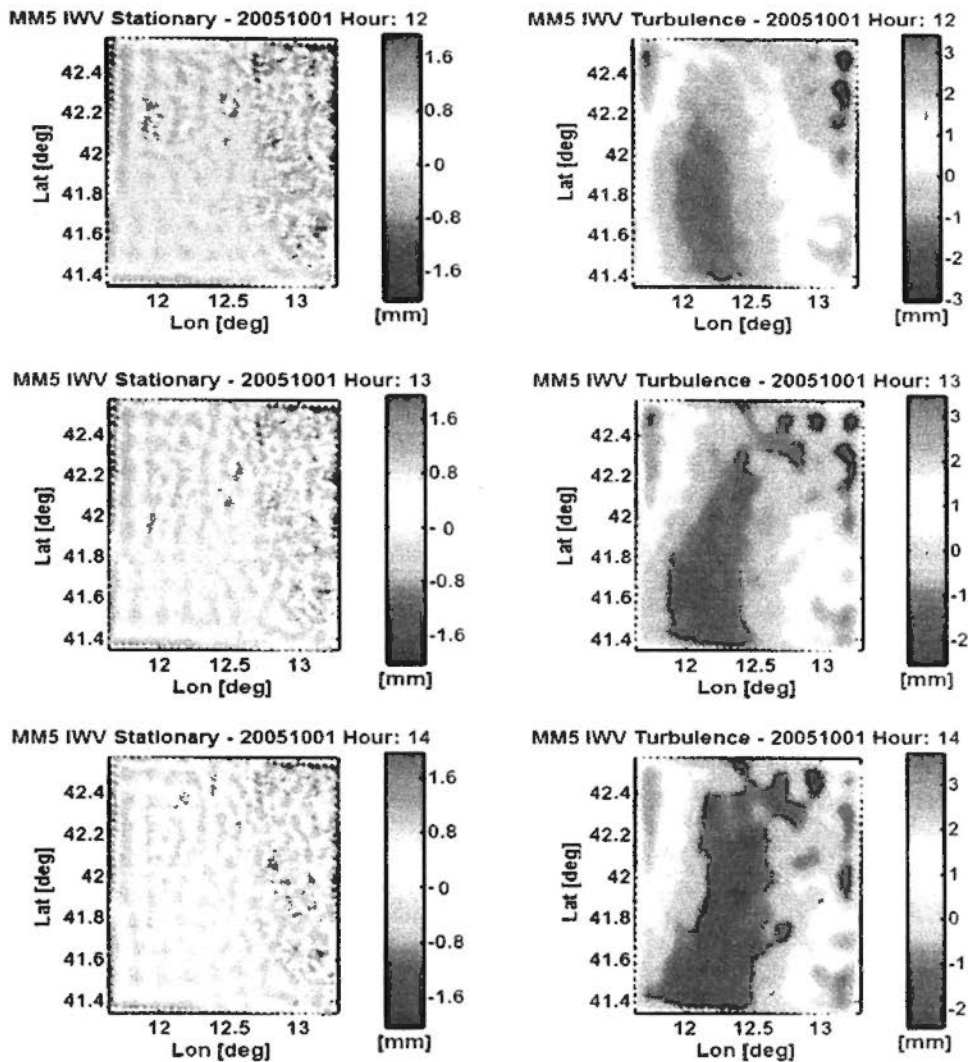
Figure 3.16 Separated ground feature related stationary term and turbulence signal by approach of spatially spectral filtering. Maps in three consecutive hours on 20051001 are shown in this figure as Fig. 3.13.

The power spectrum of remained water vapor signal in frequency domain is divided into two parts, the spectrum in low frequency and that in high frequency. Corresponding low/high pass frequency filters were divided at frequency boundary of 16 Km. This experiential threshold was analyzed from power spectrum map, as discussed before. Then the stationary term signal was recovered from high frequency, while the mixing turbulence signal was recovered from low frequency part by inverse Fast Fourier Transformation. The figure 3.16 shows one example of separated results of stationary term and turbulence signal by approach of such spatial spectral filtering.

Comparing the result in Fig. 3.16 (temporal periodic averaging approach) and results in 3.13 (spatial spectrum filter), following points can be summarized. Firstly, the spatial distributions of turbulence term for common IWV map from two independent approaches are almost coherent. Secondly, the turbulence estimated from spatial spectral filter is slightly underestimated, while stationary terms behaves with some artificial error, compared to that from temporal periodic averaging. Thirdly, the boundary at IWV maps cannot be well handled by spatial spectral filtering; this is the intrinsic limitation of spatial spectrum transformation and signal recovery from frequency domain.

One important point should be seriously stressed is the problem of stationary term extracted from above two approaches. From figure 3.13, 3.14 and figure 3.16, you could observe that the dominated signal in assumed stationary term still has relationship with local topography, though being linearly modeled and removed. This signal is supposed as not the genuine stationary terms but the systematic artifacts caused by discrepancy of resolution of DEM data between that in MM5 models and that we resampled from SRTM. While, further removing such systematic artifacts is difficult but possible if DEM be firstly modeled from globally averaged MM5 IWV maps and then be employed in stratification estimation.

3.5.3 Spatial Temporal Correlation of Turbulence

With the approaches introduced in section 3.5.1 and 3.5.2, the turbulence term and ground feature correlated stationary term in water vapor can be distinguished. Therefore, the statistical characteristics of turbulence signal can be further studied, which is included as one of objectives of this chapter. To serve this purpose, the correlation analysis tool was used to study the spatial temporal characteristics of turbulence of water vapor. The correlation analysis can be referred to appendix B.3

As we previously mentioned, atmospheric turbulence is highly important in meteorological study. In addition, inhomogeneous delay induced by water vapor turbulence plays the critical limitation in SAR interferometry for ground detection

and deformation monitoring. While the turbulence signal in water vapor, compared to other terms covered in the component model, dominated the spatial and temporal variability and confronted the most difficulty of observing and modeling.

The objective limitation of this problem lies in following two reasons. 1) The turbulence term is always mixed with other terms and conventionally difficult to distinguish; therefore previous studies only deal with the law of total water vapor, but not turbulence. 2) The highly spatial and temporal data to model atmospheric water vapor are usually not available and reliable.

Based on analysis and discussion in previous two sections, the above mentioned problems were well resolved in our experiment. The implementations of our approach to serve target goal can be described as following steps: 1) Obtaining of power spectrum on spatial frequency with 2D FFT transformation for each hourly turbulence map. 2) Obtaining of 1D spatial spectrum projected from 2D spectrum in all rotated directions. 3) Forming different time series of spatial power spectrum with different lagged time, from more than 24 hourly maps. 4) Calculating of correlation of signal power of turbulence in different spatial scales and temporal lagged hours.
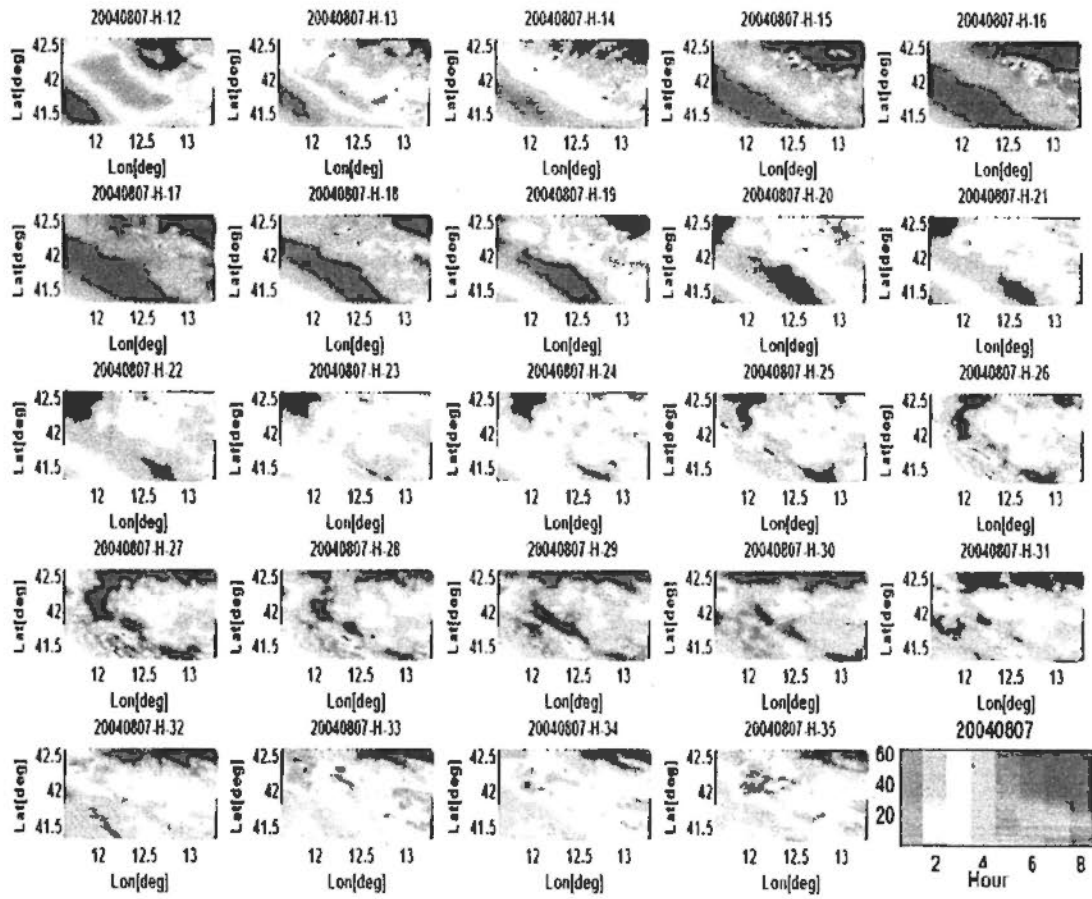
Figure 3.17 Extracted water vapor turbulence signals in 24 hours and calculated spatial temporal correlation coefficient image (last sub graph) on 20040807. The correlation coefficients were saturated in +/-1.

As shown in Fig. 3.17, extracted water vapor turbulence varied spatially within the range of 129*129 Km² and temporally in total 24 hours. The intensity of such variability in different spatial scales and temporal scales was illustrated in correlation coefficient image as shown in last sub graph of Fig. 3.17.
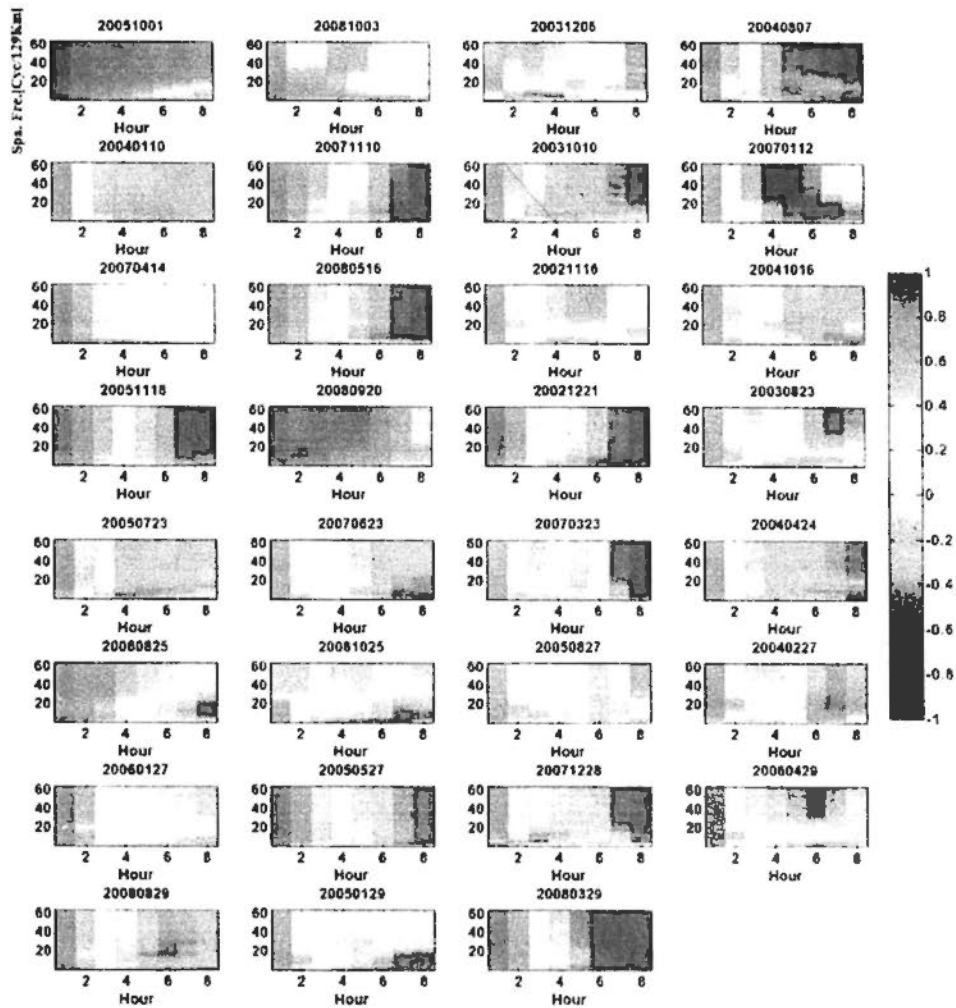
Figure 3.18 Spatial temporal correlation coefficient images on total 31 days. The meaning of X axis is lagged time in hours. The meaning of Y axis is spatial scale (or frequency) with unit of cycle/129Km. Number 1 to 64 means increased resolution from 130Km to 2 Km. The correlation coefficients were saturated in +/-1.

As illustrated in Fig. 3.18, spatial temporal correlation coefficient images on total 31 days were drawn to statistically represent spatial temporal decorrelation law of water vapor turbulence signal. In the figure, lagged time in hours is shown in X axis is, and the meaning of Y axis is spatial frequency (or scale) in the unit of cycle/129Km. The numbers from 1 to 65 marked in Y axis means the increased spatial resolution (from large scale to fine scale) from 130km to 2Km.

The result shows that 1~2 hour of turbulence in all scales, and even 3~4 hour of large scale turbulence are highly correlated. The result is significance that it provide evidence of linking of different water vapor sources with 1~3 hours of temporal gaps, for application of data synergy or mutual comparison and calibration.

3.6 Conclusion

To validate the water vapor component model proposed in this chapter, more than 775 maps of MM5 IWV data are collected to differentiate different compositions of water vapor. Three major parts being probed in this chapter are summarized as conclusion.

Firstly, spatial linear trend and stratification have been distinguished.

1) All IWV maps in mountainous area (2km in experimental area) exhibits height dependent stratification. With three models being tested, in map based water vapor study, instead of individual comparison or atmospheric delay analysis, there are neglectable difference between linear model and non linear model.

2) Spatial linear trend can be remarkable in most IWV maps. Such kind of spatial trends can be mitigated but partly left in averaged maps within 24 hours. This law can be simply observed from drawn figures and shall be carefully considered in spatial analysis of water vapor.

3) The differentiating between spatial linear trend and stratification is important, especially if the topography of experimental area has some extent of spatial trend. This precondition holds in our experimental area, which is observed from spatial distribution of signal intensity of height in different angles by Radon transformation of DEM data.

4) Joint parameter retrieval with least squares fitting is recommended if topography is correlated with spatial trend. After the comparison between this approach and the sequential separation ways, retrieved parameters in sequential separation ways shows instability (dispersion of parameter distribution) and bias (underestimation) than that obtained from least squares fitting shows.

Secondly, stationary term and mixing turbulence term have been distinguished.

1) Assumption on difference of characteristics between both terms was taken. Spatially, the stationary term was assumed correlated with scale no more than tens of kilometers. The spatial scale of turbulence can be regarded as from tens of kilometers

71

to thousands of kilometers. Temporally, the stationary term is assumed to be correlated in the period from months to years. Inversely, mixing turbulent is supposed to keep correlation within less than 3 hours and turn to uncorrelated in 24 hours.

2) Based on above assumption, periodic averaging is adopted as first approach to separate both terms. With large number of stacked IWV maps, turbulence signal can be restrained, and stationary term in each map then can be modeled on globally averaged signal with a linear fitting.

3) Spatial spectral filter is adopted as second approach to differentiate between two terms. This approach is realized with implementation that we transform the spatial signal into frequency domain and separate the two terms by low/high pass spectral filtering with experiential spatial frequency threshold. Such spatial spectral filtering is valuable to discern turbulence in individual maps, which can be applicable for other spatial data.

Thirdly, with reasonable differentiation of four components (spatial linear trend, height correlated stratification, stationary term and mixing turbulence), the spatial temporal decorrelation of water vapor turbulence has been studied with MM5 IWV maps using frequency spectrum and correlation analysis. The result shows that 1~2 hour of turbulence in all scales, and even 3~4 hour of large scale turbulence are highly correlated. The result demonstrates that it provide evidence of linking of different water vapor sources with 1~3 hours of temporal gaps, for application of data synergy or mutual comparison and calibration.

The deficiency of the experiment in this chapter lies in the missing of validation for ground feature related water vapor signal. Though theoretical reasons can be explained for this signal, only validation can provide strong and persuadable evidence for such assumption. The external validation of ground feature related stationary term is suggested to be operated using fine scale land use classification map or coinstantaneous high resolution Remote Sensing Images. For instance, as a

further study, to validate the stationary term detected in this chapter with MM5 IWV, coinstantaneous 1Km MODIS multispectral images in cloud free conditions can be collected to obtain updated reliable ground feature classification map and to detect possible correlation between stationary water vapor signals and following special features: smaller water body, vegetation area, shaded area in large slopes etc.

The founding in this paper provides first evidence that spatial linear trend and ground feature related stationary term are superimposed and mutual influential with stratification and turbulence terms in water vapour. It improves the theoretical understanding of water vapor signal in atmosphere, being potentially significant for improving of water vapor modeling. This improvement of water vapor modeling would then generate engineering significance for correction of InSAR atmospheric noises in ground geophysical applications.

Chapter 4 Point-based Comparison between APS and GPS delay

With mm precision, water vapor from GPS meteorology was widely employed in various applications. Besides the previous discussions of water vapor from SAR APS, however, reliable comparisons of atmospheric delay between GPS and InSAR are never studied. In this chapter we proposed a complete comparison methodology between GPS delay and SAR Atmospheric Phase Screen (APS) in both differential and pseudo-absolute mode. ENVISAT ASAR APS and synchronous GPS campaign measurements in Como, Italy are collected for agreement analysis. Furthermore, for the purpose of clearly distinguishing turbulence signal from total delay of APS, APS has been divided into even groups according to their height. Stratified slopes of APS are then retrieved from grouped APS after the removal of 'Head effect' (influenced by turbulence) and 'Tail effect' (small number of Samples). Finally, based on above stratification analysis, the stratification terms and assumed turbulent terms from SAR APS and GPS have been compared in the differential mode.

4.1 Introduction

In the past decades various approaches were proposed to model and correct the artificial phase due to atmospheric effect in SAR interferometry. The one approach models such effect (mainly due to water vapor) with external water vapor measurements, e.g., GPS Precipitable Water Vapor (PWV) (Bevis, 1992; Williams, 1998), MODIS/MERIS (near) infrared water vapor product, predicted water vapor products from the Numerical Weather Prediction (NWP) models, Radiosonde profiles, etc. Among them, the most widely used data is independent GPS zenith delay or water vapor retrieved from the regional Continuous Observation Reference System (CORS) (Li Z.H. 2006; Xu C. 2006; Cheng 2009).

Several studies have introduced how GPS derived Zenith Wet Delay (ZWD) or Precipitable Water Vapor (PWV) can be used in atmospheric correction in InSAR. Williams et al. assessed the possibility of reducing atmospheric effects on SAR interferograms using Southern California Integrated GPS Network (SCIGN) GPS data through simulation (Williams 1998). A comparison between GPS zenith delays estimated from a 14 station continuous GPS (CGPS) network and InSAR measurements was performed over Mt. Etna, the result of which shows that the equivalent values for InSAR-GPS gave a RMS value of 19 mm with a mean of +12 mm (Wadge 2002). Li et al. employed GPS data in SCIGN to develop the GTTM model for InSAR atmospheric mitigation, especially the height dependent and long wavelength atmospheric terms (Li Z.H. 2006). However, a fully investigated result on the agreement of accurate InSAR atmospheric phase and GPS derived atmospheric measurements and reliable demonstrative conclusions of correction performance are missing for previous case studies.

To make up for the deficiency of previous studies, agreement analysis between GPS and SAR is at first time conducted. In which a comprehensive experimental comparison between GPS zenith delay and SAR Atmospheric Phase Screen was carried out with a novel comparison methodology. In this chapter, the data set values are compared in zenith delay instead of water vapor due to two following reasons. Firstly, the zenith wet delay is positively linear with water vapor for regional case. Secondly, the results demonstrated in zenith delay are closer to the InSAR atmospheric mitigation from GPS. In Section 2, both spatial and temporal coverage of ENVISAT ASAR data (both ascending and descending) and GPS campaign data in Como are described. Section 3 introduces the methodology of comparison with consideration of the different characteristics of SAR APS and GPS delay. Height sensitive stratification in APS and the determination of stratified ratio have been specifically studied in Section 4 for following comparison of the turbulence signals. Based on the methodology in Section 3 and stratification sensitivity analysis in

Section 4, the total atmospheric delay, the stratification slope and the turbulence signal (after removal of the spatial linear trend and stratification) in both differential comparison mode and pseudo-absolute comparison mode from GPS and SAR APS (ascending and descending) are compared in section 5. The conclusion and discussion are presented in the last section.

4.2 Experimental data

In order to quantitatively analyze the agreement between GPS atmospheric measurements and InSAR correspondents, we have designed an experiment of comparison between GPS zenith delay and SAR atmospheric phase. The data collection in this experiment is realized as one part of METAWAVE project funded by ESA (European Space Agency). SAR time series imagery and local GPS continuous observations have been collected in Como, Lombardy, in the northern part of Italy for the experiment.

In the experiment, SAR time series stacking images have been collected in both COMO and ROME, northern part of Italy. The whole SAR dataset have been acquired from the ESA satellite Envisat and cover the time span between 2002 and 2009.

The ENVISAT ASAR images were acquired in two selected tracks, ascending track 487 and descending track 480. The map of each track and the overlapping coverage of the two tracks are shown in Figure 4.1. The dates of data acquisition for the two tracks are shown in Figure 4.2. In total, 38 and 28 ENVISAT ASAR datasets are available for this experiment during the period 2003–2008 for track 487 and track 480, respectively. The image on date 20070715 is adopted as master in the PS InSAR analysis for both tracks. In this experiment, the Atmospheric Phase Screen (APS) for each SAR acquisition is estimated from SAR time series imagery with PS InSAR technique (Ferretti 2001) and the developed Matlab tool SARProz (Perrisin 2007;

76

Perrisin 2008). APS in two SAR tracks are processed independently. Table 4.1 marks all the dates of available SAR data in two tracks.

GPS observations were collected throughout the GPS campaign in Como, a local GPS network with an area smaller than the SAR coverage, and shown by the black rectangular box in the left figure of Figure 4.1. Eight GPS stations were installed in the Como test site at different scales (in the order of from about 5 km, 1 km to 100 m). The right figure in Figure 4.1 sketches the location and distribution of the GPS sites in Como. In the GPS campaign in Como, however, datasets were collected on six days, which were partially synchronous with SAR acquisitions, as marked by black circles in Figure 4.2.
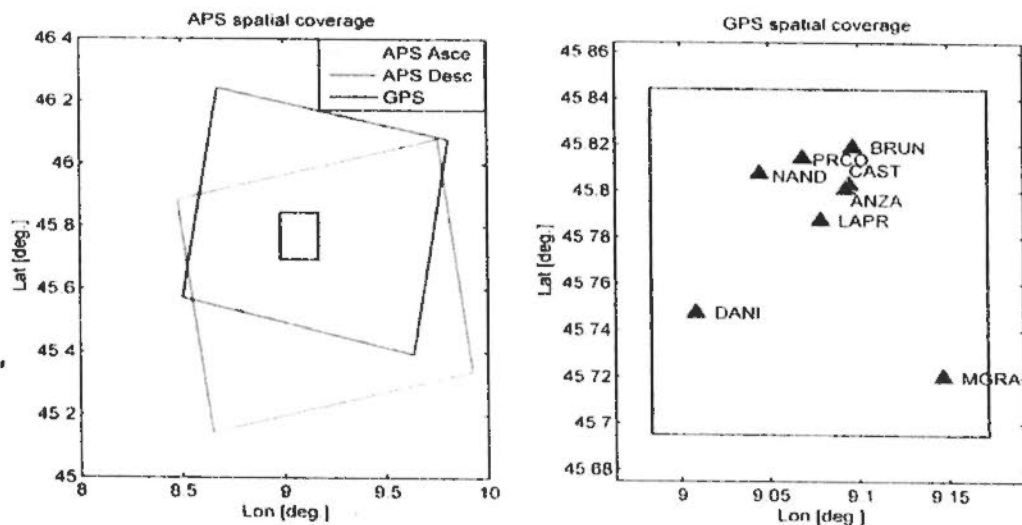
Figure 4.1 Map of SAR imagery and GPS data. Left: Red and blue rectangular boxes give the spatial coverage of SAR imagery for ascending and descending tracks, respectively. Right: Locations of GPS stations in Como, Italy, which are marked with black triangles.

Table 4.1 SAR Dataset of Track 487, ascending pass, Track 480, descending pass, over Como.

Dates of Track 487				
20030706	20050327	20060521	20070506	20080420
20030810	20050710	20060625	20070610	20080525
20031019	20050814	20060730	20070715	20080629
20040307	20050918	20060903	20070819	20080803
20040411	20051023	20061008	20070923	20080907
20040516	20051127	20061217	20071028	20081012
20040620	20060101	20070121	20071202	
20050116	20060312	20070225	20080210	

Dates of Track 480				
20021208	20050327	20061008	20070819	20080629
20030112	20060101	20061112	20070923	20080803
20031019	20060205	20070121	20071028	20080907
20040411	20060416	20070401	20080106	20081012
20040516	20060625	20070610	20080316	
20041003	20060903	20070715	20080525	
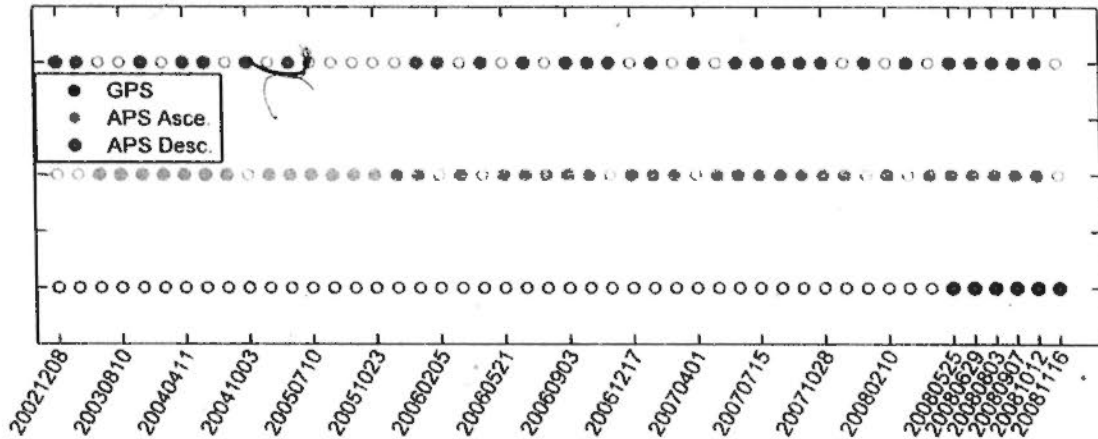
Figure 4.2 Time series of ENVISAT ASAR imagery and GPS datasets. Filled circles indicate that synchronous data are available on the listed date. Circles in black, red and blue stand for datasets of GPS, ascending SAR and descending SAR, respectively.

Table 4.2 Temporal list of GPS dataset at all stations for Como, Italy. Available hourly samples per day for each station are given in the table. NaN means that data values are unavailable on that day for the station.

Stations\Date	20081116	20081012	20080907	20080803	20080629	20080525
ANZA	25	25	25	25	25	25
BRUN	25	25	25	25	25	25
CAST	25	25	25	25	25	25
DANI	25	25	NaN	NaN	NaN	NaN
LAPR	25	25	25	25	25	25
MGRA	25	25	NaN	NaN	NaN	NaN
NAND	NaN	25	NaN	NaN	NaN	NaN
PRCO	25	25	25	25	25	NaN

For the stations operating well, hourly GPS zenith delays were retrieved under piece-wise linear model from GPS phase observations at 5 minutes intervals with precise IGS orbits. GPS data was processed with the BERNESE package. However, during the whole campaign three of the eight stations were inoperative on four of the

six days and then corresponding observation data are not available for providing zenith delay for comparative analysis. Table 4.2 gives the available dataset samples of GPS zenith delay per day in this experiment.

4.3 Implementation for comparison

To compare GPS and SAR APS for testing of their consistency and agreement, differences of atmospheric correspondence from both should be stated, then comparison framework with consistent spatial & temporal characteristics shall be constructed and correspondingly several implementations are conducted to derive comparable values of atmospheric delay.

PWV retrieved from GPS meteorology the following properties of should be clarified as follow. More detail of GPS retrieval can refers to section 2.1.2.

1) Spatially averaged PWV within an inverted cone

GPS water vapor is the averaged quantity in an inverse cone, the boundary of the inverse cone is dependent on the maximum zenith angle of the GPS observation. The water vapor amount in each slant direction was converted into zenith through a projection model to obtain the final PWV with a least squares fitting. Neil Mapping Function (NMF) with 1st order horizontal gradient is adopted in our data preparation (Niell 1996; Herring 2006).

2) Absolute PWV

PWV is the total amount of physical water vapor along a vertical profile from ground to the upper air for a given point, with the unit of kg/m^2 or mm. PWV estimated from GPS observations are spatially absolute values, This can be realized either by a Precise Point Positioning (PPP) strategy with standalone dual frequency dual code receivers, or by a differential positioning strategy with incorporation of the International GPS Service (IGS) stations into the regional Continuous Operational Reference Stations (CORS).

3) Temporal independent PWV

79

GPS water vapor is also temporally independent, which means water vapor content retrieved in different epochs (time beyond interval) have no correlation with each other. Each node of PWV time series is significant and independent in adjustment or statistics; this provides a tool to analyze the variation law of water vapor in the time domain.

For APS in our comparison, we regard spatial atmospheric water vapor signal as a composition of following four parts: spatially linear plane trend, height dependent stratification term, spatially correlated perturbation term, and ground feature dependent part, as proposed in chapter 3. This model is adopted in our analysis based on following reasons: firstly, turbulence term and stratification in the total atmospheric delay are the most important components being concerned (Hanssen 2001); secondly, spatial liner trends would inevitably bring errors in comparison due to imperfect of satellite orbits, which cannot be neglected. Though in this paper we do not dig much in ground feature related water vapor effect, we try to compare between GPS and SAR APS for specific signal components, instead of mixed signal

As APS derived from InSAR are differential measures with an interferometric way and are relative to a master image, while water vapor estimated with non-interferometric techniques (in situ observations, remotely sensed measurements, as well as model simulations, such as microwave radiometers, radiosondes, GPS, MERIS, MM5, etc.) are spatially and temporally absolute measurements. The difference in such characteristics blocks the direct comparison between SAR APS and absolute water vapor in our experiment. In order to obtain reliable comparison results, we must resolve the characteristics difference from two datasets and only rely on comparable values within comparison.

Then in this chapter we propose a comparison methodology to transform the GPS delay into differential values or to recover the SAR APS in absolute values, and then to compare them in two ways: differential and absolute-pseudo way. According to the domain of comparable values, we classify the comparison between GPS and

APS correspondences into two modes: the differential mode and the absolute mode. The differential mode of comparison was implemented by subtracting GPS ZTD at master time of APS from the original GPS delays. Usually, with the differential characteristic, APS do not require the corresponding differential operation. However, if the original APS master chosen in PS-InSAR processing was not covered by the GPS data series, then a differential operation between corresponding pairs (synchronized to GPS) was required. In this case, the differential operation cancelled out the common unknown atmospheric delay of the original master date and then comparable values are kept with exact consistency of physical meanings. The concept of absolute comparison is to estimate the SAR master APS from GPS time series and then to compensate all SAR APS for atmospheric delay of master time with approximately estimated ones. The comparable values of both SAR APS and GPS ZTD are finally compared in the absolute domain. Because that comparison is in the absolute domain and atmospheric delay of the SAR master time could not be genuinely recovered from the GPS time series, this mode can be called the pseudo-absolute comparison.

Besides the implementation of temporal interpretation ambiguity, as discussed in section 3.3, in order to enable the two datasets into comparable values, four additional disagreements must be specified and correspondingly implemented before comparison.

1) The link between SAR APS phase and SAR zenith delay should be built to compare with GPS. Considering that the GPS Zenith Tropospheric Delay (ZTD) is calculated in the one-way vertical direction while the radar signal transmits with an incidence angle (e.g., 23°, swath 2 of ENVISAT ASAR) in two-ways, the Mapping Function of the incidence angle must be accounted for. Simplifying the model, a cosine Mapping Function was adopted to project the radar phase in the line of sight into vertical delay as in equation 4.1 (Cheng 2009):

$$\varphi(\text{APS})_{LOS}^{2way} = \frac{ZWD \cdot 4\pi}{\lambda \cdot cos(\theta_{inc})} \tag{4.1}$$

In above equation, λ is wavelength of radar, and θ_{inc} indicates the local incidence angle. With the given link between SAR APS phase and SAR zenith atmospheric delay, the comparable atmospheric delay is expressed in mm in the following context of this paper if no additional specifications are given.

2) The relationship between PWV, ZWD and ZTD from GPS shall be stated. With a locally constant factor, ZWD keeps a directly linear relationship with PWV. And through a spatial temporal difference operation, there would be no difference between ZWD and ZTD when comparing with SAR APS. Therefore, though PWW from GPS is theoretically introduced in last section, considering above two factors, ZTD directly retrieved from GPS are practically used for comparison and analysis.

3) It is also required to geo-code SAR APS to a common geographic system and to resample APS into GPS overlapped locations to keep the signals comparable. In the following part, the SAP APS have been transformed and resampled into the WGS84 grid, and interpolated into the same geographic locations as GPS before point-based comparison. In our experiment, if the data of one GPS station are unavailable for a given day, the interpolation on this location on the given day is neglected.

4) Spatial linear trends should be carefully considered and removed from APS, if required. The residual orbital phase due to inaccuracy of orbit products cannot be distinguished from APS in PS processing, so a linear phase trend should be removed from APS. To keep consistency, we intended to estimate and remove spatial linear trends from GPS too, but we gave up this intention when considering following two reasons. The first one is that the GPS atmospheric delays on Como stations are spatially independent because synchronous observations from a wide GPS reference network are introduced in processing. The second is that it can highly possibly lead to

82

instability in estimation of the spatial trend with the limited number of GPS stations in our case.

5) Removal of mean values in space for GPS. SAR APS are spatial differential signals, which are referred to one reference point adopted in PS processing. In order to keep consistency between GPS and SAR APS, we removed the spatial average of same samples to cancel out the unknown bias existing between the GPS absolute delay and the spatially differential APS.

4.4 Height sensitive stratification of APS

It was mentioned that height dependent stratification was one influential factor of the atmospheric effect on InSAR in comparisons in previous studies (Hanssen 2001), but detailed analyses of such stratification had not been performed and compared with correspondence from other sensors. In this experiment, we compare the correspondence of atmospheric delay for GPS and SAR APS, not only total delay, but also stratification terms and the assumed turbulence. But as stated before, the spatial linear trend, the stratification term, and turbulence terms co-exist in SAR APS; different terms must be clearly discriminated before comparison.

In this section, we firstly extract the height dependent stratified term for both SAR APS and GPS; the Phase to Height ratio is regressed from scatter points. As given in statements above, delay caused by the spatial linear trend, stratification and turbulence are mixed together on APS. Then reliable estimation of the stratified ratio from APS cannot be directly established, and instead requires special analysis. In the analysis we divide APS into even groups according to APS height and then calculate the mean value and standard deviation of the APS within each group.

The mixed effect of turbulence and stratification can be observed in Figure 5.3, in which the one-way zenith delay against height is plotted. From Figure 5.3, we can find a clear linear trend of APS delay on APS height, especially in the ascending cases. This linear trend is directly caused by the stratification effect on SAR

interferometry, which we focus on and analze for comparison in the experiment. However besides the linear trend, unexpected noises and an abnormal trend of APS delay at lower heights can also be observed, e.g., in the 20080629 ascending and descending data. Besides this, the noise of APS in the descending pass is larger than that of the ascending pass.
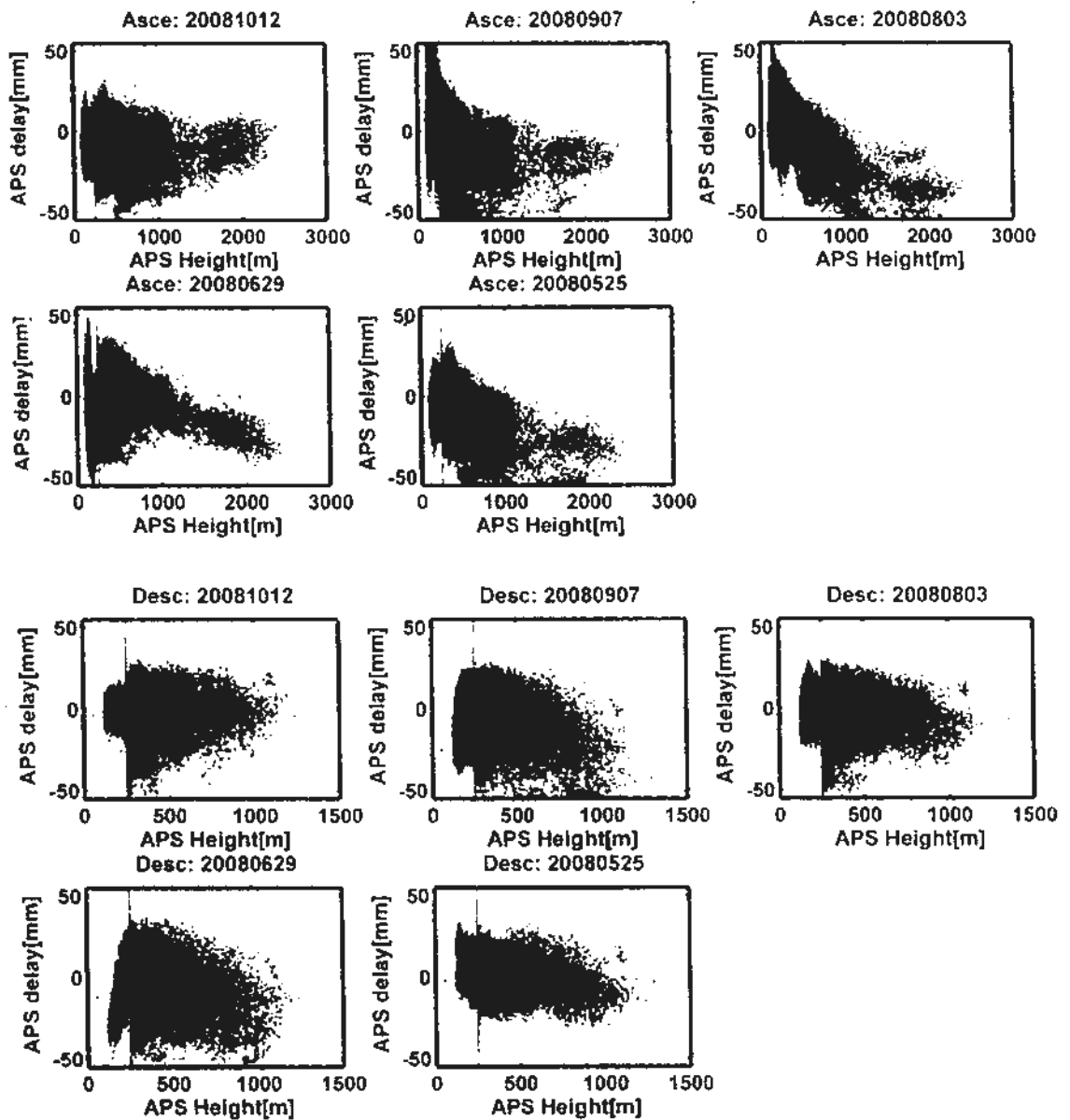
Figure 4.3 One-way zenith delays of SAR APS against APS height for the dates synchronous with GPS. Top: Ascending track. Bottom: Descending track. The red vertical lines in all graphs show APS at a height of 250 m, for ascending and descending. Blue scatter points stand for original APS; Black points represent APS after removal of the spatial linear trend.

From Figure 4.3, a critical height of APS at 250 m, represented by a red vertical line in both ascending and descending cases, can be observed. APS points under the height have a reversed tendency compared to those of higher APS. In most cases, the standard deviation and range of APS under this critical height are remarkable larger than average. We can assume that the abnormal line in the original APS (in blue color) is mainly caused by the spatial linear trend effect.

Then this could be partly validated by the scatter points of APS after the removal of the spatial linear trend, given in black color. In the scatter points, the standard deviation of APS decreased, but the trend of APS at larger heights is kept unchanged. In addition, the trend of APS under the critical height has been rectified (e.g., in date 20080907 of the ascending track).

We divided APS into even groups based on the APS height with experiential steps. The purpose of this operation is to differentiate the different effects in mixed signal and to better observe the whole curve from each group. Considering that the range of APS height for the ascending track is 2400 m, larger than that in the descending track of 1400 m, the experiential steps we take are increasing from 100, 160 to 250 m for ascending, and increasing from 60, 100 to 160 m for descending. Through our experiment, the curves of the mean slope keep close to each other. In Figure 4.4, we only show the case for ascending with step of 160 m and descending with step of100 m for grouped APS. The mean delay, STD and samples for each group are given in Figure 4.4.
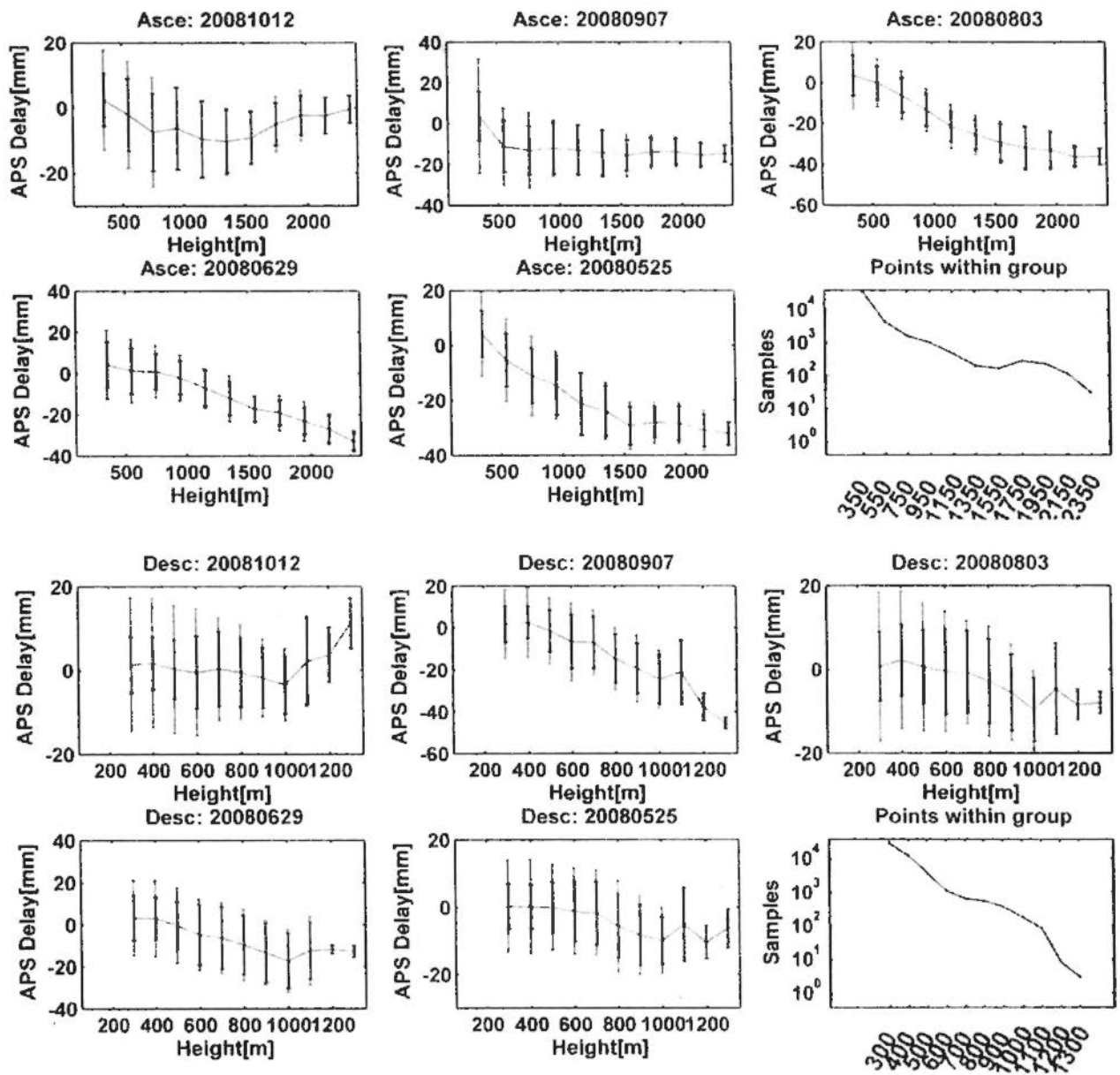
Figure 4.4. Mean, standard deviation error (in black) and a quarter of range (in blue) of grouped APS delay after removal of spatial linear trend. Each group is determined by APS height, which increased in steps of 200 m for ascending and 100 m for descending. The solid black dotted line is added in the last sub-graph to represent the total sample numbers in each APS group.

In the Figure 4.4, we calculate the mean, standard deviation and quartered range (25% of difference between Max. and Min.) of APS in each group after removal of the spatial linear trend, beginning at the height of 250 m. From Figure 4.4, with the increase of APS height, the range and standard deviation of grouped APS decreased, and the APS samples in each group also exponentially decreased for both tracks.

From Figure 4.3, the large variation at the head of the curve of APS scatter points and high sparsity at the tail of the curve can be observed. Same phenomenon could be evidenced in grouped APS curves in Figure 4.4. The range and deviation of grouped APS in lower heights (from 250 to 850 m for ascending and from 250 to 550 m for descending) is higher than that at the larger heights, primarily affected by mixing turbulence in lower ground elevations. We take this phenomenon in mixed APS signals as 'Head effect'. While, the APS beyond larger heights (2050 m for ascending and 1150 m for descending) have samples of under 100 and are not accepted as reliable APS in stratification analysis, referring to the last sub-graph in Figure 4.4. this phenomenon in mixed APS signals can be taken as 'Tail effect'. In order to obtain a reliable stratification term, we must neglect Head effect (turbulence effect) and remove the Tail effect (small samples at large heights) in the comparison analysis in next section.

4.5 Point-based Comparison Results

In this section, besides a comparison of absolute zenith delay between GPS and SAR APS, standard deviations of GPS, of SAR APS delay, and of the difference between both are also listed to show individual dispersion and mutual consistency between GPS and APS in different comparison modes and at different comparison stages when neglecting several APS terms. At the beginning of the comparisons, the sensitivity of the stratified ratio on the height threshold in polynomial fitting under a mixture of turbulence and stratification are analyzed. The estimated slope of delay to height between GPS zenith delay and SAR APS is also compared under the linear assumption of the stratification term. In addition, correlation coefficients of zenith delay and of estimated stratified ratio between both data sets are listed in a table to index their agreement.

4.5.1 Differential Mode

In differential comparison mode, we transform absolute GPS delay into spatial and temporal differential values and then make comparison with SAR APS in the differential domain. 10 differential APS are generated by randomly selected pair from 5 SAR images for each track. Differential delay values have been implemented on GPS as introduced in section 3. In the differential mode, stratified slope is compared firstly, followed by total delay and assumed turbulence delay.

1) Comparison of stratified ratio

In Section 4, we analyzed the height sensitive stratification under a mixture of spatial linear trend, turbulence and stratification. In this differential mode, we first plot the scatter plots of both datasets on height.
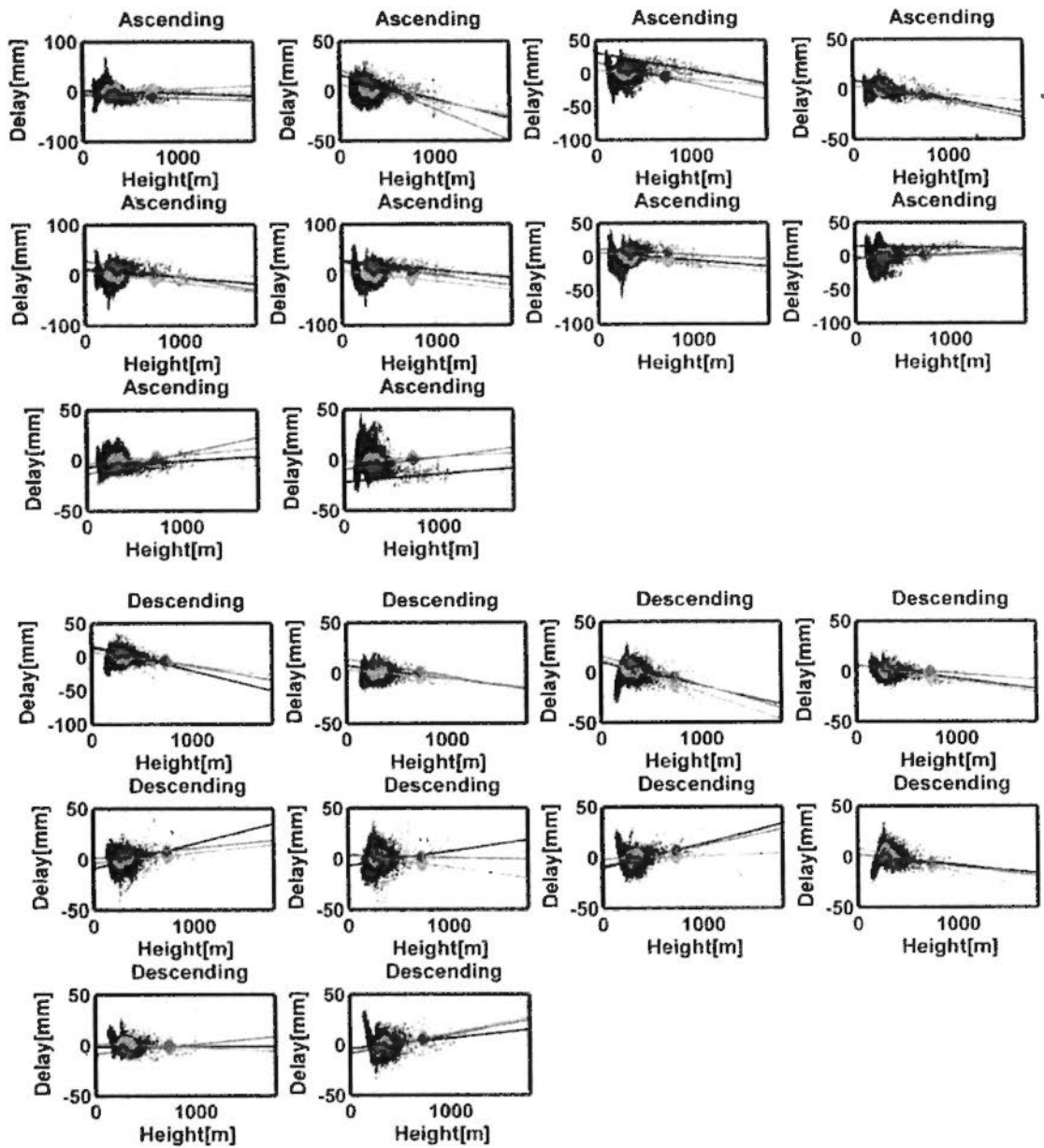
Figure 4.5 Atmospheric delay against height for original SAR APS and original GPS ZTD. Ascending (Left) and descending (Right). In both sub-graphs, the black color is for original SAR APS values, blue symbols stand for the interpolated APS points geographically overlapped with GPS stations, while the GPS delay are plotted in red. Fitted lines by linear regression are plotted to represent their estimated stratified ratios.
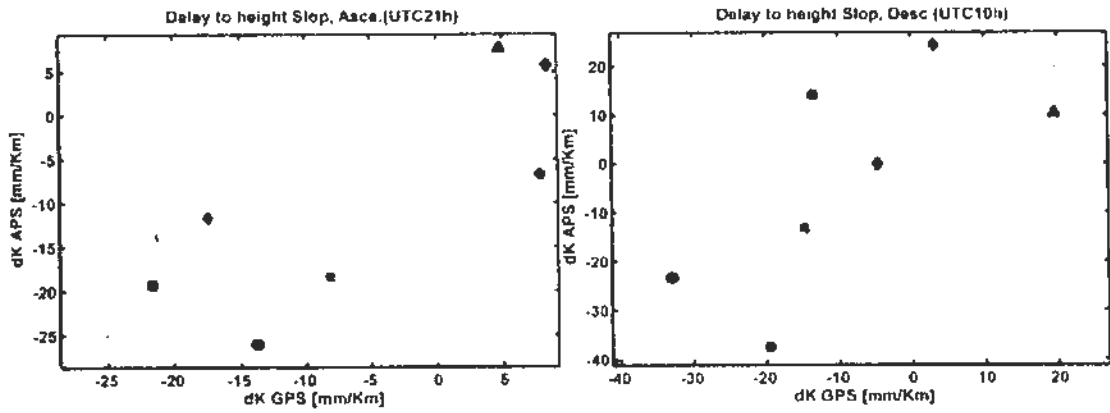
Figure 4.6 Cross plot of estimated stratified ratio from the original GPS ZWD and the original SAR APS. In the upper sub-graphs. the stratified ratios are estimated from the original SAR APS. (Left) ascending and (Right) descending pass. Unit of the stratified ratio is mm/Km.

Table 4.3 The statistics of Stratification Ratio from GPS delay and SAR APS. Unit: mm/Km

APS vs. GPS	Corr. Coef	Bias	STD Diff.	Slope	Intercept
Ascending	0.81	3.39	7.73	0.76	-5.29
Descending	0.74	-6.11	13.92	0.96	5.73

Figures 4.5 and 4.6 provide one direct perspective of atmospheric delay against ground height. From the statistics in Table 4.3. calculated from Figure 4.5 and Figure 4.6, we find that APS and GPS have comparable stratification; the estimated stratification ratios from both datasets coincide with each other with a correlation coefficient of more than 0.7, but the ascending track performs better than the descending one. The bias and standard deviation of differences of stratification ratio between GPS and SAR APS in ascending (3.4 and 7.7) are much smaller than that in descending (6.1 and 13.9).

2) Comparison of atmospheric delay

In this section, we compare the atmospheric delay. including the total delay and delay after removal of the spatial linear trend, as well as height dependent stratificaiton that was estimated in the last section. According to the assumption in our model, the residual delays are mostly caused by turbulence effect; then we simply take the residual signal as turbulence delay. The comparision results are given

90

in Figures 4.7–4.9. From the figures, we integrate all samples of comparable values on each date pair and calculate the following global statistics: STD of GPS, STD of SAR APS, STD of difference between both, correlation of both series, slope of APS delay on GPS. The above statistics in different stages are listed in Table 5.3.
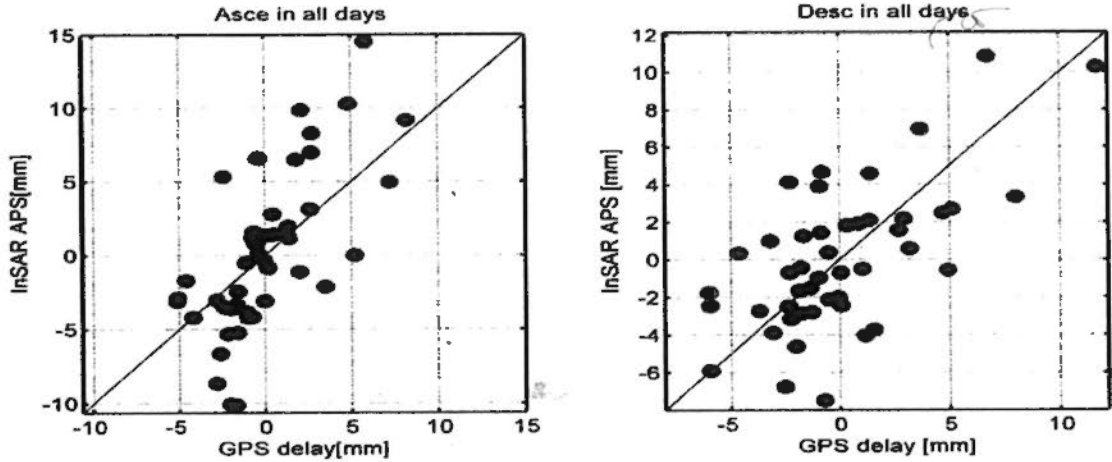
Figure 4.7 Cross Plot of zenith atmospheric delay (Total delay) between GPS and SAR on all temporal pairs in the differential comparison. (Left): Ascending track. (Right): Descending track. Individual spatial averages at available overlapping stations for both datasets are removed for comparative demonstration.

Figure 4.8 Cross Plot of zenith atmospheric delay (after removal of spatial linear trend) between GPS and SAR on all temporal pairs in differential comparison. (Left): Ascending track. (Right): Descending track. Individual spatial averages at available overlapping stations for both datasets are removed for comparative demonstration.

Figure 4.9. Cross Plot of zenieth atmospheric delay (turublence delay) between GPS and SAR on all temporal pairs in differential comparison. (Top): Ascending track. (Bottom): Descending track. Linear spatial trend and stratification effect are removed from the original APS, stratification on GPS stations are removed for comparable demonstration. Individual spatial averages at available overlapping stations for both datasets are removed.

Table 4.4. Statistics of differential comparison between GPS and SAR APS at two stages. Unit: mm.

Atmospheric delay (10 Pairs)	Ascending					Descending				
	STD GPS	STD APS	STD Diff.	Corr. Coef.	Slope (APS V. GPS)	STD GPS	STD APS	STD Diff.	Corr. Coef.	Slope
Total delay	3.02	5.44	3.99	0.69	1.25	3.58	3.86	3.16	0.64	0.69
Turbulence delay and stratificaiton	3.02	4.99	3.09	0.81	1.34	3.58	3.62	2.99	0.66	0.66
Turbulence delay	1.39	2.95	2.60	0.47	0.99	1.71	2.12	2.94	-0.16	-0.20

From Figure 4.7, 4.8 and 4.9 and Table 4.4, we can found following detain from scatter points and index:

1) As shown on the stage of total delay in the first row, after the removal of individual averages, and without any additional operations, the GPS delay and SAR APS agree with each other in differential mode with the standard diviation of the difference being less than 4 mm and the correlation coefficient being higher than 0.6.

2) As shown on the stage of turbulence and stratification delay in the second row, after removal of the spatial linear trend in the original APS, the agreement between the two datasets is stronger, with higher corrlation and smaller standard deviation.

3) As shown in the third row, after removal of both linera trend and height dependent stratification term, the assumed atmospheric turbulence term from GPS and SAR APS is moderately correlated with a coefficient near to 0.5, while the standard deviation of difference decreased to less than 3 mm for the both tracks.

Some general law can be drawn from figure series and corresponding numbers in Table 3, as our summary of comparison in differential mode. Agreement between GPS delay and SAR APS generally holds in most cases. For the original total delay (or only including stratification and turbulence), dispersion of GPS are smaller than that of APS it self. With the help of GPS zenith delay, APS noises can be reduced at a certain extent by a differential (between GPS and APS) operation. Even for only assumed turbulence, with the height sensitivity analysis of stratification in section 4, turbulence delay from GPS can still be possibly employed to mitigate the turbulence signal from APS, which could be evidenced by the change of STD (2.95 for STD of APS to 2.60 for STD of difference) in SAR ascending track.

For the ascending track, the reasons for the decrease in correlation are: 1) The stratification ratio estimated from GPS and SAR APS has a standard deviation of more than 7 mm/km, as shown in the last section; 2) Most (7 of 8) GPS stations are located at lower heights, but the stratification term on APS are removed on all the APS scatter dataset. When APS are interpolated on GPS stations, the removal of the linear trend on all APS may introduce artificial model error on interpolated APS points because that 7 of 8 stations are at lower height. The decending track shows no correlation for the turbulence term between both; this is because of the large RMS

error in the APS data itself, and the uncorrelated stratification ratio-the STD differences in ratios are at about 14mm/ Km.

5.4.2 Pseudo absolute mode

The first implementation of this pseudo-absolute comparison is to estimate the SAR atmospheric delay of master time as an average of all GPS temporal series data (all hours within all days). Then one following step is executed in this pseudo-absolute comparison: either to add the estimated master delay onto APS or to subtract it from GPS. The second implementation steps of the pseudo-absolute comparison include that of extracting GPS ascending and descending time series (synchronous with SAR APS) respectively, according to their passing time, and then to estimate the SAR atmospheric delay of master time with the average of the synchronous GPS temporal series. Similar to operations in the last approach, two choices could be made on data in this implementation: to add the master onto APS or to subtract the master from GPS.

Figures 4.10 and 4.11 illustrate the comparable atmospheric delay between GPS and SAR APS at different stages as well as in different implementation approaches; different colors stand for different available stations. Generally, a good correlation in total delay can be observed in both figures and the correlations in turbulence delay are decreased. Similar to the differential comparison, we give statistics to quantitatively describe the relation of atmospheric measurements between GPS and SAR APS (referring to Table 4.5).
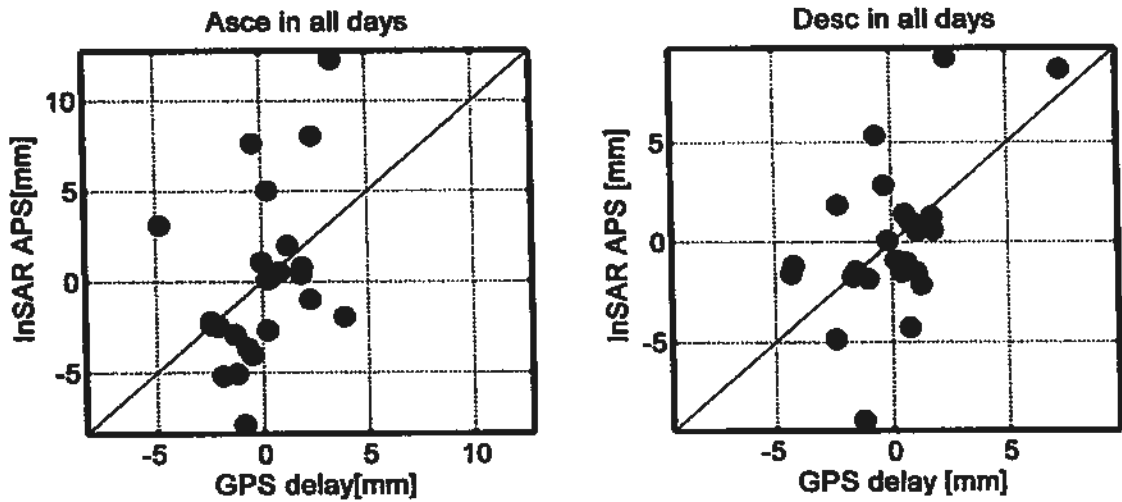
Figure 4.10 Cross plot of zenieth atmospheric delay between GPS and SAR in pseudo-absolute comparison. While different from Figure 4.8, the SAR master delay was estimated with the average of all GPS data and subtracted from the GPS series. (Left): Ascending case. (Right): Descending case. Individual spatial average at available overlapping stations for both datasets is removed for comparative demonstration.
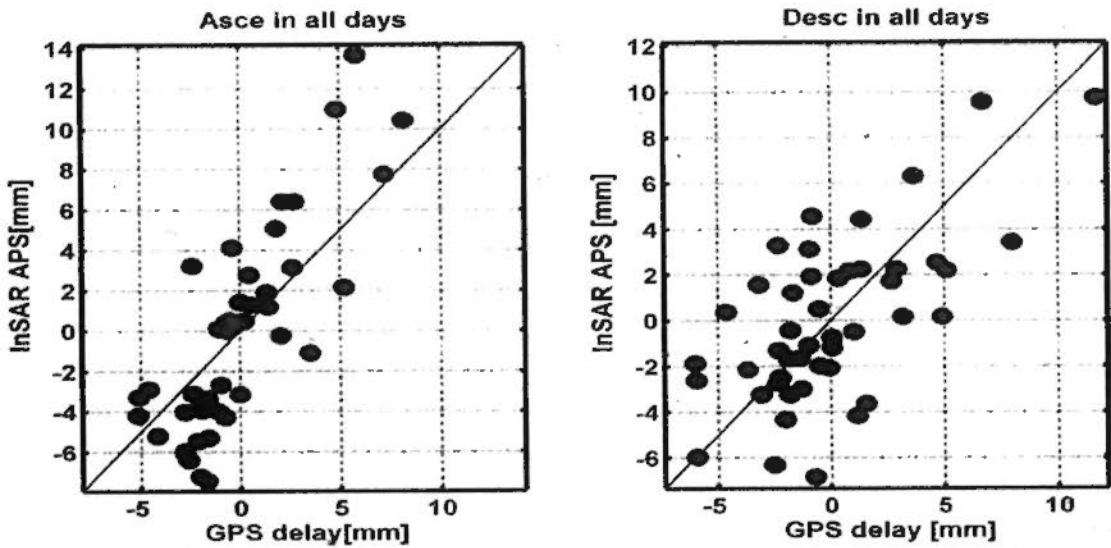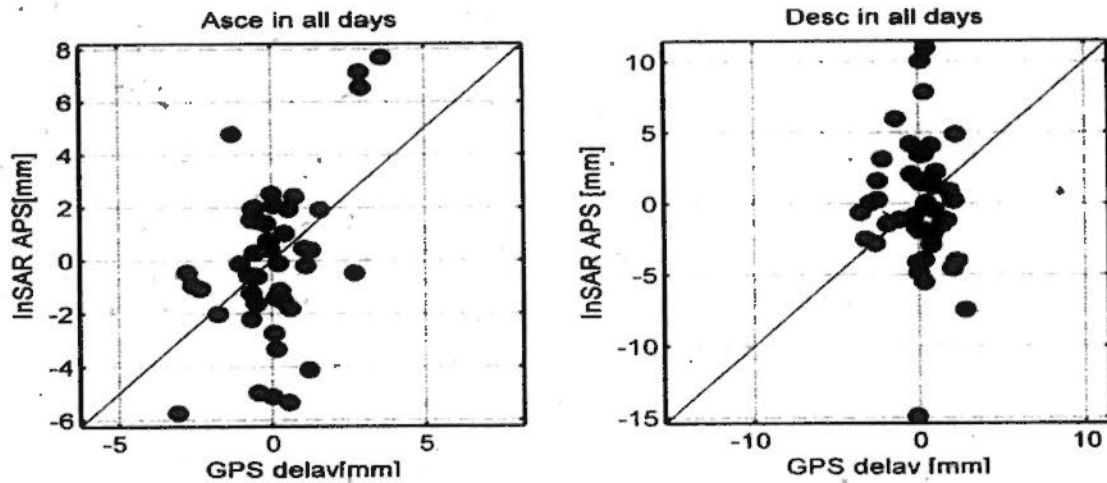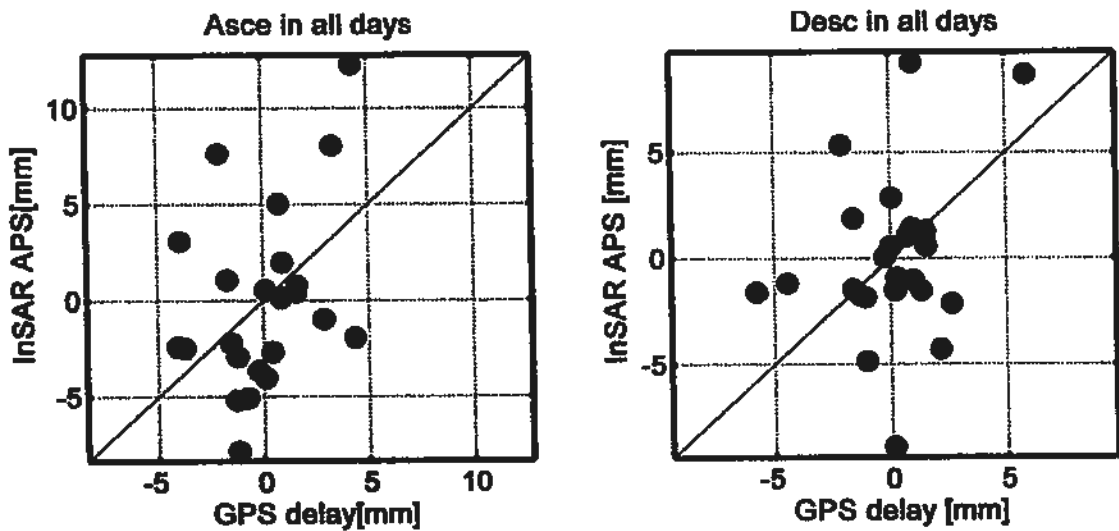

Figure 4.11 Cross plot of zenieth atmospheric delay between GPS and SAR in pseudo-absolute comparison. SAR master delay was estimated with the average of synchronous GPS data and subtracted from the GPS series; individual spatial means were both removed. (Left): Ascending case. (Right): Descending case. Individual spatial averages at available overlapping stations for both datasets were removed for comparative demonstration.

Table 4.5 Statistics of pseudo-absolute comparison between GPS and SAR APS for total zenith delay. Statistics for two implementation approaches of SAR master delay estimation are included.

Absolute mode	Ascending	Descending

95

Total delay (all 5 days)	STD GPS	STD APS	STD Diff.	Corr. Coef	STD GPS	STD APS	STD Diff.	Corr. Coef
All GPS	2.03	4.65	4.26	0.40	2.36	3.91	3.28	0.55
Synch. GPS	2.33	4.65	4.37	0.37	2.31	3.91	3.94	0.28

Table 4.6 Samples of GPS in SAR master estimation in pseudo-absolute comparison between GPS and SAR APS.

Average on station		ANZA	BRUN	CAST	DANI	LAPR	MGRA	NAND	PRCO
Average of all GPS	Asce.	150	150	150	50	150	50	25	125
	Dsce.	150	150	150	50	150	50	25	125
Average of synchr. GPS	Asce.	5	5	5	1	5	1	1	4
	Dsce.	5	5	5	1	5	1	1	4

From Table 4.5, we can summarize the following points:

1) Correlations in the pseudo-absolute comparison mode are not as high as those in the differential comparison mode because the recovered master is not the genuine SAR master delay but approximately estimated from the average of GPS series.

2) STD of GPS data are evidently smaller than STD of APS. STD of difference between two datasets in pseudo-absolute comparison mode are slightly smaller than that of APS it setlf in most cases. Though with different implementation, deviation of difference between two datasets are kept at the same level with STD being less than 5 mm in all cases.

3) Master delay estimation with the average of all GPS provides a better comparable result than average synchronous GPS, because the GPS samples for averages in our comparison are extremely plentiful (referring to table 4.6), enabling reliable average values as a substitute of the SAR master delay, while the case of averaging synchronous GPS does not.

4.6 Conclusion and discussion

In this chapter, the stratification effect of APS with a mixture of turbulence as well as spatial linear trend is analyzed and two comparison modes between GPS and

APS are implemented for the first time. The first significant finding in this paper is that GPS ZWD is directly proved to be comparable with SAR APS in our investigation. With height determined grouped APS, after removal of the spatial linear trend and neglecting mixed turbulence at lower heights, the stratification ratio of APS derived in this experiment coincides well with that of GPS. The slopes from both correlate with a coefficient higher than 0.8 with bias (GPS-APS) of 3.4 mm/Km as well as a STD of difference of 7.7 mm/Km in the ascending case in the differential comparison. Though with more noise and a larger STD of difference, slopes for the descending case still gain correlation with coefficients of 0.74.

The differential comparison mode is physically representative of difference between the two data sets. In the differential comparison mode, the original delay from APS and GPS in 10 differential pairs have correlations higher than 0.6 in both tracks. The correlation increased and the STD of difference decreased after the removal of the spatial linear trend. When considering and removing the stratification term, agreement between the residuals of GPS ZWD and SAR APS is distinctly decreased; this could be acceptable because of additional inconsistency of the stratification between both. Though the performance varies, the atmospheric delay between GPS and SAR APS coincides with the STD of difference smaller than 4 mm (~ 0.65 mm PWV) in different stages in the differential comparison.

A second significant finding is that it is possible to restrain atmospheric noises in SAR interferometry with high precision GPS meteorological products, which is directly evidenced by the fact that the STD of delay difference (between GPS and SAR APS) are mostly slightly smaller than STD of SAR APS itself in both comparison modes. STDs of differenced are reduced compared to APS when GPS is introduced, except for the turbulence term in the descending track.

Pseudo-absolute comparison results are also provided. Comparatively, pseudo-absolute comparison is only approximately implemented, which inevitably brings implementation errors, but it still provides an alternative vision in comparison.

The agreement of atmospheric delay in pseudo-absolute mode was slightly worse than that in differential mode, which could be accepted because the nominal term and master delay are just approximately estimated. For two implementations of the pseudo-absolute mode, taking the master delay as the average of the entire GPS temporal series can enroll more data samples, providing a stable estimation. Due to the different physical nature of GPS and SAR, we cannot expect the stratification from GPS and APS to be totally correlated.

Another point from our results is that the ascending track provides reliable and comparable results and good evidence for our motivation, while the descending track does not. The first reason for this is the large noise in the APS data itself (refer to Figure 4.3); the second reason is that the height range of the descending track is much smaller (only 1100 m).

As previously studied, GPS data only provides the possibility of such atmospheric mitigation; however, the performance of such mitigation still depends on other factors: 1) Strategy and accuracy of zenith delay retrieved from GPS, 2) Spatial separation and distribution of GPS stations, 3) Statistical model for predicting every interferometric spatial pixel and known GPS atmospheric delay, and 4) Other factors bringing sensitivity of atmospheric effect on InSAR e.g., local topography, local ground feature, ionospheric activity (intensity and abnormity), which can be more influential on long wavelength SAR interferometry.

Chapter 5 Map-based comparative spatial analysis of synchronized water vapor

In this chapter, with the primary motivation of enhancing the understanding of spatial characteristics of water vapor, we employ water vapour data from MERIS images, MM5 simulated products and from SAR Meteorology to analyze the spatial stochastic law of each water vapour component, especially the effect of stratification and turbulence. Spatially overlapped and temporally synchronized data are compared with implementation of differential comparison mode and pseudo-absolute mode, as same as that in chapter 4. In differential comparison mode, isotropic variograms and rotated 1D spectrum for three data sources are given. Besides, anisotropic characteristics with 2D variogram from water vapor are observed. In pseudo absolute mode, differential water vapor from APS was recovered with MERIS values at SAR master time. Water vapour spatial behavior studied in this research would be significant to construction of fine scale (equal or smaller than 1km) 2D water vapour field, and also understanding of spatial stochastic law toward the final solution of InSAR atmospheric artificial fringes.

5.1 Introduction

Water vapour, strongly varied in space and time, is worst modeled with current observation data and retrieving technology up to now. The true law of spatial temporal variation of water vapour in different space and time scales are still challenging and unsolved to scientific communities (Hanssen 2001).

With the development of satellite observing techniques, increased satellite data are available for retrieval of water vapour and its spatial analysis. The typical map-based water vapor products are including: NIR water vapor images retrieved from double channel (one of which is water vapor absorbing channel) by split window method (e.g. MODIS and MERIS) (Li. Z.H. 2004; 2005), Numerical

weather prediction model products. In latest ten years, SAR interferometry have also been developed providing large coverage and fine scale differential water vapour maps (Hanssen 2001; Ferretti 2005; Perissin 2009)

With recent paramount amount of SAR interferograms and above kinds of external independent water vapour dataset, many previous studies are focused on spatial stochasticity discovery for further modeling of atmospheric signal. The typical results can be reviewed as follows. Kolmogrov turbulence theory was firstly proposed to describe the atmospheric turbulence process, with the assumption of conservation of turbulent atmospheric energy, he proposed the spatial power law of atmospheric processes (Tatarski 1961). Goldstein firstly obtained the power spectra of atmospheric signals in one SAR interferogram. The derived spectra followed a power law distribution with a power exponent of -8/3, which agreed the nature of scale invariance proposed by Kolmogrov Turbulence theory (Goldstein 1995). Hanssen analyzed the spectra of atmospheric signals in 26 SAR interferograms over Netherland. He found though uniformly following the power law, power exponent of atmospheric spectrum varied from -5/3, -8/3 to -2/3 in different three spatial scales or regions (Hanssen 1998). While Li., etc. proposed a GTTM model to consider both turbulence signal based on above laws and ground elevation correlated stratification in SCIGN with GPS data (Li 2006).

But look through all above results, only turbulence and stratification are considered. While as suggested by previous study (Hanssen 2001) and discussed in chapter 3, spatial linear trend effects and also ground feature correlated stationary term shall also be included and differentiated carefully. With the motivation of better understanding of water vapour variation law for atmospheric modeling and mitigation in InSAR as well as other meteorological applications, the spatial law of water vapour in aspect of decorrelation, power spectrum and structure function with kinds of synchronous experimental data are deeply studied in this study.

In this chapter, the author firstly introduces different independent water vapor products, including water vapor dominated atmospheric phase derived from SAR, MM5 simulated water vapour products from Numerical Weather Prediction model and EVISAT boarded MERIS near Infrared Water vapour images, spatially co-located and temporally synchronous in Rome at the center of Italy. Secondly, we propose the methodology to do decorrelation analysis of water vapour with following tools: Power Spectral analysis, Variogram analysis. With an enhanced water vapour signal model illustrated in Chapter 3, classification of water vapour effect into spatial linear trend, stratification, mixing turbulence term and ground feature related term, we then characterize the spatial spectrum and signal structure function as well as direction determined inhoemengenity.

Water vapour stochastic behavior studied in this research would not only be significant to discern the potential of fine scale (equal or smaller than 1km) 2D water vapor field, significant in regional climate model synergy and local weather predication, but also be significant in enhancing of water vapor modeling toward the final solution of InSAR atmospheric effects, which is critical in various geophysical applications.

5.2 Water vapor data

25 MERIS water vapor images, 31 days (more than 24 hourly per day) MM5 simulated water vapor images, 27 SAR Atmospheric Phase Screen (APS) maps processed from ENVISAT ASAT track 351 in ROME are collected for this research within the METAWAVE project funded by ESA.

5.2.1 Spatial and temporal coverage of data

MERIS Water vapor maps in this experiment are ENVISAT MERIS level 2 products estimated with a quadratic model of water absorption band provided under the METAWAVE project funded by ESA (ESA 2006). The acquired MERIS water vapor images are in Full Resolution (FR) mode with 360m* 250m patial resolution

with declared accuracy of 10% of relative water vapor amount about 1.6mm under cloud free conditions (Bennartz and Fischer 2001; Albert 2001). Water area and cloud area (which is not constant for each image) are masked from MERIS water vapor map, because water vapor values in those areas are not reliable and unsuitable for further spectral analysis. The spatial coverage and temporal range of MERIS data is referred to figure 5.1 and 5.2. The available pixels in each acquired image after cloud mask are plot in figure 5.3.

MM5 Integrated Water Vapor (IWV) data in this research experiment are simulated products of Numerical Weather Predication (NWP) model, generated on $130*130 \text{ km}^2$ surface centered at Roma, Italy, referring to Figure 5.1. More detail of MM5 model operations and input& output data could refer to official website of National Center for Atmospheric Research (NCAR)/Pennsylvania State University or related references (Grell 1995; Kistler 1999). More than 775 simulated IWV hourly maps on 32 dates are acquired during 2002 to 2008, as shown in Figure 5.2. These water vapor maps are highly suitable for spectral analysis of water vapor signal because they have sufficient detail of dynamic characteristics both in space and in time. With multiple-nested capability with increasing resolution in spatially horizontal domain, the water vapor maps employed in this experiment, own spatial resolution of 1km and temporal interval of 1hour.

The ENVISAT ASAR images were acquired from ESA in one selected track, descending 351. The spatial coverage of the track is shown in Figure 5.1. Totally 29 descending ENVISAT ASAR imagery during the period 2003-2008 are preferred as interferometric analysis and selected to retrieve Atmospheric Phase Screen (APS). APS for each SAR image are estimated by PS-InSAR technique with Matlab tool 'SAR PROZ' (Perissin 2007; 2009). SAR APS derived from PS-InSAR are temporally differential values relative to master reference, and spatially differential referring to one reference point. From figure 5.1, we can find some blank area in APS map because that no APS could be retrieved in those area, e.g. water body,

vegetation or forest area where SAR signal in different epochs are decorrelated and unable for interferometric analysis.
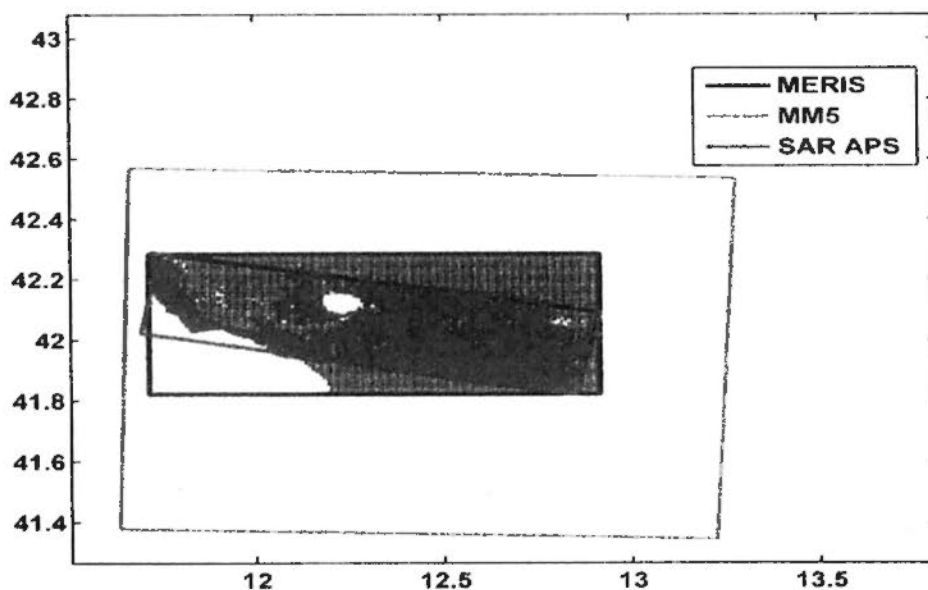
Figure 5.1 Spatial coverage of MERIS images (in black), MM5 water vapor maps (in red) and SAR APS maps (in blue) in our experimental area, Rome, Italy. The unit is degree (For better illustration of geospatial coverage, you'd better plot projected coverage)
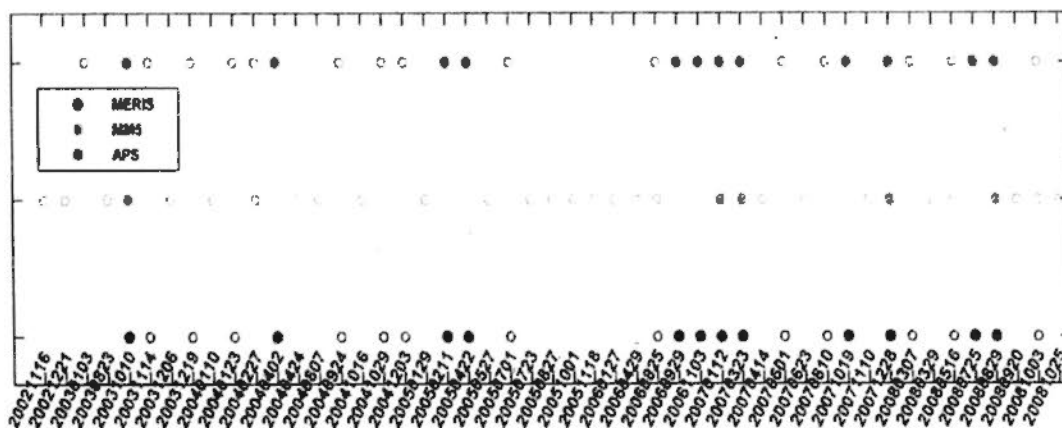
Figure 5.2 Temporal coverage of experimental data: MERIS images (black), MM5 (red) and SAR APS maps (blue). The dates are listed in abscissa, the filled circles mean selected from all empty circles for spectral analysis for each kind of data.
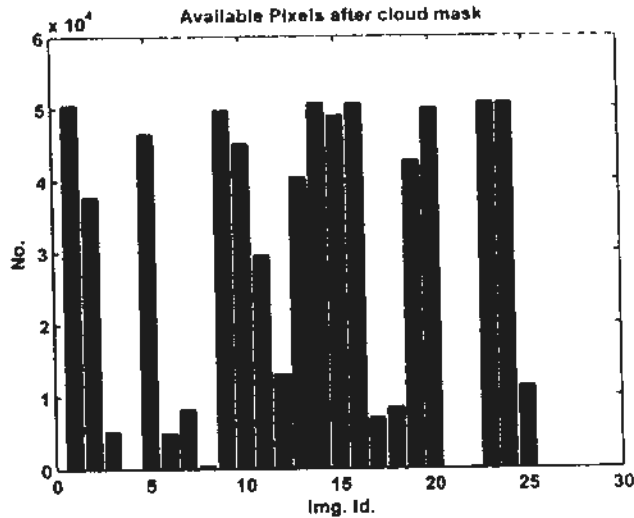
Figure 5.3 bar figure of available pixels from collected MERIS images after cloud mask.

The figure 5.1 and 5.2 draw exact spatial & temporal coverage of each kind of above data acquired in this experiment for spectral analysis. The figure 5.3 plots the number of available pixels in each MERIS image after cloud mask. From figure 5.2, eight synchronous dates from all candidates are obtained, but three of them (20060825, 20080516, 20081013) are extremely contaminated due to small number of available pixels and therefore abandoned. Then data on only five days (20031010, 20070112, 20070323, 20071228, and 20080829) are selected as data samples for synchronized comparison. From above 5 synchronous days, data from whole three kind of dataset, we plot their water vapor in different stages, with considering the water vapor component model proposed in chapter 3.

5.2.2 Spatial properties of Data

In this section, each of three data and its individual spatial prosperities in different stages are plot. Some related statistical concepts, moments and statistical stationarity are briefly reviewed, for better illustration and explanation of water vapor variation in spatial field in this chapter, given in appendix A. Power spectrum analysis and spatial structure function has been employed to detect the spatial statistical properties of compositions of water vapour in this part. Power spectrum analysis and spatial structure function are described in detail in appendix B.

1) MERIS

Figure 5.4 to 5.6 depict the MERIS water vapor in three stages and their spatial variogram and spectrum. Spatial linear trend and stratification are jointly estimated with least squares fitting and then removed one by one; the dominants in residual signal could be regarded as turbulence term if neglecting the small stationary term. From this set of three figures, the stratification is much stronger than the spatial linear trend; the turbulence signal after removing both is about 1 mm or also.
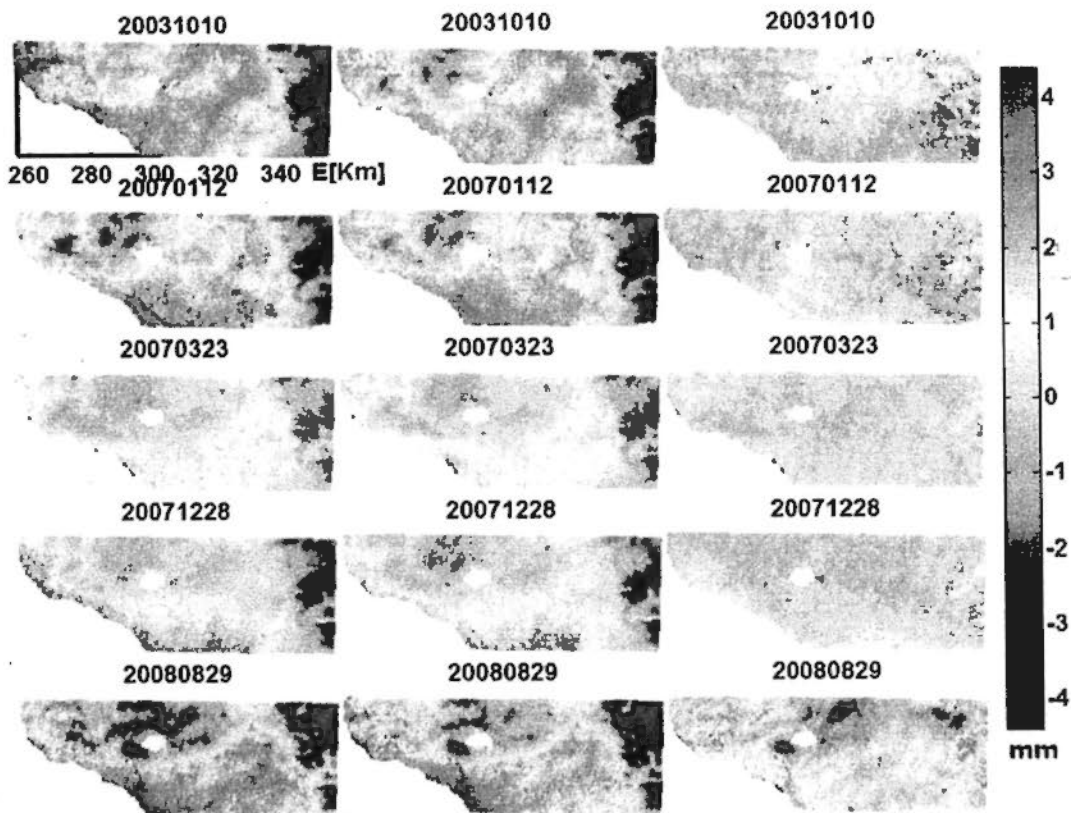
Figure 5.4 MERIS water vapour, all vapor maps with cloud free pixels larger than 40,000. For the arrangement of 15 sub-graphs, first column represent MERIS original water vapour. The second column represents water vapour after removal of spatial linear trend. And the third column represents water vapour after removal of both stratification and spatial linear trend. For better visualization, water vapour maps in same date under different stages are mapped after removal of individual average, keeping same color range (+/-4.2mm stands for difference between 5th and 95th percentile).

Figure 5.5 MERIS variograms in different stages, which of original water vapor is given in red, that of water vapor after removal of spatial linear trend is given in blue, and the turbulence signal is given in black.
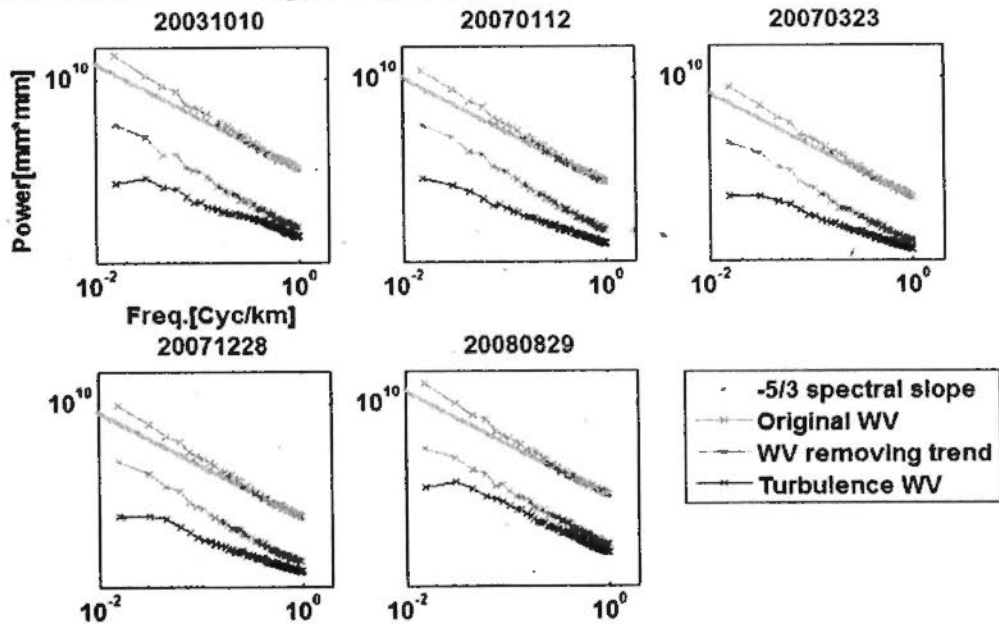
Figure 5.6 MERIS spectrum in different stages, which of original water vapor is given in red, that of water vapor after removal of spatial linear trend is given in blue, and the turbulence signal is given in black.

2) MM5 Water Vapor

Figure 5.7 to 5.9 depict five days cases of MM5 simulated water vapor and spatial properties with isotropic variogram and 1D rotated spectrum. The operations in this set of three figures are same as that in MERIS. The spatial linear trends in these figures are distinct within a larger coverage, and the strength of residual

106

turbulence signal close to that of MERIS. In spectrum curves, as similar as in that of MERIS, the spectrum at scale smaller than 10Km gradually converges at exponential spectral curve with power slope of -5/3.
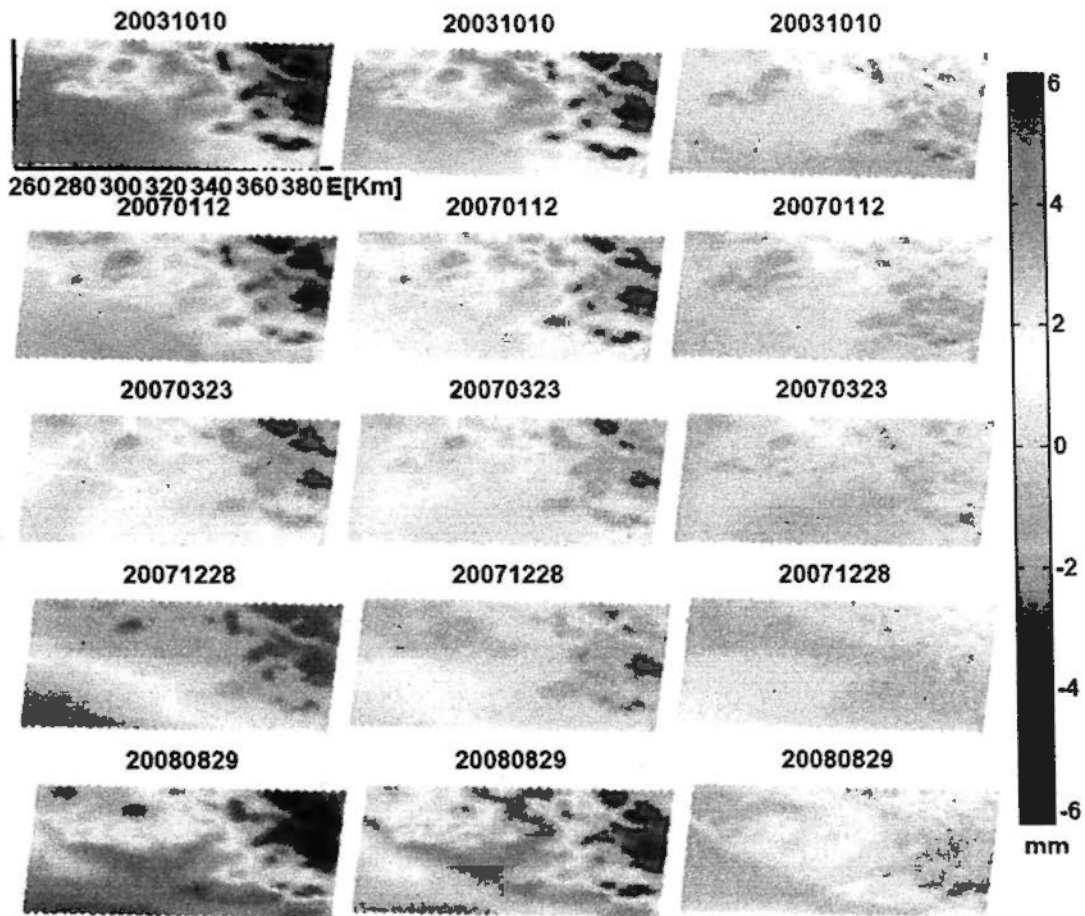
Figure 5.7 Water vapour maps simulated from MM5. Only 5 dates from total 32 ones are selected for comparable demonstration and spatial analysis. MM5 water vapour data are downwards arranged in column with increase of dates. Water vapour data are mapped in the same way of MERIS. The stratification was modeled with DEM after 2D median filtering with window of 7*7 and then removed.
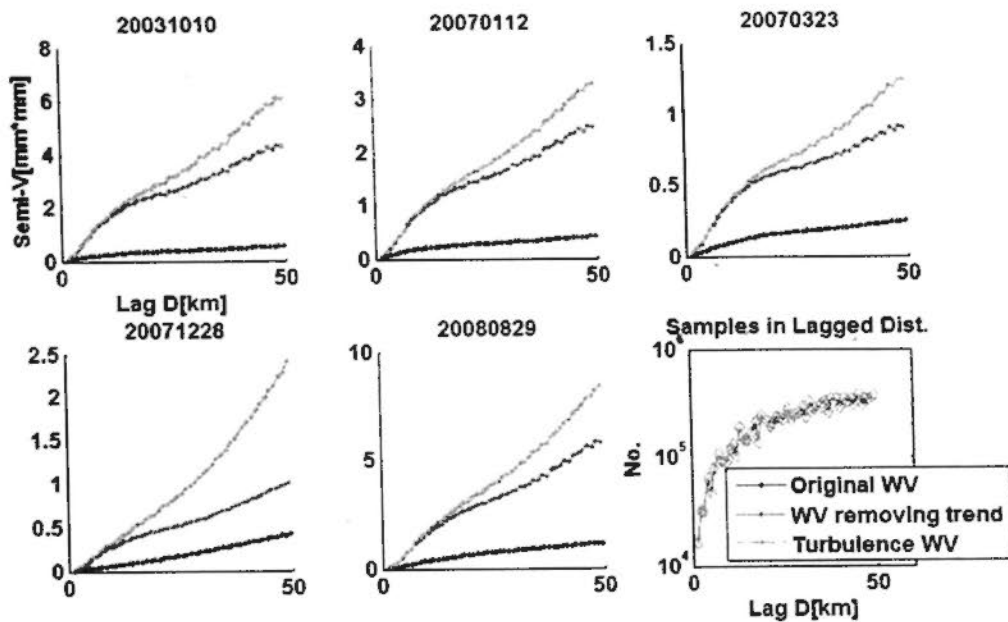
Figure 5.8 MM5 spatial variogram in different stages, which of original water vapor are given in red, that of water vapor after removal of spatial linear trend is given in blue, and the turbulence signal is given in black. The stratification was modeled with DEM after 2D median filtering with window of 7*7 and then removed.
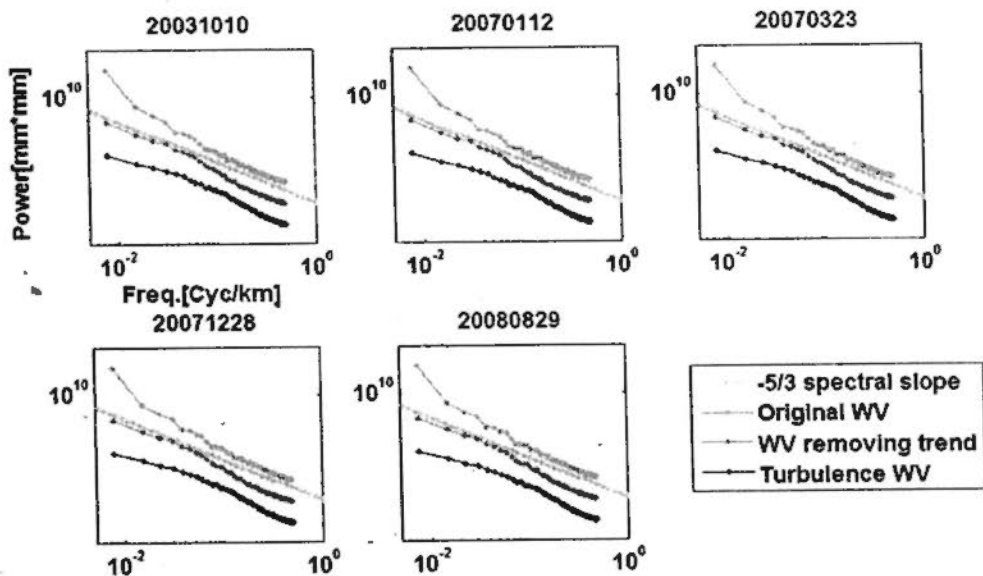
Figure 5.9 MM5 spectrums in different stages, which of original water vapor are given in red, that of water vapor after removal of spatial linear trend is given in blue, and the turbulence signal is given in black. The stratification was modeled with DEM after 2D median filtering with window of 7*7 and then removed.

3) Water Vapor from APS

Figure 5.10 to 5.12 depict water vapor maps from SAR APS and its spatial properties in different stages. From this set of three figures, since the nominal terms

108

of spatial linear trends in differential maps are cancelled out, the signal strength in APS at large scales is much smaller than that of MERIS or MM5. The exceptions are signals on three dates 20031010, 20070112 and 20070323 that remarkable spatial artifacts due to inaccuracy of satellite orbits are existent. While for all five cases, the stratification terms in these APS maps are extremely tiny, i.e., the variograms and spectrums of turbulence signal with or without stratification term nearly coincide well between each other.
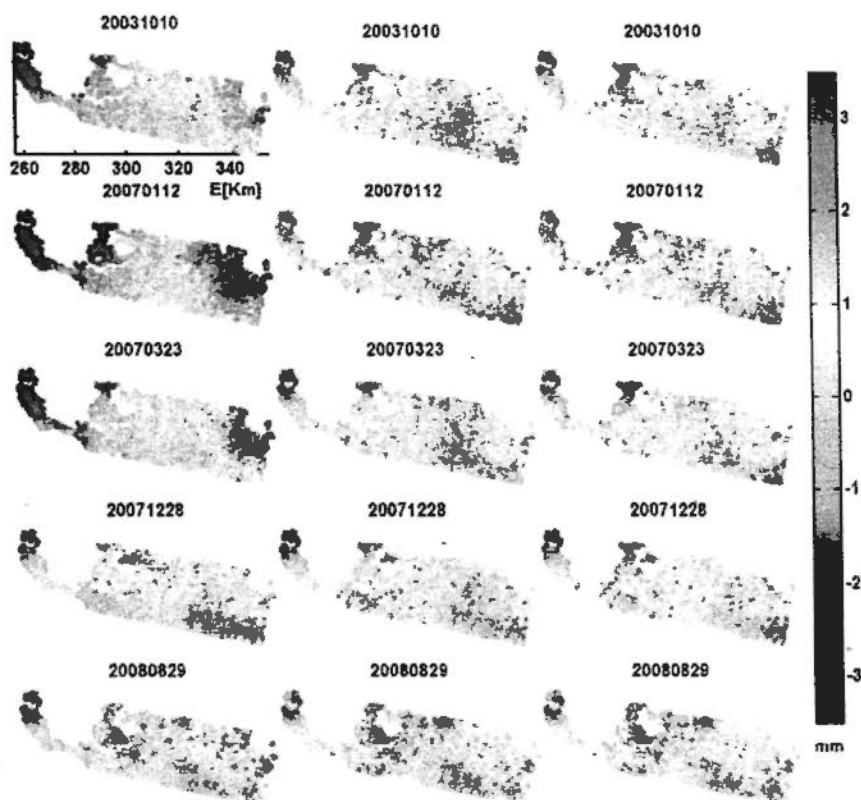
Figure 5.10 APS water vapour maps from ENVISAT ASAR T351 around Rome, transferred from phase in to integrated water vapour in mm. SAR APS in increasing date are arranged as that of MERIS. Water vapour data are mapped in the same way of MERIS. Among these, APS of master image is date of 20071019.
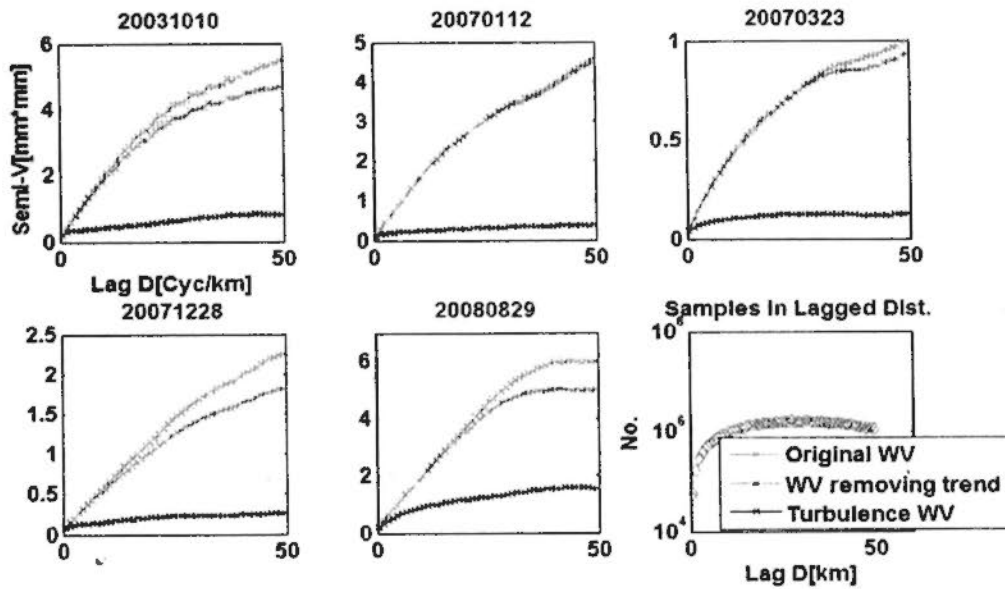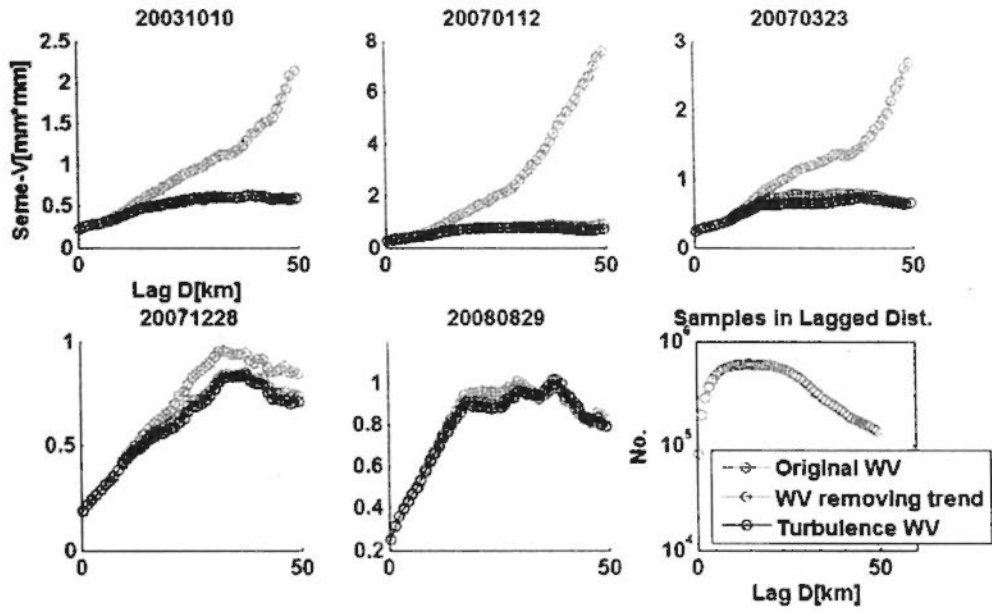
Figure 5.11 APS Variogram in different stages, which of original water vapor is given in red, that of water vapor after removal of spatial linear trend is given in blue, and the turbulence signal is given in black.
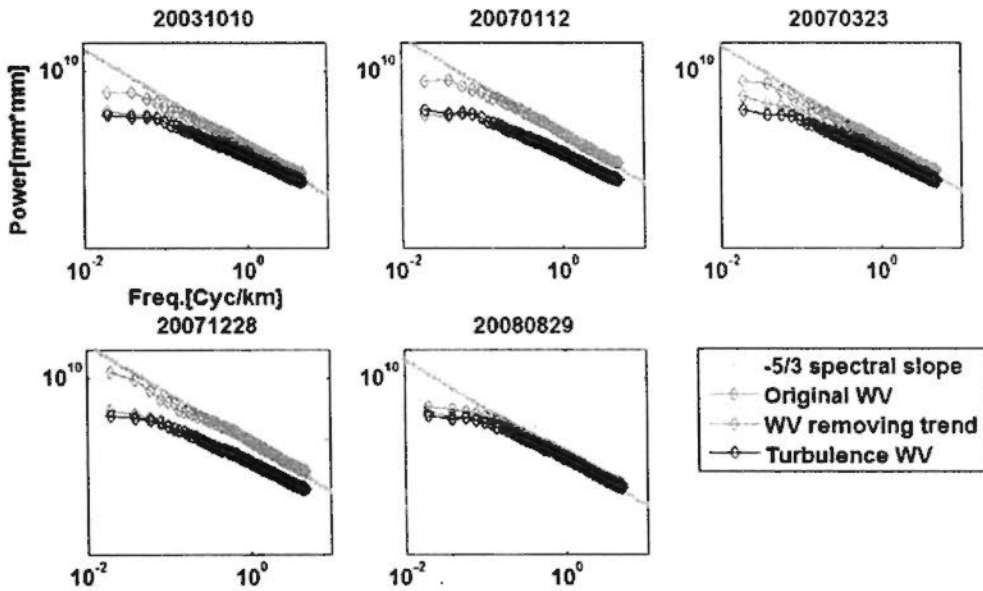
Figure 5.12 APS spectrum in different stages, which of original water vapor is given in red, that of water vapor after removal of spatial linear trend is given in blue, and the turbulence signal is given in black.

5.3 Spatial stochasticity of Differential Water vapor

As studied on water vapor signal compositions in Chapter 3, the spatial temporal law of different water vapor signals should also be distinguished and

individually observed. The most important among all are height dependent stratification term and spatially correlated mixing turbulence.

After the successful separation of four basic signal of water vapour, we do spectral analysis for integrated water vapor and also for each basic signal. Turbulence, which is varied strongly both in space and time, are analyzed in detail. For the detail that how to decompose water vapor into spectra in different temporal frequency and the method to revert spatial (2D and 1D) spectrum of turbulence term, the readers can refer to Chapter 3.

5.3.1 Implementation of Differential Mode

With the water vapor components model described in chapter 3, atmospheric water vapor in SAR APS can be regarded as superimposition of four compositions: spatial linear plane, height dependent stratification, mixing turbulence and ground feature related term. In addition, APS derived from PS-InSAR are differential measurements in an interferometric way and relative to a master image, while water vapor estimated with non-interferometric techniques (such as MERIS, MM5, etc.) are spatially and temporally absolute measurements. To demonstrate reliable and comparable results, we must resolve the characteristics difference from different datasets.

Then in this chapter, as similar with the approach in chapter 4, we transform the absolute water vapor maps into differential values, and then to compare them in differential domain. Since the original APS master chosen in PS-InSAR processing was not covered by the external data series in MM5 and MERIS, then a differential operation between corresponding synchronized pairs as well as SAR APS water vapor were implemented. In this case, the differential operation cancelled out the common unknown atmospheric water vapor of the original master date and then comparable values are kept consistently well with physical meanings.

Besides the above unification of temporal reference four additional operations are implemented to enable the two datasets into comparable values. 1) The link

between SAR APS phase and IWV should be built for comparison. A Mapping Function of incidence angle must be accounted for to transform radar signal delay in two-ways at an incidence angle into IWV in one-way vertical direction (Cheng 2009). 2) Geo-code SAR APS into a common geographic system, i.e. WGS84 grid. 3) Spatial linear trends should be carefully considered and removed from APS, if required. 4) Removal of mean values in space for Absolute Water Vapor. Since SAR APS are spatial differential signals, in order to keep consistency, spatial averages of absolute water vapor maps are required to remove to cancel out the unknown bias.

5.3.2 Spatial and temporal data synchronization

After the differential mode (described in section 5.3.1) implemented on water vapour data, steps for spatial and temporal synchronization are taken before spatial analysis. Spatially, in order to keep the analyzed data with same geographical sampling, we segmented MM5 and MERIS images from original coverage by APS spatial samples, and then resampled both data into APS sample points. Isolated APS clusters in the North West are also removed to avoid instability. A nearest neighbor interpolation has been performed to generate resampled data with tens to hundreds of meters resolution from original 1 km spatial resolution. No extrapolation is required because that coverage of MM5 and MERIS totally contains all SAR APS samples, as shown in figure 5.1. All interpolated samples with non null values are taken into the variogram calculation. Before spectrum calculation, one rectangular grid centered at and bordered by APS scatter points with resolution of 0.2 km has been predefined. Valid values on the grid have been searched within the nearest neighbors from sparse APS (or resampled MERIS, MM5) points within 1.2km and resampled by triangle-based linear interpolation. Spectrums are obtained based on valid values of generated grid.

Temporally, SAR APS are processed from ENVISAT ASAR descending track 351 in Rome with the acquisition time at UTC 9:28 a.m. MERIS water vapour images are temporally simultaneous with ASAR images with the passing time at

112

UTC 9:28 a.m.(sensors on same platform) MM5 simulated water vapour images are modeled from UTC 0h to 24h. The MM5 simulation provides the temporally evaluative (e.g hourly or half hourly) atmospheric parameters, but up to now it's quite challenging to generate desired atmospheric product exactly for given epoch. Under this limitation, we take the MM5 data at UTC 9h as substitute of UTC 9.5h in our experiment. The influence of temporal gap of 0.5 hour would be neglected in this section. Besides keeping the acquisition epochs close to that of each other, more important what we do is that only water vapour data at same date and under qualified weather conditions (cloud free for MERIS) are selected for post processing and analyzing. Synchronized and resampled water vapour of MERIS, MM5 and SAR APS are depicted in figure 5.13.
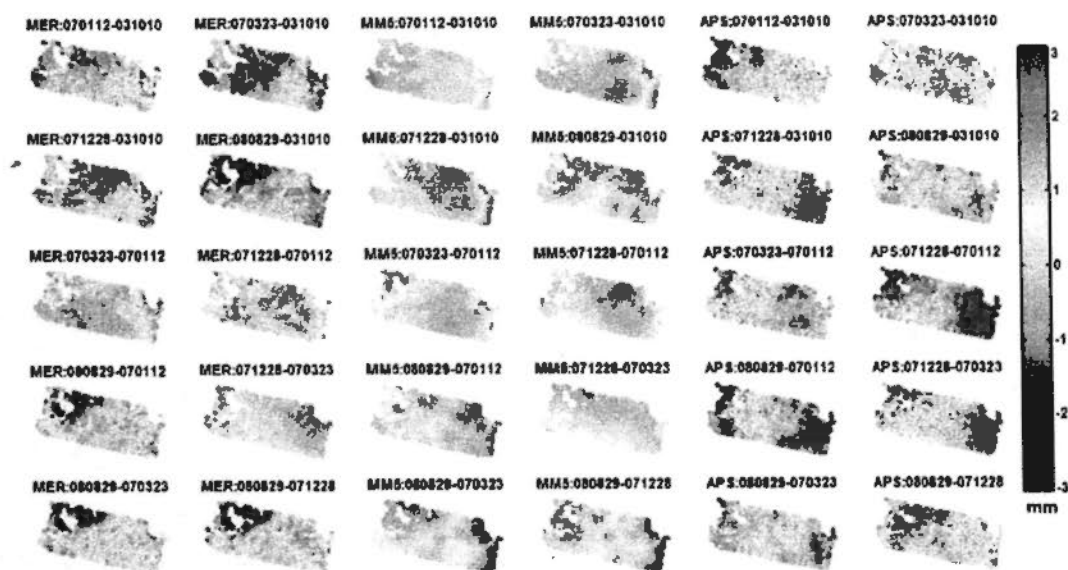
Figure 5.13 Original Differential Water vapor, pairs are randomly combined from 5 synchronous days. For the arrangement of sub-graphs, first two columns represent MERIS water vapour; the second two columns represent MM5 water vapor; the third two columns represent SAR APS interpreted water vapor. 10 differential maps in each set are column-wisely arranged in the same sequential. For better visualization purpose, the individual average of MERIS and MM5 are cancelled, and then the variations of water vapor are saturated to +/-3.0 mm.

In figure 5.13, original differential water vapor maps are plotted for demonstration, 10 differential maps in each dataset are column-wisely arranged in the same sequential and the variations of water vapor are saturated to +/-3.0 mm.

113

From the figure, MERIS and MM5 observes similar spatial pattern, while SAR APS behaves finer spatial disturbulence with a strong spatial linear trend.
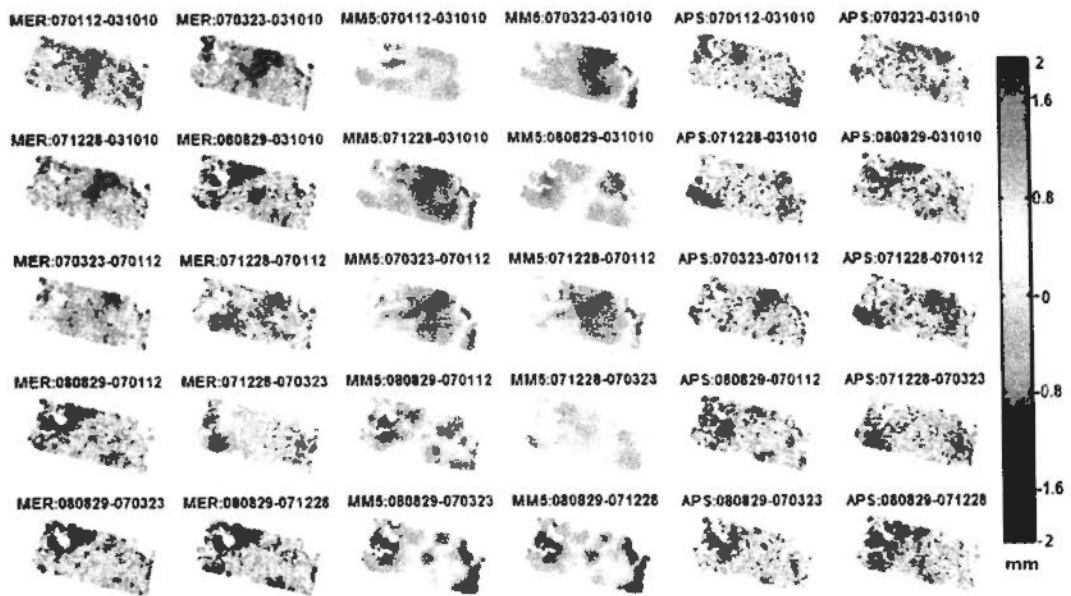
Figure 5.14 Differential Water Vapor with removal of spatial linear trend, combined pairs and arrangement of sub-graphs, are as same as figure 14. For better visualization purpose, the variations of water vapor are saturated to +/-2.0 mm.

After removal of spatial linear trend and stratification, we plot the differential water vapor turbulence from three dataset in figure 5.14. In this figure, MM5 behaves smoothly, while the MERIS and APS water vapour presents similar roughness (strength of disturbulence.) Overall, the general patterns are in some extent coherent with each other, while the details are analyzed in next sub-section.

5.3.3 Omni-directional analysis

In this Omni-directional analysis, we calculate the spatial spectra and variograms in two dimensional and average those into direction-independent values, i.e. averaging in rotated all directions. In this chapter, MERIS, MM5 and SAR APS have all provided the spatial variation and structure as map-based water vapour. For comparatively demonstrate the spatial stochastic properties, spatial and temporal synchronized data from last section are taken for advanced spatial statistical analysis. Figure 5.15 describes the spatial variograms from differential water vapour data after removing of spatial linear trend, which are averaged from various directions based on

isotropic assumption. Spatial linear trend are removed to leave out possible artificial errors and enable water vapor signals statistically stationary.
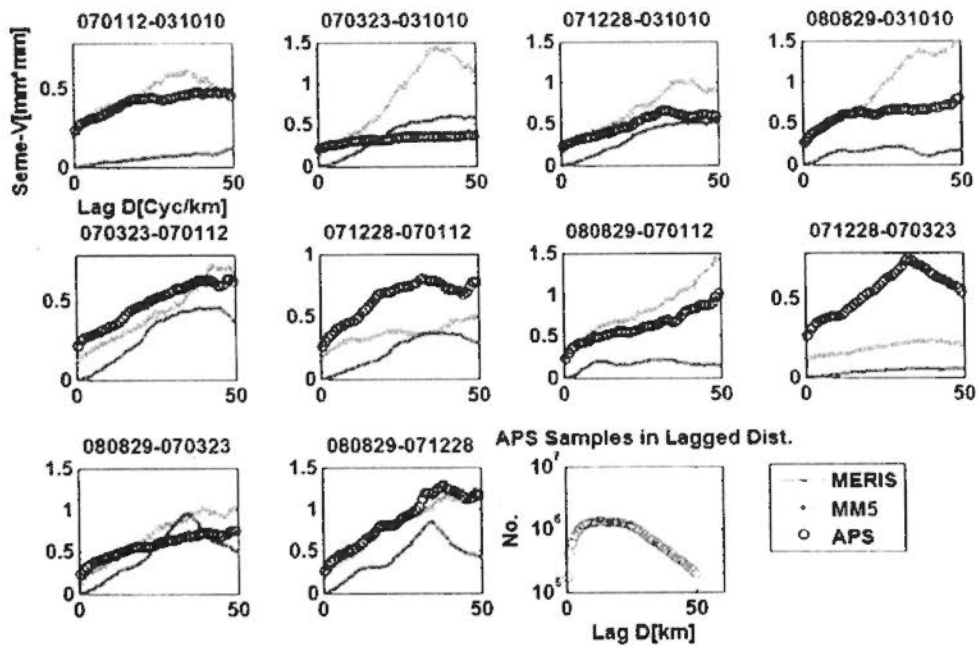
Figure 5.15 Semi-Variance of differential water vapor after removal of spatial linear trend from three dataset.

In order to derive their spatial spectrum, as briefly described in last subsection, a regular grid with 0.2 km resolution are produced from original sparse water vapour of all datasets. With the FFT transformation into spatial frequency domain and averaging of signal power spectrum from two dimensional into one dimensional, one dimensional spatial Power Spectrum Density (PSD) of water vapour for MERIS, MM5 and SAR APS can be derived. Figure 5.16 plot derived Power Spectral Density from all three data source, typical power spectral slope of -5/3 (Hanssen 2001) for water vapour have been plot as reference together with derived PSD.
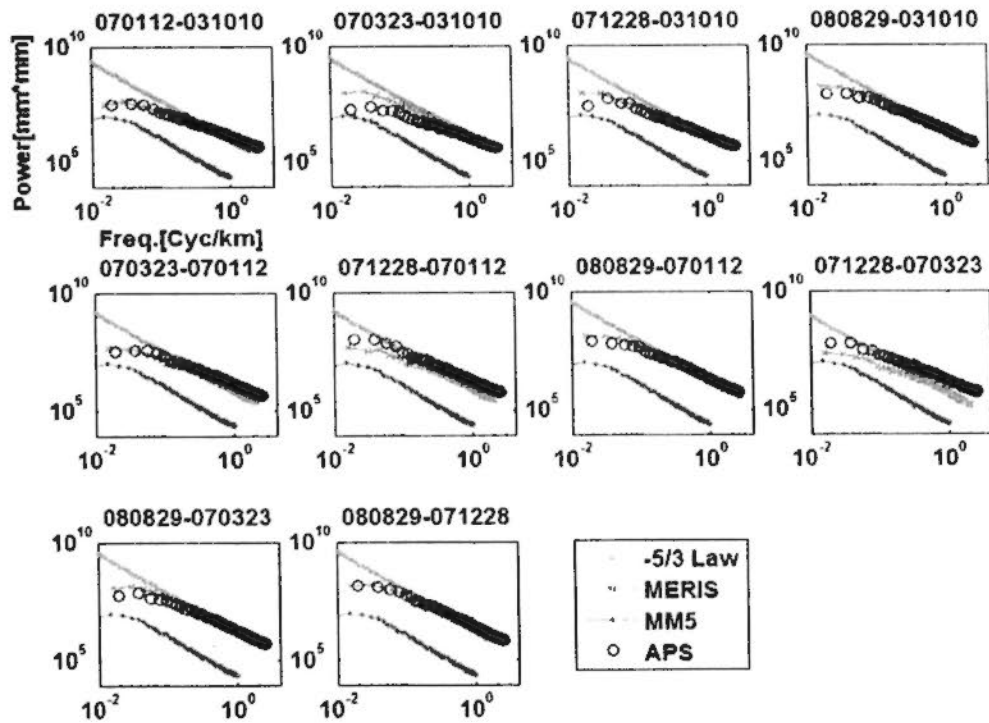
Figure 5.16 Spectrum of differential water vapor after removal of spatial linear trend from three dataset.

After removal of spatial linear trend, we obtained the variogram curves as figure 5.15 and spectra curves as figure 5.16. Following laws can be perceived from 10 pairs of cases from three dataset.

1) After removal of spatial linear trend, the isotropic variograms from MERIS close to that from SAR APS in most cases. The variogram curves between MERIS and MM5 have much coherence, though smaller (larger or smaller case by case) differences of semi-variance between MERIS and APS are existent.

2) After the removal of spatial liner trend, semi-variance of differential water vapor for all three data in space varies from 0.5 mm^2 to 1.5 mm^2. The number of such semi-variance is not so much in water vapor study, but it could be strongly influential if regarded as atmospheric delay (from 20 mm^2 to more than 50mm^2).

3) MM5 shows lower variogram, with smallest nugget and smallest sill compared to other two data. This means variation of MM5 water vapor is smooth, which is determined by 1km resolution of simulation. While MERIS and SAR APS

116

water vapor data provide stronger spatial variations in smaller scale. This could be significant in fine scale meteorological applications or atmospheric studies.

4) Spectra from MERIS are highly coherent with that form SAR APS. On the contrary, MM5 spectra are much lower than that from SAR APS. The signal power spectra for MERIS and SAR APS have wider spectral window, extended to scale smaller than 1km. The information provided by spectra in figure 5.16 additionally support the evidence founded from variograms in figure 5.15. Generally, MM5 spectra follow the Kolmogorov turbulence theory as spectral slope of -5/3, while spectral slopes from MERIS and SAR APS water vapor data (about -1.6) are lower than this number.

5.3.4 Directional analysis

Anisotropic properties of atmospheric signals have long been regarded. Hanssen firstly used Radon transform to examine the anisotropy of atmospheric signatures in SAR interferograms in Netherland (Hanssen 1998). Ding used radon transformations to study the anisotropy of atmospheric signatures in four SAR interferograms over shanghai (Ding 2008). Such anisotropic properties of water vapor have much significance in geophysical parameter retrieval, e.g. ground deformation.

Knospe fits anisotropic variogram model employing Matérn- and Bessel-family correlation functions to represent complex DInSAR covariance structures, and use anisotropic covariance information to weight DInSAR measurements, achieving improvement of accuracy of geophysical parameter estimations (Knospe 2010). The directional statistical properties are applied in anisotropic modeling of atmospheric phase in the sparse-grid point-target DInSAR applications. An improvement in the performances of kriging reconstruction with sufficient sampling densities is observed (Refice 2011).

To detect the possible anisotropic characteristics of water vapour in our experimental area, in this section, directional variograms in evenly separated angles calculated from synchronized water vapor data (from SAR APS, MERIS, MM5) in

differential mode. Then isotropic spatial structures from different water vapor data are compared.
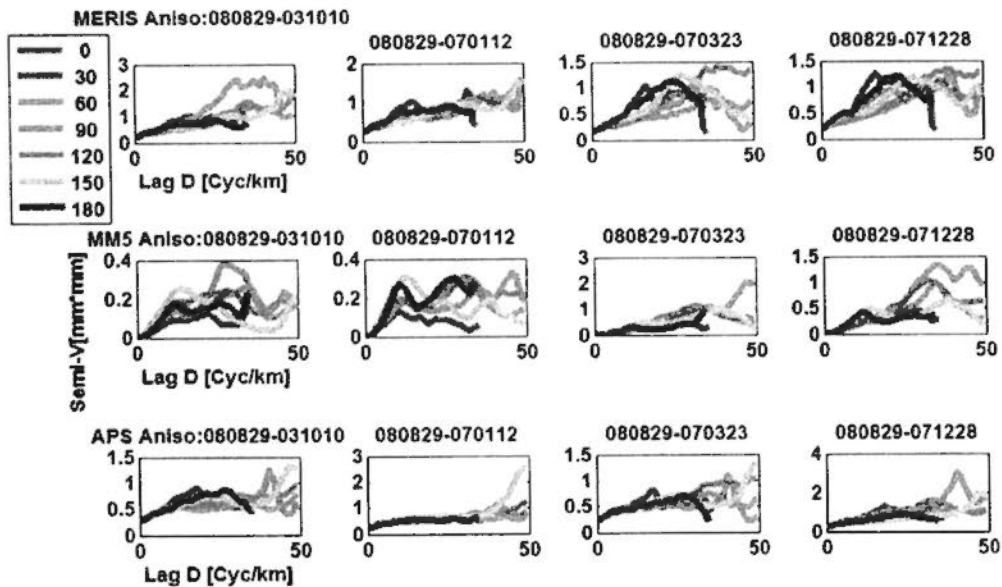
Figure 5.17 Directional variogram from spatially interpolated (overlapping MERIS and MM5 on APS) and temporally synchronized MERIS, MM5 and SAR APS differential water vapour after removal of spatial linear trend. Semi-variograms at 7 directions from 0 to 180 degrees with averaging interval of 30 degrees are calculated.

In figure 5.17, we plot the directional variogram of water vapor from the water vapour after removal of spatial linear trend, from three kinds of synchronized data. Spatial linear trend are removed to leave out possible artificial errors and enable water vapor signals statistically stationary. The 4 cases from 10 are selected, which has strong intensity of atmospheric signal and directional effect. Several laws could be observed from the figure:

1) Isotropic assumption generally holds in spatial scales small than 30 km. In figure 5,17, except MERIS 080829-031010, the variograms in different directions under small spatial scale are overlapping on each other;

2) In spatial scale larger than 30 km, anisotropic properties shall be carefully considered and modeled. E.g. direction of 60, 150 deg. (0 degree as eastward) larger than 30 km are stronger than other directions in figure 5.17, the difference of variogram could be as high as $1\sim3$ mm^2.

3) MERIS, in this thesis, with spatial resolution of 360m*250m, providing highly similar subtle change of anisotropic variogram with that for APS in most cases. While MM5, with forever available and regular sampling but lower resolution, provides smooth and stable anisotropy prosperities in all scales. The coherence of their variogram performance in different directions at different scales are moderate, the reasons of difference need more cases for checking.

5.4 Pseudo absolute Water Vapor

In this pseudo absolute mode, our purpose is to recover the differential SAR APS water vapor by water vapor MERIS maps at SAR master date. The recovered absolute APS water vapors are intended to compare with MERIS and MM5. Since MERIS and SAR sensors are both equipped and simultaneously operated on ENVISAT satellite. MERIS water vapor images with could mask products can possibly provide spatially lost information of water vapor at SAR master acquisition epochs. With this idea, temporal ambiguity of APS water vapor could be partially recovered. The figure 5.18 and 5.19 shows our approach and recovered water vapor maps. From figure 5.18(a), MERIS water vapor values at 9:30am on 20071019 after cloud mask are 2D linearly interpolated, 5*5 filtered and resampled into water vapor of APS coverage, as APS water vapor of mater reference, shown in figure 5.18(d)
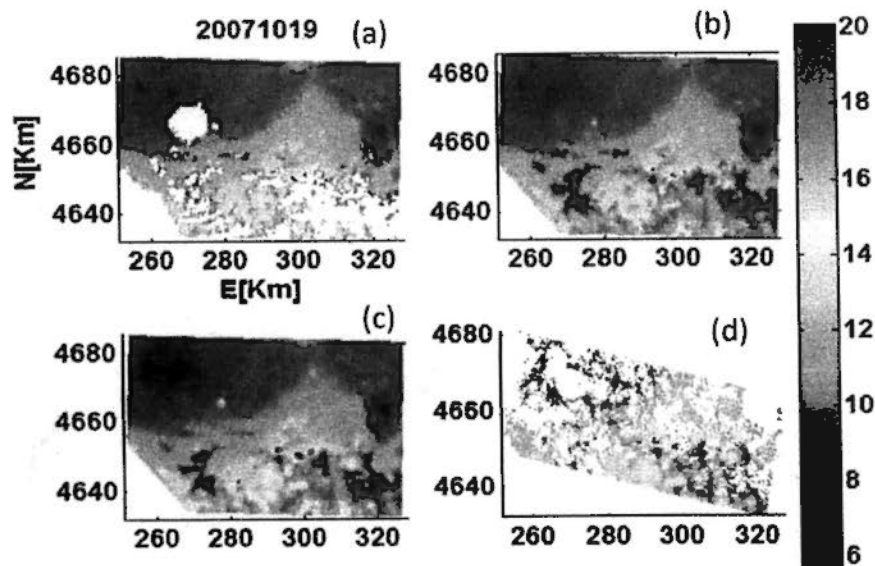
Figure 5.18 The water vapor at 9:30 am on 20071019 (epoch of SAR master) from MERIS data. (a): original MERIS water vapor map, pixel are valued with nana under cloud mask. (b): Gridded map with valid pixels; (c) Filtered gridded map by median filtering with window of 5*5; (d): The interpolated water vapor values overlapped with SAR permanent scatterers. Unit of water vapor is mm.
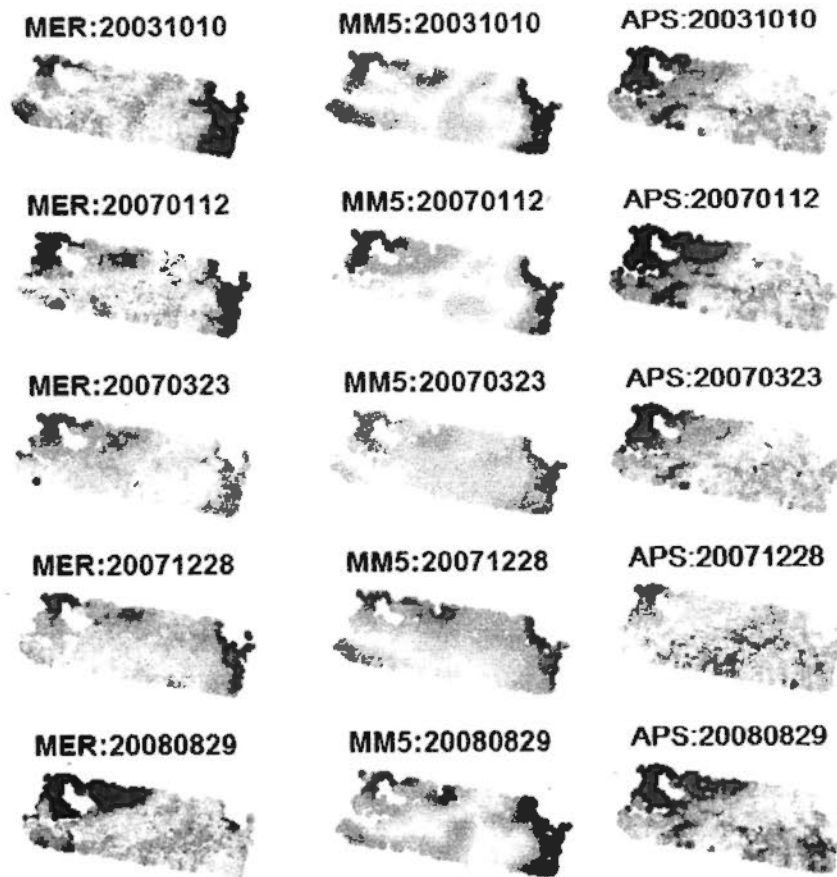
Figure 5.19 Synchronous water vapor values in absolute mode for three data source. Water vapor values from SAR APS are recovered by adding absolute water vapor at master epoch on differential APS water vapor. For visualization, the variation range of MERIS and MM5 was saturated by +/-3mm. The median value of each pair was extracted for comparison and neglected in vapor plotting. APS water vapor varied from 4 to 18mm with full color scale.

In figure 5.19, the recovered absolute SAR APS water vapor maps according to above approach as well as original MERIS, MM5 water vapor data on synchronous dates are demonstrated. As shown in figure 5.19, except the date 20080829, the magnitude and spatial pattern of recovered SAR APS on other four cases has certain similarity and correlation with synchronous MERIS and MM5 water vapor maps. We acknowledge that this similarity between SAR and non SAR are not as high as that between MERIS and MM5, but regional inhomogeneity still can be perceived from

synchronized maps. The figure can provide more confidence on recovery of absolute water vapor from differential APS. as promising and useful technique to lead SAR APS water vapor maps for meteorological applications.
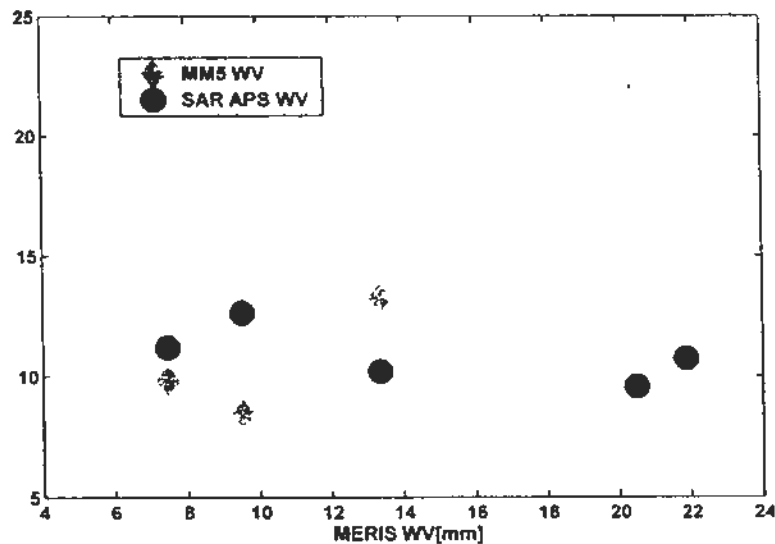
Figure 5.20 Median values of absolute water vapor maps for MERIS vs. MM5, and MERIS vs. APS.

Figure 5.20 plots the median of absolute water vapor maps for MM5. SAR APS and MERIS. A good positively linear coherence from scatter points can be observed between MERIS and MM5. While median from recovered APS are not genuine values. dependent on the average of water vapor in MERIS adopted as master of SAR data.

As illustrated in water vapor component model in section 3.2. The lost information in differential water vapor from SAR are not only including temporal reference, but also including nominal terms of spatial linear trend, stratification and stationary term. So water vapor at SAR mater epoch alone is not sufficient to recover the genuine absolute water vapor for each SAR image.

More robust way is to retrieve nominal terms (e.g. linear trend in spatial low frequency) from other external data (e.g. MERSI. or simulated models) for SAR imagery, and then to recover original nominal components which are lost in differential APS products. As introduced in section 3.4, when retrieving and compensating of spatial linear trend, DEM data and its modeling of stratification

121

with joint least squares fitting to avoid mixing is also required if local elevation has spatial distinct pattern.

5.5 Conclusions

Based on proposed water vapor model in chapter 3, mixture of spatial linear trend and stratification can be better discriminated, and the target of spatial analysis is water vapor components, instead of total water vapor. Furthermore, differential and pseudo absolute implementations were implemented to compare the spatial stochasticity between APS and synchronous absolute water vapor maps from MERIS and MM5. With these two operations, new water vapor retrieval products- water vapor from APS can then be linked to the conventional water vapor products, i.e. MERIS, modeled water vapor.

More important, we use power spectrum and semi-Variogram to represent the spatial stochastic properties of water vapor components based on overlapped and synchronous data, Water Vapor from MERIS, MM5 and APS. Spatial spectrum and variogram (structure function) with isotropic assumption is derived to measure the spatial stochastic law of water vapour, for total noise and only turbulence. Following this, we detect the anisotropic characteristics of water vapour by calculate the directional variogram with even spaced direction degrees.

The main highlighted points in the experimental analysis we draw include following:

a) From the derived spatial structure function and spectrum of total water vapour and assumed turbulence based on isotropic assumption, APS water vapor usually has stronger spatial pattern (trend), with removal of such spatial pattern, the magnitude of variance of water vapor are approaching to MERIS and MM5.

b) Overall, in the assumed turbulence term, APS is overestimated than MERIS and MM5 in variogram, while compare to MM5, MERIS are more close to

APS in the performance of spatial isotropic variograms.

c) Based on anisotropic assumption, the derivation of directional variograms for water vapour turbulence provides some new insight of spatial variogram in large scale. In spatial scale of 30 Km or more, anisotropic properties should be considered, compared to MERIS, then MM5 can be advantageous to help APS.

The above water vapour signal characteristics in different perspectives being deeply studied have much significance. Only sound analysis of water vapour data and spatial/temporal varying law are conducted, the model of water vapor in different components for mitigation on InSAR could be accurately built. Water vapour spectral behavior studied in this research would be significant to construction of fine scale (equal or smaller than 1km) 2D water vapour field, and also understanding of spatial stochastic law toward the final solution of InSAR atmospheric artificial fringes. The research here also provide possible insight for satellite based microwave atmospheric delay correction, e.g., Point stand-along GPS positioning, costal satellite laser almery.

Chapter 6 Conclusion and Recommendation

Comparative study of water vapor between Interferometric SAR images and synchronized data in this thesis serves following two motivations: 1) to study the atmospheric effect in SAR interferometry and it's compensating. 2) to demonstrate the preferential capability of water vapor map from Interferometric Radar in spatial domain.

6.1 Conclusions

1) Reasonable differentiation of Water vapour components

We in this paper proposed water vapor component model to serve for comparative analysis between SAR APS and absolute water vapor data. The Proposed model, can applicable in both SAR interferometric water vapor and independent WV data, was validated with paramount amount MM5 maps with 1km resolution and 1 hour interval.

A) The spatial temporal decorrelation of water vapor turbulence signal has been studied with MM5 IWV maps using frequency spectrum and correlation analysis. The result shows that 1~2 hour of turbulence in all scales, and even 3~4 hour of large scale turbulence are highly correlated.

B) Stationary term and mixing turbulence term have been distinguished with two approaches-temporal periodic averaging and spatial spectral filter-based on spatial and temporal difference of characteristics between both terms.

C) The differentiating between spatial linear trend and stratification shall be careful if the topography of experimental area has some extent of spatial trend. Joint parameter retrieval with least squares fitting is recommended instead of the common sequential separation ways in this case.

2) Point-based Comparison

The stratification effect of APS with a mixture of turbulence as well as spatial linear trend is analyzed and two comparison modes between GPS and APS are implemented for the first time. With height determined grouped APS, after removal of the spatial linear trend and neglecting mixed turbulence at lower heights, the stratification ratio of APS derived in this experiment coincides well with that of GPS.

A) GPS ZWD is directly proved to be comparable with SAR APS in differential mode. The slopes from both correlate with a coefficient higher than 0.8 with bias (GPS-APS) of 3.4 mm/Km as well as a STD of difference of 7.7 mm/Km in the ascending case in the differential comparison. Though with more noise and a larger STD of difference, slopes for the descending case still gain correlation with coefficients of 0.74.

B) Pseudo-absolute comparison results are also provided. Comparatively, pseudo-absolute comparison is only approximately implemented, which inevitably brings implementation errors. The agreement of atmospheric delay in this mode was slightly worse than that in differential mode, but it still provides an alternative vision in comparison.

3) Spatial stochasticity of water vapor based on map-based comparison

We use power spectrum and semi-variogram to represent the spatial stochastic properties of water vapor components based on overlapped and synchronous data, water vapor from MERIS, MM5 and APS. Spatial spectrum and variogram (structure function) with isotropic assumption is derived to measure the spatial stochastic law of water vapour, for both total signal and turbulence only. Following this, we detect the anisotropic characteristics of water vapour by calculate the directional variogram with even spaced direction degrees. The main summarized points in this part are as following.

A) From the derived spatial structure function and spectrum of total water vapour and assumed turbulence based on isotropic assumption, APS water vapor

usually has stronger spatial pattern (trend), with removal of such spatial pattern, the magnitude of variance of water vapor are approaching to MERIS and MM5.

B) Overall, in the assumed turbulence term, APS is overestimated than MERIS and MM5 in variogram, while compare to MM5, MERIS are more close to APS in the performance of spatial isotropic variograms.

C) Based on anisotropic assumption, the derivation of directional variograms for water vapour turbulence provides some new insight of spatial variogram in large scale. In spatial scale of 30 Km or more, anisotropic properties should be considered, compared to MERIS, then MM5 can be advantageous to help APS.

6.2 Contributions of this research

The Innovation and contribution in this thesis research are as following:

1) *Exploratory study in a in a comparative perspective for water vapor from Permanent Scatters Radar Interferometry and synchronous data set.*

a) The research perspective is innovative among similar studies in this topic. In our research, credible SAR APS in form of transformed water vapor is compared with external synchronized data to study the compensating feasibility of InSAR atmospheric effect. b) The research data supporting this study is innovative and comprehensive. More than 100 APS maps from 3 tracks, 777 MM5 water vapor maps, 25 MERIS images and synchronous GPS campaign data were collected for the research analysis. c) Results demonstrated in this research also point out newly promising insight. Water vapor from InSAR presents unparalleled superiority with its highest spatial scale, e.g. tens of meters, which would be highly valuable in regional water vapor study or meteorological service.

2) *Precision of water vapor measurements from SAR APS and the statistical law of water vapor maps from SAR APS are studied using comparison with synchronous data.*

A) Point-based comparison results provide us the individual precision of water vapor from APS. It then implies the potential and limitation of atmospheric compensating of SAR interferometric measurements with external water vapor data. B) Map-based comparison results provide us the coherence and difference of spatial temporal statistical characteristics of water vapor field from multiple sources. This would provide valuable predictions in water vapor mutual calibration or data synergy, especially when employed data have spatial resolution discrepancy or temporal gaps.

3) A logical strategy of differentiation of water vapor components and implementations for comparison were introduced as useful reference in atmospheric probing in interferometric SAR.

We in this paper firstly proposed water vapor component model to serve for comparative analysis between differential water vapor signal from SAR APS and absolute water vapor. Based on this model, components in total water vapor can be discriminated and the analyzing target can be focused on each component instead of mixed signal.

The proposed rational strategy to differentiating of water vapor components and the implementation of comparison way (differential mode and pseudo-absolute comparison) between SAR and non SAR data can be taken as valuable reference in technical operations of atmospheric compensating in SAR interferometry.

6.3 Recommendations on future work

In the thesis, some aspects are covered, e.g. water vapor component model, water vapor signal decomposition, data comparison between GPS and InSAR, spatial & temporal statistical analysis. But we have to objectively confess, the following aspects have been only partly or weakly involved in this thesis up to now. These items are still open for deeper investigation in future research, which would be significant in the InSAR atmospheric study for geophysical applications.

As a summary, the work continuing to our results-water vapor study from Interferometric SAR images and synchronized data-includes following aspects.

1) Ground feature related signal validation

Though ground feature related water vapor signal are demonstrated to be slightly existent, but the exact influence on InSAR have not been quantitavely given, and how to model such water vapor signal composition still need more work. The external validation of ground feature related stationary term is suggested to be taken using fine scale Land use classification map or coinstantaneous high resolution Remote Sensing Images, e.g. as a further study, to validate the stationary term detected in this chapter with MM5 IWV, coinstantaneous 1Km MODIS multispectral images in cloud free conditions can be collected to obtain updated reliable ground feature classification map and to detect possible correlation between stationary water vapor signals and following special features: smaller water body, vegetation area, shaded area in large slopes etc.

2) GPS data is valuable to provide point-based atmospheric information. But such GPS data only provides sparse samples for atmospheric compensating in map-based SAR interferograms; The performance of mitigation using GPS data only still depends on other factors: 1) Strategy and accuracy of zenith delay retrieved from GPS, 2) Spatial separation and distribution of GPS stations, 3) Interpolation model for predicting every interferometric spatial pixel from known GPS locations, and 4) Other related factors sensitive to atmospheric effect on InSAR e.g., local topography, local ground feature, ionospheric activity (intensity and abnormity).

3) The understanding of water vapour spatial temporal characteristics in different scale and for each component still requires more effort to improve. Water vapour behavior described by variogram, spectrum or decorrelation would be significant to predict that with which data atmospheric signal component can be mitigated and in which extent such mitigation can be achieved. Though important in

practical applications, this kind of advises on atmospheric mitigation strategy are not given in this thesis,

4) Recovery of absolute water vapor form SAR differential APS is promising in meteorological application in the future. As illustrated in water vapor component model in section 3.2. The lost information in differential water vapor from SAR are not only including temporal reference, but also including nominal terms of spatial linear trend, stratification and stationary term. So water vapor at SAR mater epoch alone is not sufficient to recover the genuine absolute water vapor for each SAR image. More robust way is to retrieve nominal terms (e.g. linear trend in spatial low frequency) from other external data (e.g. MERSI, or simulated models) for SAR imagery, and then to recover original nominal components which are lost in differential APS products.

InSAR atmospheric effect and its compensating is a radical problem in this field and an essential purpose of this research. As far as our understanding, the following two aspects related to our work and serving the same purpose can in significant in this field. 1) Coupling of deterministic physical model or simplified statistical model with one or two water vapor data, as shown in GTTM model with GPS data (Li, Z.H. 2006) and 'frozen flow' GPS model (Onn 2006). Better understanding of turbulence signal in smaller scale (e.g. less than 10 Km) from statistical modeling with current available water vapor data (e.g. fine scale MM5) still have significance in this field. 2) Water vapor observations shall be closely working together with typical advanced long time series InSAR techniques, e.g. PSInSAR, SBAS, etc. though the former one provide more information, while the latter one is rather robust and quite applicable in practical applications.

Appendix A Review of geo-statistics of water vapor

A.1 Moments in geo-statistics

1) Expectation - First-order moment

Giving random variable $\varphi(X)$ with probability density function of $pdf(\varphi)$ at geospatial location X in an image (x, y), the expectation of this spatial random variable $\varphi(X)$ is as follows:

$$E\{\varphi(X)\} = \mu(X) = \int_{-\infty}^{\infty} \varphi \cdot pdf(\varphi) \cdot dx \qquad (A.1)$$

The expectation of random variable is also called first order moment.

2) Variance - First Second-order moment

The dispersion of random variable on expectation value is described by the second-order moments. Three second-order moments are the variance, the covariance and the structure function or variogram.

$$\sigma^2_{\varphi(X)} = E\{[\varphi(X) - \mu(X)]^2\} = \int_{-\infty}^{\infty} [\varphi - \mu(X)]^2 \cdot pdf(\varphi) \cdot dx \qquad (A.2)$$

3) Covariance - Second Second-order moment

Covariance is statistics of variance of random variable within two spatial locations.

$$C_\varphi(X_1, X_2) = E\{[\varphi(X_1) - \mu(X_1)][\varphi(X_2) - \mu(X_2)]\} \qquad (A.3)$$

Autocorrelation function ρ is a standardized covariance function, ranged between [-1, 1] as follows (Box 1994):

$$\rho_\varphi(X_1, X_2) = \frac{E\{[\varphi(X_1) - \mu(X_1)][\varphi(X_2) - \mu(X_2)]\}}{\sqrt{E\{[\varphi(X_1) - \mu(X_1)]^2\}E\{[\varphi(X_2) - \mu(X_2)]^2\}}} \qquad (A.4)$$

In equation A.4, we can know autocorrelation is independent of magnitude of data values. $\varphi(X_1)$ is random functions at location X_1.

4) Variogram -Third Second-order moment

The third second-order moment is the structure function or (semi-) variogram. Structure function is a term used in atmospheric turbulence, while (semi-) variogram originates from geo-statistics. Variogram is defined as the variance of the increment of random variable between two spatial locations as follows:

$$D_\varphi(X_1, X_2) = \sigma^2{}_{\Delta\varphi} = 2\Gamma_\varphi(X_1, X_2) = E\{[\Delta\varphi(X_1 - X_2) - \mu(\Delta\varphi)]^2\}$$
$$\Delta\varphi(X_1 - X_2) = [\varphi(X_2) - \mu(X_2)]$$

(A.5)

In equation A.5, D_φ is structure function or variogram and Γ_φ is semi-variogram (Journel and Huijbregts 1978).

A.2 Statistical Stationarity

Statistical stationary is the precondition of spatial analysis, time series analysis and also power spectrum deviation (Huang E. 1998), so Statistical Stationarity is shortly reviewed in this appendix.

Random function is always perceived as the spatial variable, which performs random statistical characteristic in each given spatial point, but behaves with deterministic law among points in certain spatial distribution. Physical variable, Water vapour, the research target in thesis, exactly performs these two characteristics simultaneously, both statistically and deterministically. Based on first and second order moments of random function reviewed above, concepts about stationarity of random function are further shortly reviewed.

Contained in the general set of random functions, terms of nested set of statistically stationary from larger to smaller are as following (Hournel and huijbregts 1978; Chiles and Delfiner 1999):

1) Intrinsic stationary

A random function is intrinsic stationary when (1) the expectation value is constant and exists for every location, as equation 4.6; (2) for all vectors r the increment, $\Delta\varphi(X + r, X) = \varphi(X + r) - \varphi(X)$ has a constant finite variance, as

equation 4.8. Therefore, these functions are also named as random functions with stationary increments.

$$E\{\varphi(X)\} = m, \forall X \qquad (A.6)$$

With equation 4.6, it equals to 4.7 as:

$$E\{\varphi(X+r,X)\} = 0, \forall X \qquad (A.7)$$

$$\begin{aligned} D_\varphi(r) &= \sigma_{\Delta\varphi}^2 \\ &= E\{[\Delta\varphi(X+r,X) - E(\Delta\varphi(X+r,X))]^2\}, \forall X \qquad (A.8) \\ &= E\{[\Delta\varphi(X+r,X)]^2\} \end{aligned}$$

2) Second-order Stationarity

A random function is second-order stationary when first two moments are stationary, i.e. expectation and all second-order moments are stationary.

$$\sigma_{\varphi(X)}^2 = n, \forall X \qquad (A.9)$$

$$C_{\varphi(r)} = E\{\varphi(X+r)\varphi(X)\} - E\{\varphi(X+r)\}E\{\varphi(X)\}, \forall X \qquad (A.10)$$

$$\begin{aligned} D_\varphi(r) &= \sigma_{\Delta\varphi}^2 = 2(\sigma_{\varphi(x)}^2 - \sigma_{\varphi(x+r),\varphi(x)}) \\ &= 2(C_\varphi(0) - C_\varphi(r)), \forall X \end{aligned} \qquad (A.11)$$

In this case, not only hypothesis of intrinsic stationary holds, but also for each pair $[\varphi(X), \varphi(X+r)]$ the covariance is only dependent on the increment vector r. Under second-order stationarity, the covariance and structure function are in fact equivalent (Journel and Huijbregts 1978).

3) Strict Stationarity

A random function is strictly stationary if the probability density function is invariant under translation. Strict stationarity is a severe requirement for random function. Usually the simple term stationarity refers to second-order stationarity.

4) Homogeneity and Isotropy

Besides above three terms of stationarity, homogeneity and are also common terms used for random function. Homogeneity is equivalent term of second-order stationarity in especially 2D and 3D random fields (Balakrishnan 1995). A random field is isotropic if it is not only homogeneous but also with that the covariance

function only depends on the length of increment r and not on its orientation (Chilès and Delfiner 1999; Balakrishnan 1995).

Appendix B Spectrogram, variogram and correlation

1) Power spectrum analysis

The spectrum is the most basic method in signal analysis. Spatially, power spectrum is spectrum of power intensity of signal from spatial domain into frequency domain. Temporally, power spectrum is distribution of power or energy on time or frequency, obtained by Fourier spectral transformation with a limited time window and by successively sliding the window distribution along the time axis.

Two dimensional (2D) Fast Fourier Transformation (FFT) is generally used to estimate the 2D power spectrum of signals. The one dimensional rotationally averaged power spectrums are calculated from 2D power spectrum to degrade the spectra noise. The derivation of power spectrum can help reveal in which spatial scale the signal energy dominates and can be mitigated. It also can be useful for variogram model optimization with experimental variogram.

Atmospheric signal power spectrum can be formulated as the amplitude of fast Fourier transform from unbiased estimation of autocorrelation of ZWD time series itself. If we give that ZWD index ranges from 0 to N-1 (N means ZWD Time Series Number), then:

$$C_{zwd,unbiased}(m) = \begin{cases} \dfrac{1}{N-|m|} \sum_{n=0}^{N-m-1} ZWD_{n+m} \bullet & \eta \geq 0 \\ C_{zwd,unbiased}(-m) & m < 0 \end{cases} \quad m \in [-(N-1), N-1]$$

(B.1a)

$$Pow = Amp(FFT)$$

(B.1b)

In equation B.1, C has length of 2N-1. From equation B.1, the power intensity could be estimated from autocorrelation of ZWD, represented in frequency domain.

2) Structure function analysis

Structure function represents variance between two spatial points, also called spatial (semi-) variogram. It quantitatively describes the correlation of signal

134

separated with a spatial vector. As a typical geo-information analytical approach, the structure function analysis describes the spatial variation or variance of two spatial signal with separated distance. This provides the basis of spatial modeling of water vapour and interpolation of water vapour using spatially spaced known values.

$$\gamma(h) = \frac{1}{2n_C} \sum_{i=1}^{n_C} (z(x_i) - z(x_i + h))^2 \qquad \text{(B.2)}$$

In the equation B.2, $z(x_i)$ is value of random function at spatial vector x_i, n_C is the number of samples in each distance bin. In isotropy case, h is the separated distance of two spatial vectors. In anisotropy case, it stands for the vectorized distance, using symbol $\bar{h}$ instead.

3) Correlation analysis

Correlation describes the similarity of signal with certain spatial or temporal baseline. The correlation could be calculated by the moments, described in detail in appendix. The population correlation coefficient $\rho_{X,Y}$ between two random variables X and Y with expectation μ_X and μ_Y and standard deviations σ_X and σ_Y is defined as following equation:

$$\begin{aligned} \rho_{X,Y} = corr(X,Y) &= \frac{cov(X,Y)}{\sigma_X \sigma_Y} \\ &= \frac{E[(X - \mu_X)(Y - \mu_Y)]}{\sigma_X \sigma_Y} \end{aligned} \qquad \text{(B.3)}$$

In equation B.3, $\rho_{X,Y}$ is standard correlation coefficient, E is the operator of expectation, and cov means covariance.

Publications

1) Book and Book Chapters

F. Chen, H. Lin, **S. Cheng**, "Principle, algorithms and applications of satellite SAR interferometry and its time series analysis", Survey & Mapping Press., (In Chinese, forthcoming).

2) Refereed Journal Papers

S. Cheng, D. Perrisin, H. Lin, F. Chen, Agreement Analysis of atmospheric measurement from GPS and SAR APS, Journal of Atmospheric and Solar-Physics (SCI) (Under review).

S. Cheng, Hui Lin, Liming Jiang, Fulong Chen, Qing Zhao, Radar Interferometry Atmospheric Phase Map Generation from GPS Water Vapor and Validation with Coherent Points in Hong Kong, Remote Sensing, 1, 1-x manuscripts; doi:10.3390/rs10x000x (In revision).

S. Cheng, H. Lin, L. Jiang, F. Chen, Q. Zhao, SAR interferometry atmospheric mitigation from GPS water vapor retrieval in Hong Kong, 2009 Joint Urban Remote Sensing Event, 20-22 May 2009, Shanghai, IEEE published Proceeding (EI), doi:978-1-4244-3461-9/09.

L. Jiang, H. Lin, **S. Cheng**, Monitoring and assessing reclamation settlement in coastal areas with advanced InSAR techniques: Macao city (China) case study, International Remote Sensing (SCI), 2011 (Accepted).

F. Chen, H. Lin, K. Yeung and **S. Cheng**, Detection of Slope Instability in Hong Kong Based on Multi-baseline differential SAR interferometry using ALOS PALSAR data, GIS Science & Remote Sensing (SCI). 2010 (Vol. 47), 02, pp: 208-220 DOI:10.2747/1548-1603.47.2.208.

Q. Zhao, H. Lin, L. Jiang, F. Chen and **S. Cheng**, A Study of Ground Deformation in the Guangzhou Urban Area with Persistent Scatterer Interferometry, Sensors (SCI), 2009, 09, pp:503-518; doi:10.3390/s90100503.

3) Conference Proceedings:

Shilai Cheng, Daniele Perissin, Hui, Lin, Fulong Chen, Agreement analysis of atmospheric delay from GPS and InSAR, 2011 IEEE International Geoscience and Remote Sensing Symposium (IGARSS), 24-19 July, 2011, Vancouver, Canada.

Shilai Cheng, Hui Lin, Longsang Chiu, Fulong Chen, Liming Jiang, Qing Zhao, Validation and Correction of Elevation-dependent Atmospheric Stratification Effect on PALSAR Interferograms using Radiosondes in Hong Kong, 2010 Remote Sensing Symposium across Taiwan Strait, National Central University, Jhong Li, Taiwan, March, 2010 (Digital Conference Proceedings).

Shilai Cheng, Hui Lin, Longsang Chiu, Fulong Chen, Liming Jiang, Qing Zhao, Validation and correction of elevation-correlated atmospheric stratification effect in InSAR ground feature deformation monitoring, in International Workshop on Spatial Information Technologies for Monitoring the Deformation of Large-Scale Man-made Linear Features, Jan. 11-12, 2010, Hong Kong, China, (Digital Conference Proceedings).

4) Paper(s) in preparation

S. Cheng, D. Perissin, H. Lin, F. Chen, "Spatial and Temporal Stochasticity of water vapor components from synchronous MERIS, MM5 and SAR APS", to Journal of Selected Topics in Applied Earth Observations and Remote Sensing (in preparation).

References

Albert, P., Bennartz, R. and Fischer, J. (2001). Remote Sensing of Atmospheric Water Vapor from Backscattered Sunlight in Cloudy Atmospheres. Journal of Atmospheric and Oceanic Technology, 18(6), 865-874.

Avallone, A., Zollo, A., Briole, P., Delacourt, C. and Beauducel, F. (1999). Subsidence of Campi Flegrei (Italy) detected by SAR interferometry. Geophysical Research Letters, 26(15), 2303-2306.

Baby, H.B., Golé, P. and Lavergnat, J. (1988). A model for the tropospheric excess path length of radio waves from surface meteorological measurements. Radio Science, 23(6), 1023-1038, doi:10.1029/RS023i006p01023.

Balakrishnan, A. V. (1995), Introduction to random processes in engineering, John Wiley, New York.

Bennartz, R., and Fischer, J. (2001). Retrieval of column water vapour over land rom backscattered solar radiation using the medium resolution imaging spectrometer. Remote Sensing of Environment, 78,274-283.

Berardino, P., Fornaro, G., Lanari, R and Sansosti, E. (2002). A new algorithm for surface deformation monitoring based on small baseline differential SAR interferograms. IEEE Transactions on Geoscience and Remote Sensing, 40(11), 2375-2383.

Berardino, P., Casu, F., Fornaro, G., Lanari, R., Manunta, M., Manzo, M. and Sansosti, E. (2004). A quantitative analysis of the SBAS algorithm performance. International Geoscience and Remote Sensing Symposium, Anchorage, Alaska, 3321-3324.

Bevis, M., Businger,S., Herring, T.A., Anthes, R.A., Rocken, C. and Ware, R.H. (1992). GPS meteorology: Remote sensing of atmospheric water vapor using the Global Positioning System. Journal of Geophysical Research, 97(D14), 15, 787-15,801.

Bevis, M., Businger,S., Chiswell, S., et al. (1994). GPS meteorology: mapping zenith wet delays onto precipitable water. Journal of Applied Meteorology, 33(3), 379-386.

BobTubbs (1997). Astronomical optical interferometry: A Literature Review (Updated 2000). St. John's College, Cambridge.

Bock, Y., and Williams, S. (1997). Integrated satellite interferometry in Southern California. EOS, 78 (29), 293, 299-300.

Bonforte, A., Ferretti, A., Prati, C., Puglisi, G. and Rocca, F. (2001). Calibration of atmospheric effects on SAR interferograms by GPS and local atmosphere models: first results. Journal of Atmospheric and Solar-Terrestrial Physics, 63(12), 1343-1357.

Box, G. E. P., Jenkins, G. M. and Reinsel, G. C. (1994), Time series analysis: forecasting and control, Prentice-Hall, Englewood Cliffs, 3rd edn.

Bracewell, R.N. (1995). Two-Dimensional Imaging. Prentice Hall, New Jersey, ISBN:013062621X.

Breit, H., Knöpfle, W., Adam, N., Eineder, M., Suchandt, S. and Rabus, B. (2002). SRTM X-SAR DEM of Europe - Results and algorithmic improvements. International Geoscience and Remote Sensing Symposium, Toronto, Canada, 24-28.

Buckley, S.M. (2000). Radar Interferometry Measurement of Land Subsidence. PhD thesis, The University of Texas at Austin, Austin.

Buckley, S.M., Rosen, P.A., Hensley, S. and Tapley, B.D. (2003). Land subsidence in Houston, Texas, measured by radar interferometry and constrained by extensometers. Journal of Geophysical Research, 108 (B11), 2542, doi:10.1029/2002JB001848.

Carnec, C., and Fabriol, H. (1999). Monitoring and modeling land subsidence at the Cerro Prieto geothermal field, Baja California, Mexico, using SAR interferometry. Geophysical Research Letters, 26(9), 1211-1215, doi: 10.1029/ 1999 GL900062.

Cavalié, O., Doin, M.-P., Lasserre, C. and Briole.P. (2007). Ground motion measurement in the Lake Mead area, Nevada, by differential synthetic aperture radar interferometry time series analysis: Probing the lithosphere rheological structure. Journal of Geophysical Research, 112, B03403, doi: 10.1029/2006JB 004344.

Cervelli, P., Murray, M.H., Segall, P., Aoki, Y. and Kato, T. (2001). Estimating source parameters from deformation data, with an application to the March 1997 earthquake swarm of the Izu Peninsula, Japan. Journal of Geophysical Research, 106, 11,217-11,237.

Chaboureau, J.P., Chédin, A. and Scott, N. A. (1998). Remote sensing of the vertical distribution of the atmospheric water vapor from the TOVS observations: method and validation. Journal of Geophysical Research, 103 (D8), 8743-8752.

Cheng, S.L., Lin, H., Jiang, L.M., Chen, F.L. and Zhao, Q.. Radar Interferometry Atmospheric Phase Map Generation from GPS Water Vapor and Validation with Coherent Points in Hong Kong. Remote Sensing, 1, 1-x manuscripts, doi: 10.3390/rs10x000x, under revision.

Chilès, J.-P. and Delfiner, P. (1999), Geostatistics: modeling spatial uncertainty, Wiley Series in Probability and Statistics, John Wiley & Sons, New York.

Colesanti, C., Ferretti, A., Prati, C. and Rocca, F. (2003). Monitoring landslides and tectonic motions with the Permanent Scatterers Technique. Engineering Geology, 68(1-2), 3-14.

Crook, N.A. (1996). Sensitivity of moist convection forced by boundary layer processes to low-level thermodynamic fields. Monthly Weather Review, 124, 1767-1785.

Crosetto, M., Tscherning, C.C., Crippa, B. and Castillo, M. (2002). Subsidence monitoring using SAR interferometry: Reduction of the atmospheric effects using stochastic filtering. Geophysical Research Letters, 29(9), 1312, doi: 10.1029/2001GL013544.

Cumming, I.G., and Wong, F. H. (2005). Digital processing of synthetic aperture radar data: algorithms and implementation. Artech House, Boston, ISBN: 9781580530583.

Delacourt, C., Briole, P. and Achache, J.A. (1998). Tropospheric corrections of SAR interferograms with strong topography application to Etna. Geophysical Research Letters, 25(15), 2849-2852.

Ding, X.L., Li, Z.W., Zhu J.J., Feng, G.C. and Long, J.P. (2008). Atmospheric Effects on InSAR Measurements and Their Mitigations. Sensors, 8, 5426-5448,

doi: 10.3390/s8095426.

Dodson, A., and Baker, H.C. (1998). The accuracy of GPS water vapour estimation. In Proceedings of the ION National Technical Meeting, Navigation 2000, Long Beach, California.

Doin, M.-P., et, al. (2009). Corrections of stratified tropospheric delays in SAR interferometry: validation with global atmospheric model. J. Appl. Geophs., doi: 10.1016/j.jappgeo.2009.03.010.

Dudhia.J, Gill, D., Manning,K., Wang,W., Bruyere,C., Kelly, S. and Lackey,K. (2005). PSU/NCAR Mesoscale Modeling System Tutorial Class Notes and User's Guide: MM5 Modeling System Version 3.7.

Emanuel, K., Raymond, D., Betts, A., et al (1995). Report of the first prospectus development team of the U.S., weather research program to NOAA and the NSF. Bulletin of the American Meteorological Society, 76,1194-1208.

ESA (2006), MERIS Product Handbook. Issue 2.0, 14 Apr. 2006, http://www.envisat.esa.int/handbooks/meris/.

Evans, J.V., Hagfors, T. and Laboratory, L. (1968). Radar Astronomy. McGraw-Hill, New York.

Farr, T.G., and Kobrick, M. (2000). Shuttle Radar Topography Mission produces a wealth of data. EOS Transactions American Geophysical Union, 81,583-585.

Ferretti, A., Prati, C. and Rocca, F. (1999). Multibaseline InSAR DEM reconstruction: The wavelet approach. IEEE Transactions on Geoscience and Remote Sensing, 37 (2), 705-715.

Ferretti, A., Prati, C. and Rocca, F. (2000). Nonlinear subsidence rate estimation using Permanent Scatterers in Differential SAR Interferometry. IEEE Transactions on Geoscience and Remote Sensing, 38 (5),2202-2212.

Ferretti, A., Prati, C. and Rocca, F. (2001). Permanent Scatterers in SAR Interferometry. IEEE Transactions on Geoscience and Remote Sensing, 39 (1),8-20.

Ferretti, A., Novali, F., Passera, E. and Rocca, F. (2005). Statistical analysis of atmospheric components in ERS SAR data. Fringe.

141

Ferretti, A. Passera, E. Novali, F., Prati, C., Rocca, F. (2007), Impact of atmospheric effects on PSInSAR results. Geophysical Research Abstracts, Vol. 9,02288,2007.SRef-ID:1607-7962/gra/EGU2007-A-02288,EuropeanGeosciences Union, 2007.

Fischer, J., and Bennartz, R. (1997). ATBD 2.4 retrieval of total water vapour content from MERIS measurements. Technical Report PO-TN- MEL-GS-0005, ESA.

Gabriel, A.K., Goldstein, R.M. and Zebker, H.A. (1989). Mapping small elevation changes over large areas: Differential Radar Interferometry. Research, 94 (B7),9183-9191.

Gao, B.C., and Kaufman, Y.J. (2003). Water vapor retrievals using Moderate Resolution Imaging Spectro radiometer (MODIS) near-infrared channels. Journal of Geophysical Research, 108 (D13), 4389, doi:10.1029/2002 JD003023.

Ge, L.L, Han S.W. and Rizos C. (2000). The double interpolation and double prediction (DIDP) approach for InSAR and GPS integration. 19th International Society of Photogrammetry & Remote Sensing Congress & Exhibition, Amsterdam, Holland,,205-212.

Ghiglia, .D.C., and Romero, L.A. (1996). Mimimum Lp-norm two dimensional phase unwrapping. Journal of the Optical Society of America A: Optics, Image Science and Vision, 13(10), 1999-2013.

Goldstein, R.M. (1995). Atmospheric limitations of repeat-track radar interferometry. Geophysical Research Letters, 22 (18), 2517-2120.

Graham, L.C. (1974). Synthetic interferometer radar for topographic mapping. Proceedings of the IEEE, 62(6),763-768.

Gray, A.L., and Farris-Manning, P.J. (1993). Repeat-pass interferometry with airborne synthetic aperture radar. IEEE Transactions on Geoscience and Remote Sensing, 31,180-191.

Grell, G.A., Dudhia,J. and Stauffer, D. R. (1994). A description of the fifth-generation Penn State/NCAR mesoscale model (MM5). NCAR Technical Note, NCAR/TN-398+STR, 117 pp.

Hanssen, R.F. (1998). Atmospheric heterogeneities in ERS tandem SAR interferometry, 136 pp. Delft University Press, Delft, the Netherlands.

Hanssen R., Lehner, S. and Weinreich, I., (1998). Atmospheric heterogeneities from - ERS tandem SAR interferometry and sea surface images. In CEOS SAR Workshop, ESTEC, Noordwijk, The Netherlands, 3-6 February 1998, pages 33-39.

Hanssen, R.F., et al (1999). High-Resolution Water Vapor Mapping from Interferometric Radar Measurements. Science, 283(5406), 1295-1297,DOI: 10.1126/science.283.5406.1297.

Hanssen, R.F. (2001). Radar interferometry: Data Interpretation and Error Analysis, xviii, 308 pp. Kluwer Academic, Dordrecht, Boston,ISBN-10: 0792369459.

Hanssen, R., Moisseev, D., and Businger,S. (2003). Resolving the acquisition ambiguity for atmospheric monitoring in multipass radar interferometry. In International Geoscience and Remote Sensing Symposium, Toulouse, France, 21–25 July 2003, pages cdrom, 4 pages.

Henderson, F.M., and Lewis, A.J (1998). Principles & Applications of Imaging Radar,Manual of Remote Sensing. John Wiley & Sons, New York, 3rd edition.

Herring, T.A., King, R.W and McKlusky, S.C. (2006). GAMIT Reference Manual: GPS Analysis at MIT, Version 10.3. . Massachusetts Institute of Technology, Cambridge.

Hilley, G.E., Burgmann, R., Ferretti, A., Novali, F. and Rocca, F. (2004). Dynamics of slow-moving landslides from Permanent Scatterer analysis. Science, 304(5679), 1952-1955.

Hooper, A.J. (2006). Persistent Scatterer Radar Interferometry for Crustal Deformation Studies and Modeling of Volcanic Deformation. PhD thesis, Stanford University, Standford.

Huang, E. et al. (1998). The empirical mode decomposition and the Hilbert spectrum for nonlinear and non-stationary time series analysis. Proc. R. Soc. Lond. A, 454, 903–995.

Jónsson, S., Adam, N. and Björnsson.H. (1998). Effects of subglacial geothermal

activity observed by satellite radar interferometry. Geophysical Research Letters, 25(7), 1059-1062.

Journel, A. G. and Huijbregts, C. J. (1978), Mining Geostatistics, Academic Press, London.

JPL (2004). Shuttle Radar Topography Mission - the mission to map the on line. http://www2.jpl.nasa.gov/srtm/.

Kalnay, E. (2003). Atmospheric Modelling, Data Assimilation and Predictability. Cambridge University Press, ISBN-10: 0521796296.

Kistler, R., et al. (1999), The NCEP/NCAR 50-year reanalysis, Bull. Am. Meteorol. Soc., 82, 247– 268.

Knospe, S.H.G. and Jónsson, S., (2010). Covariance Estimation for dInSAR Surface Deformation Measurements in the Presence of Anisotropic Atmospheric Noise, IEEE TRANSACTIONS ON GEOSCIENCE AND REMOTE SENSING, VOL. 48, NO. 4.

Kovaly, J.J. (1976). Synthetic Aperture Radar. Artech House, Dedham, Mass, ISBN: 0890060568.

Kramer, H.J. (1994). Observation of the Earth and Its Environment: Survey of Missions and Sensors. Springer-Verlag, Berlin, ISBN 3540578587.

Lanari, R., Mora, O. and Manunta, M. (2004). A small-baseline approach for investigating deformations on full-resolution differential SAR interferograms. IEEE Transactions on Geoscience and Remote Sensing, 42(7), 1377-1386.

Li, Z.H., et al (2003). Validation of MERIS Near IR water vapour retrievals using MWR and GPS measurements. in MERIS user workshop, ESA ESRIN,Frascati,Italy,10-13.

Li, Z.H. (2004). Production of 1KM Water Vapor using MODIS. ION 2004.

Li, Z.H. (2005). Correction of Atmospheric Water Vapour Effects on Repeat-Pass SAR Interferometry Using GPS, MODIS and MERIS Data. PhD thesis, University of College London, U.K..

Li, Z.H, Muller, J.-P., Cross, P. and Fielding, E.J. (2005). Interferometric synthetic

aperture radar (InSAR) atmospheric correction: GPS, Moderate Resolution Imaging Spectro-radiometer (MODIS), and InSAR integration. Journal of Geophysical Research, 110, B03410, doi: 10.1029/2004JB003446.

Li, Z.H, Muller, J.-P., Cross, P., Albert, P., Fischer, J. and Bennartz, R. (2006). Assessment of the potential of MERIS near-infrared water vapour products to correct ASAR interferometric measurements. International Journal of Remote Sensing, 27(2), 349-365, ISSN 0143-1161.

Li, Z.H, Fielding, E.J.Cross, P. and Muller, J.-P. (2006). Interferometric synthetic aperture radar atmospheric correction: GPS topography-dependent turbulence model. Journal of Geophysical Research, 111, B02404, doi:10.1029/2005JB003711.

Li, Z.H, Fielding, E.J., Cross, P. and Preusker, R. (2009). Advanced InSAR atmospheric correction: MERIS/MODIS combination and stacked water vapour models. International Journal of Remote Sensing, 30(13), 3343-3363.

Li, Z.W. (2004). Modeling Atmospheric effects on Repeat-pass InSAR Measurements. PhD thesis, The Hong Kong Polytechnic University, Hong Kong.

Li, Z.W., Ding, X.L. and Liu, G.X. (2004). Modeling atmospheric effects on InSAR with meteorological and continuous GPS observations: algorithms and some test results. Journal of Atmospheric and Solar-Terrestrial Physics, 66,907–917.

Li, Z.W., Ding, X.L., Huang, C and Zheng, D.W.(2006). Modeling of atmospheric effects on InSAR measurements by incorporating terrain elevation information. Journal of Atmospheric and Solar-Terrestrial Physics, 68(11), 1189-1194.

Li, Z.W., Ding, X. L., Huang, C., et al (2007). Atmospheric effects on repeat-pass InSAR measurements over Shanghai region. Journal of Atmospheric and Solar-Terrestrial Physics, 69(12), 1344-1356.

Mason, N., Hughes, P., McMullan,P., Reynolds, R., Simmonds, L. and Twidell, J. (2001). Introduction to environmental physics: planet earth, life and climate. Tylor&Francis, London.

Massonnet, D., Rossi, M., Carmona, C. , Adragna, F. , Peltzer, G. , Feigi, K.

and Rabaute, T. (1993). The displacement field of the Landers earthquake mapped by radar interferometry. Nature, 364,138-142, doi:10.1038/364138a0.

Massonnet, D., Feigl, K., Rossi, M. and Adragna, F. (1994). Radar interferometric mapping of deformation in the year after the Landers earthquake. Nature, 369,227-230, doi:10.1038/369227a0.

Massonnet, D., Briole, P. and Arnaud, A. (1995). Deflation of Mount Etna monitored by spaceborne radar interferometry. Nature, 375,567-570.

Massonnet, D., and Feigl, K.L. (1998). Radar interferometry and its application to changes in the Earth's surface. REVIEWS OF GEOPHYSICS, 36(4), 441-500,doi:10.1029/97RG03139.

Mobasheri, M.R., Purbagher Kordi S.M., Farajzadeh, M. and Sadeghi Naeini, A. (2008). Improvement of Remote Sensing Techniques in TPW Assessment Using Radiosonde Data. Journal of Applied Sciences, 8(3), 480-488.

Mockler, S.B., Water vapor in the climate system (Special Report, December 1995) (1995). (Available online at: http://www.agu.org/sci_soc/mockler.html). American Geophysical Union, Jekyll Island, Georgia.

Mohr, J.J, Reeh, N. and Madsen, S.N. (1998). Three-dimensional glacial flow and surface elevation measured with radar interferometry. Nature, 391, 273-276, doi:10.1038/34635.

Mora, O., Mallorqui, J.J. and Broquetas, A. (2003). Linear and nonlinear terrain deformation maps from a reduced set of interferometric SAR images. IEEE Transactions on Geoscience and Remote Sensing, 41(10), 2243-2253.

Niell, A.E. (1996). Global mapping functions for the atmosphere delay at radio wavelengths. Journal of Geophysical Research, 101(B2), 3227-3246.

Odijk, D., Fast precise GPS positioning in the presence of ionospheric delays (2002). PhD thesis. Delft University of Technology, Delft, 96-102.

Onn, F (2006). Modeling water vapor using GPS with application to mitigating InSAR atmospheric distortions. PhD thesis, Stanford University, Stanford .

Perissin, D., Ferretti, A., Piantanida, R., et al (2007). Repeat-pass SAR interferometry with partially coherent targets. Proceedings of Fringe 2007,

26-30, Frascati (Italy).

Perissin, D., Pichelli, E., Ferretti, R., Rocca, F. and Pierdicca, N. (2009). The MM5 Numerical Model to correct PSInSAR Atmospheric Phase Screen. Proceedings of FRINGE 2009, Frascati (Italy).

Perissin D., Pichelli, E., Ferretti, R., Rocca, F., and Pierdicca, N., (2010). Mitigation of Atmospheric Water-vapour Effects on Spaceborne Interferometric SAR Imaging through the MM5 Numerical Model, PIERS Proceedings, Xi'an, China, March 22-26.

Perissin, D. (2010). Report of METAWAVE project, July.

Pierdicca, N., Rocca, F., et al (2009). Atmospheric water-vapour effects on spaceborne interferometric SAR imaging: Data synergy and comparison with ground-based measurements and meteorological model simulations at urban scale. In Proc. EuCAP, Berlin, Germany, Mar. 23–27, pp. 3443–3447.

Pichelli, E. Ferretti, R. Cimini, D. Perissin, D., Montopoli1, M., Marzano1, F. S. and Pierdicca, N. (2010). Water vapour distribution at urban scale using high-resolution numerical weather model and spaceborne SAR interferometric data, Nat. Hazards Earth Syst. Sci., 10, 121–132.

Pritchard, M.E., and Simons, M. (2002). A satellite geodetic survey of large-scale deformation of volcanic centers in the central Andes. Nature, 418,167-171, doi:10.1038/nature00872.

Rabus, B., Eineder, M., Roth, A. and Bamler, R. (2003). The shuttle radar topography mission - a new class of digital elevation models acquired by spaceborne radar. ISPRS Journal of Photogrammetry and Remote Sensing, 57 (4),241-262.

Rao, K.S., and Phalke, S.M. (2001). Analysis of dem derived from SRTM for the assessment of geo-coding and height accuracy. International Geoscience and Remote Sensing Symposium, Sydney, Australia, pages cdrom, 4 pages.

Refice, A., Belmonte, A, Bovenga, F. and Pasquariello, G. (2011), On the Use of Anisotropic Covariance Models in Estimating Atmospheric DInSAR Contributions, IEEE GEOSCIENCE AND REMOTE SENSING LETTERS, VOL. 8, NO. 2.

Rigo, A., and Massonet, D. (1999). Investigating the 1996 Pyrenean earthquake (France) with SAR Interferograms heavily distorted by atmosphere. Geophysical Research Letters, 26 (21),3217-3220.

Rind, D., Chiou, E.-W., Chu, W, et al (1991). Positive water vapour feedback in climate models confirmed by satellite data. Nature, 349,500-503, doi:10.1038/349500a0.

Rogers, A.E.E., and Ingalls, R.P. (1969). Venus - mapping the surface reflectivity by radar interferometry. Science, 165,797-799.

Rosen, P.A., Hensley, S., Zebker, H.A. and Webb, F.H. (1996). Surface deformation and coherence measurements of Kilauea volcano, Hawaii, from SIR-C radar interferometry. Journal of Geophysical Research, 101 (E10), 23, 109-23,125, doi:10.1029/96JE01459.

Rubin, A.M. (1992). Dike-induced faulting and graben subsidence in the volcanic rift zones. Journal of Geophysical Research, 97, 1839-1858.

Saastamoinen, J. (1972). Atmospheric correction for the troposphere and stratosphere in radio ranging of satellites, in The Use of Artificial Satellites for Geodesy, . Geophysical Monograph, Ser.15 (S.W. Henriksen et al.,eds.),AGU, Washington, D.C.,247-251.

Sandwell, D.T., and Price, E.J. (1998). Phase gradient approach to stacking interferograms. Journal of Geophysical Research, 103(B12), 30183-30204, doi:10.1029/1998JB900008.

Schaer, S., Mapping and Predicting the Earth's Ionosphere Using the Global Positioning System (1999). PhD thesis. University of Berne, Berne, Switzerland.

Smith, M.J., Goodchild, M.F. and Longley, P.A. (2009). Geospatial Analysis: A Comprehensive Guide to Principles, Techniques and Software Tools. Leicester: Matador, ISBN: 9781848761575.

Song, K.,Wu, J., Li, L. Wang Z., Lu D., Du, J. Zhang, B. (2010). MODIS- Derived Atmospheric Water Vapor (AWV) Content and Its Correlation to Land Use and Land Cover in Northeast China, Remote Sensing and Modeling of Ecosystems for Sustainability, Proc. of SPIE Vol. 7809, 78090L, doi:

Song, S., (2006), Sensing Three Dimensional Water Vapor Structure with Ground-based GPS Network and the Application in Meteorology. PhD Thesis, Shanghai Astronomical Observatory, CAS, China (In Chinese).

Tatarski, V.I. (1961), Wave Propagation in a Turbulent Medium. New York: McGraw-Hill.

Thompson, P.D. (1961). Numerical Weather Analysis and Prediction. New York, The Macmillan Company.

Tomiyasu, K. (1978). Tutorial Review of Synthetic-Aperture Radar (SAR) with Applications to Imaging of the Ocean Surface. Proceedings of the IEEE, 66 (5), 563-583.

Twine, T.E., Kucharik, C.J., Foley,J.A., (2004). Effects of Land Cover Change on the Energy and Water Balance of the Mississippi River Basin, Journal of Hydrometeorology, Vol., 5, pp: 640-655.

Vcka, J.K. (2006). Radar Interferometry used for detection of landslides and subsidences in the Northern Bohemia Brown Coal Basin. PhD thesis, Czech Technical University, Prague, Czech Republic.

Wackernagel, H. (1998). Multivariate Geostatistics, 2nd Edition. Springer Verlag, Berlin, ISBN 3-540-64721-X.

Wadge, G., Webley, P.W., James, I.N., et al (2002). Atmospheric models, GPS and InSAR measurements of the tropospheric water vapour field over Mount Etna. Geophysical Research Letters, 29 (19), 1905, doi: 10.1029/ 2002 GL015159.

Williams, S., Bock, Y. and Fang, P. (1998). Integrated satellite interferometry: Troposphere noise, GPS estimates, and implications for synthetic aperture radar products. Journal of Geophysical Research, 103 (B11), 27051-27067, doi:10.1029/98JB02794.

Xu, C.J, Wang, H, Ge, L.L, et al (2006). InSAR tropospheric delay mitigation by GPS observations: A case study in Tokyo area. Journal of Atmospheric and Solar-Terrestrial Physics, 68(6), 629-638.

Zebker, H.A., and Goldstein, R.M. (1986). Topographic mapping from

interferometric synthetic aperture radar observations. Journal of Geophysical Research, 91(B5), 4993-4999.

Zebker, H.A., and Villasenor, J. (1992). Decorrelation in interferometric radar echoes. IEEE Transactions on Geoscience and Remote Sensing, 30 (5), 950-959.

Zebker, H.A., Rosen, P., Goldstein, R., Gabriel, A. and Werner, C. (1994). On the derivation of co-seismic displacement fields using differential radar interferometry: the Landers earthquake. Journal of Geophysical Research, 99 (B10), 19, 617-634.

Zebker, H.A., Rosen, P.A. and Hensley, S. (1997). Atmospheric effects in interferometric synthetic aperture radar surface deformation and topographic maps. Journal of Geophysical Research, 102(B4), 7547-7563.

Zisk, S.H. (1972). A new Earth-based radar technique for the measurement of lunar topography. Moon, 4,296-300.